TESTING GENERAL RELATIVITY AND PROBING NUCLEAR PHYSICS IN THE ERA OF GRAVITATIONAL WAVES

A Dissertation
Presented to
The Academic Faculty

By

Sudarshan Ghonge

In Partial Fulfillment
of the Requirements for the Degree
Doctor of Philosophy in the
School of Physics
Center for Relativistic Astrophysics

Georgia Institute of Technology

December 2021

TESTING GENERAL RELATIVITY AND PROBING NUCLEAR PHYSICS IN THE ERA OF GRAVITATIONAL WAVES

Thesis committee:

Prof. Laura Cadonati
Center for Relativistic Astrophysics, School of Physics
Georgia Institute of Technology

Prof. John Wise
Center for Relativistic Astrophysics, School of Physics
Georgia Institute of Technology

Prof. Deirdre Shoemaker
Center for Gravitational Physics , Department of Physics
The University of Texas at Austin

Prof. Ümit Çatalyürek
School of Computational Science and Engineering
Georgia Institute of Technology

Prof. Ignacio J. Taboada
Center for Relativistic Astrophysics, School of Physics
Georgia Institute of Technology

Date approved: December 10, 2021

ACKNOWLEDGMENTS

This thesis would not have been possible without the advisor, Laura Cadonati. I'd like to thank her for giving me the opportunity to work in this amazing world of LIGO, and for all the intellectual scientific growth I was able to achieve under her advisement. She has been very patient, and accommodating while working with me, and has let me steer my Ph.D. in the direction I wanted while being a stabilizing force. I'm immensely grateful to her for her unwavering support during the past five years, and especially during the last final two years of my Ph.D. amidst a global pandemic.

I'd like to also thank James Clark who got me started on my first LIGO project at Georgia Tech and later introduced me to the BayesWave working group. I have had several interesting discussions with him about science, research, computing, development, bicycles, and beer. I owe my soon-to-start career in scientific software development to him.

I am also immensely thankful to Deirdre Shoemaker and Pablo Laguna because of whom I was able to do projects that involved both numerical relativity and observational gravitational wave astronomy. As heads of the center of relativistic astrophysics, and the school of physics respectively, and as the two of the three faculty advisors of the Georgia Tech LIGO group, they have been a constant source of support and advice.

I'd like to express my sincere gratitude to Katerina Chatziiaonnou for encouraging me to join production-level analyses in LIGO, guiding me through the various analysis and review processes, including me on her some of her own projects, and finally co-authoring and being the main driving force in my first leading author paper. There is a great deal I learned from her.

My thesis crucially relies on the BayesWave algorithm developed by Neil Cornish and Tyson Littenberg whom I'd like to thank. I'd also like to thank the entire BayesWave working group including Neil Cornish, Tyson Littenberg, James Clark, Katerina Chatziioannou, Meg Millhouse, Sophie Hourihane, and Bence Becsy. This has been an amazing journey

and I could not have asked for a better group to work with. I will cherish the biweekly BayesWave meetings which were a place of cutting-edge scientific discourse, whilst maintaining a friendly and comfortable environment that allowed thoughts to flow. Decisions on critical technical design aspects of my projects were possible due to the discussions that have happened here.

During the 5 years of my Ph.D., I have been part of three gravitational transient catalogs published by LIGO and Virgo. Alongside the analysis, I had the opportunity to make amazing pieces of artwork with Karan Jani which showcase the detections. I'm also very thankful to him for all the discussions about long-term scientific ideas, science communication, and education.

I'm extremely grateful to the amazing set of junior colleagues whom I have had the privilege of mentoring: Peter Lott, Megan Arogeti, Joshua Brandt, Jack Sullivan, Nadia Qutob, and Jessica Eskew. It has been an amazing experience to supervise their projects, and more importantly to learn from them. I'd especially like to thank them for taking charge and leading the residuals, reconstructions, and glitch cleaning projects, and thus allowing me time to write my thesis.

I'd like to thank Jack Sullivan for the amazing web development work for the igwn-wave-compare project. Thanks also to Joshua Brandt for quickly picking up batch deployment of a large number of glitch-cleaning jobs, and for the useful figures that I used in my thesis. My special thanks to Sophie Hourihane for discussions about the BayesWave models, useful plotting scripts, and helpful python development work needed to diagnose the various BayesWave glitch-cleaning jobs.

I'm also thankful to all my colleagues in the LIGO and Virgo Collaborations especially Maximilliano Isi, Anuradha Gupta, Christopher Berry, Will Farr, Carl-Johan Haster, Robert Cotesta, Sebastian Khan, Nathan K. Johnson-McDaniel, Parameswaran Ajith, Archisman Ghosh, Sukanta Bose, Nairwita Mazumder, Richard Udall, Edoardo Milotti, Claudia Lazarro, Sergey Klimenko, Jacob Lange, Patricia Schmidt, Aaron Zimmerman, Charlie Hoy, John

Veitch, Jonah Kanner, Gaby Gonzalez, Daniel Williams, Tom Dent, Gayathri V, Derek Davis, Jess McIver, Andrew Lundgren, Brian O'Reilly, Josh Smith, TJ Massinger, Sidd Soni, Alex Urban, Paul Easter, Paul Lasky, Zoheyr Doctor, Frank Ohme, Abhirup Ghosh, Chun-Fung Wong, Aaron Buikema, Peter Dupej, and Anirban Ain.

I was introduced to the physics of gravitational waves by my undergraduate advisor at BITS Pilani Hyderabad, Rahul Nigam, whom I'd like to thank for bringing me up to speed on General Relativity and pushing me towards a career in research. I'd also like to thank Swarnali Bandhopadhyay, who was the instructor for the computational physics course which made me realize I wanted to pursue a career in computational physics research.

My time in LIGO started in July 2015 - a month before the first gravitational wave detection and it is not coming to an end with 90 detections. It has been an incredibly rewarding journey. I'd like to express my heartfelt gratitude to Parameswaran Ajith for taking me on as a thesis student at ICTS, Bangalore in 2015, and to my senior colleagues in LIGO-India including Bala Iyer, Sukanta Bose, Archisman Ghosh, Chandra Kant Mishra, Sumit Kumar, and Nathan Johnson-McDaniel.

My time as a grad student at Georgia Tech was enriched by my partner Bahnisikha Dutta, and my friends in the Asha Atlanta and the School of Physics including Bhavesh Khamesra, Deborah Ferguson, Shashank Markande, Hemaa Selvakumar, Omid Khosravani, Prasoon Suchandra, Anish Mukherjee, Gareeyasee Saha, Shashidhar Ravishankar, Dhwanil Shukla, Adwait Mane, Shruti Lall, Jyoti Narayana, Derek Hart, Elizabeth Grace, and Pranav Dave.

I'd like to also express my thanks to my friends from my undergraduate life some of whom moved to the United States with me similar dreams of graduate studies including Ajinkya Gavane, Aniket Garg, Swetha Anandhan, Dipna Venkatachalam, and Ruchika Verma.

Finally, I would not have been here without the unconditional support from my amazing family from the very beginning.

This research was made possible due to support from the NSF grants PHY 1806580 and PHY 1809572. Computational resources and tools were provided by LIGO Labs supported by NSF PHY-0757058, PHY-0823459, and by the open science grid supported by the NSF award 1148698

TABLE OF CONTENTS

Acknowledgments iii

List of Tables xi

List of Figures xii

Summary xvi

Chapter 1: Introduction 1

Chapter 2: Gravitational Waves 4

2.1 General Relativity and Einstein field equations 5

2.2 Gravitational Waves: effect and measurement 8

2.3 Gravitational Waves: astrophysics 19

2.4 Compact Binary Coalescences (CBC) 21

2.5 GW astronomy: state of the art 22

Chapter 3: Decrypting the GW signal: inference from data to source 27

3.1 Bayesian inference of source properties 28

3.2 Signal processing methods 29

3.3 Sampling multi-dimensional parameter space 30

3.4 Waveform models 32

3.4.1 GR-based models . . . 32
3.4.2 Burst waveform models . . . 36
3.4.3 Spherical harmonics and unmodeled deviations . . . 37
3.5 GW Searches . . . 38
3.5.1 GR-based searches . . . 38
3.5.2 Burst searches . . . 39
3.6 Offline parameter estimation . . . 39
3.7 `BayesWave` . . . 40
3.8 `BayesWave` use cases . . . 46
3.9 Commonly used data products . . . 48

Chapter 4: Waveform Reconstructions and Consistency Tests . . . 53

4.1 Waveform families . . . 53
4.2 Quantifying agreement between waveforms (overlap) . . . 56
4.3 Variation of the overlap with SNR and M_T . . . 57
4.4 Application to GWTC-1 detections . . . 59
4.5 Application to GWTC-$\{1,2,3\}$ detections . . . 65
4.6 Detecting deviations in templates . . . 66
4.7 The hunt for higher order modes . . . 69
4.7.1 GW170729 . . . 69
4.7.2 GW190412 . . . 71
4.8 Inferring the BBH remnant spin from model-independent reconstructions . 72
4.9 Conclusions . . . 75

Chapter 5: Empirically testing for deviations in General Relativity 77

5.1 Types of tests 77

5.2 The Gaussian nature of detector noise 79

5.3 Details of the residual generation method 81

5.4 Analysis with `BayesWave` 82

5.5 Application to non-GR phenomenological waveforms 85

5.6 Conclusions 89

Chapter 6: Improving detector data quality 90

6.1 Glitches and their causes 90

6.2 GW170817 92

6.3 BBH systems in GWTC-{1,2,3} 94

6.4 Glitch classes 94

6.5 The `Signal+Glitch` model 97

6.6 Improvements to the `Signal+Glitch` model 99

6.6.1 Q priors 100

6.6.2 Dimensionality priors 100

6.6.3 Window priors 100

6.7 Results of the deglitching process 101

6.7.1 Blips 101

6.7.2 Scattering 103

6.7.3 Tomte 106

6.7.4 Mountain glitches 109

6.8 Conclusions 110

Chapter 7: Searching for post-merger GW signals from BNS coalescences 111

7.1 S190425z 113

7.2 Characterizing post-merger detection performance of `BayesWave` and `Bilby` 114

7.3 Stacking Observations 117

7.3.1 Stacking evidences 117

7.3.2 Stacking time-frequency tiles 118

7.4 Conclusions 120

Chapter 8: Conclusions and Outlook 123

Appendices 127

Chapter A: Code infrastructure for doing reconstruction comparisons and residuals analysis 128

A.1 Initial (manual) deployment of workflows 128

A.2 Details of residual storage 132

A.3 Setting up the `BayesWave` time-frequency volume 132

A.4 Selection of background times 133

Chapter B: Simulated Observations of non-GR waveforms 135

References 137

LIST OF TABLES

4.1 Approximants used in GW inference analysis 55

4.2 p-values of GWTC-1 events from the signal consistency test 63

4.3 p-values of GWTC-$\{1,2,3\}$ from the signal consitency test 66

4.4 SNRs and overlaps for `BayesWave` and `LALInference` with GT NR waveform `GT0745` with $M_T = 60M_\odot$ and mass ratio, $q = 6$. 68

4.5 Overlaps between `BayesWave`reconstruction templates for GW170729 . . 71

5.1 p-values of GWTC-1,2,3 events from the residuals analysis. 84

5.2 Modified GR waveform parameters 86

LIST OF FIGURES

2.1 Laser interferometer detection principle 10

2.2 Network of first and second-generation GW detectors across the globe. . . . 11

2.3 Noise sources in Advanced LIGO 13

2.4 Sensitivity of LIGO and other detectors 14

2.5 Einstein Telescope sensitivity 15

2.6 Einstein Telescope, Cosmic Explorer schematic cartoon 16

2.7 Cosmic Explorer sensitivity 17

2.8 LISA cartoon 18

2.9 Sensitivity and source spectra plots 19

2.10 GW150914 phases 23

2.11 Time-frequency heap map of GW150914 data 24

2.12 Post-merger scenarios 25

3.1 Model waveforms overlayed against detector data 28

3.2 Cartoon illustration of nested sampling 31

3.3 Regions of applicability of various GR-modeling methods. 33

3.4 Effect of select parameters on the gravitational waveform 34

3.5 GW150914 mass probability posteriors 41

3.6 Example BayesWave wavelet and chirplet time domain plots. 43

3.7 BayesWave Wavelet and chirplet spectrograms 43

3.8 The BayesLine model 45

3.9 The PSD of GW200129 49

3.10 Whitened waveform of GW200129. 50

3.11 Spectrogram of GW200129 51

3.12 Corner plot of the BayesWave signal wavelets for GW200129 52

4.1 LALInference and BayesWave comparisons with GW150914 53

4.2 Misoverlap as a function of SNR and M_T 59

4.3 Comparison of onsource and offsource overlap 61

4.4 P-values of GWTC-1 events using waveform reconstruction comparisons . 62

4.5 Comparison of overlaps of BayesWave with injected and recovered LALInference waveforms 64

4.6 P-values of GWTC-1 events computed against offsource SNR using injection waveform 65

4.7 P-values of all GWTC-$\{$1,2,3$\}$ events 65

4.8 LALInference and BayesWave comparisons in the presence of higher-order modes 68

4.9 Waveform comparisons for GW170729 70

4.10 Waveform comparisons for GW190412 72

4.11 Relationship between ω, $\dot{\omega}$, $\mathcal{M}$ and a_f 74

4.12 Histogram of the recovered spin from BayesWave 75

5.1 Residual calculation time-frequency plot for GW200129 80

5.2 Residual calculation time-domain plot for GW200129 82

5.3 P-values computing using residuals analysis for GWTC-{1,2,3} events . . . 85

5.4 Waveform reconstructions and residuals time-domain plots for non-GR waveforms 87

6.1 Time-frequency map of GW170817 with glitch-cleaning procedure 93

6.2 Spectrogram of a non-spinning BBH GW signal near a Blip glitch 95

6.3 Time-frequency heat maps of various glitch classes 96

6.4 `BayesWave` time-domain reconstruction of GW150914-like signal injected near a Blip glitch 98

6.5 `BayesWave` time-domain reconstruction of GW150914-like signal injected near a Blip glitch, unsuccessful 99

6.6 Time-frequency heat map depicting glitch cleaning for the Blip glitch . . . 102

6.7 `Bilby` PE corner plot for the Blip glitch case 103

6.8 `BayesWave` time-domain reconstruction of GW150914-like signal injected near a Scattering glitch 104

6.9 Time-frequency heat map depicting glitch cleaning for the Scattering glitch 105

6.10 `Bilby` PE corner plot for the Scattering glitch case 106

6.11 `BayesWave` time-domain reconstruction of GW150914-like signal injected near a Tomte glitch 107

6.12 Time-frequency heat map depicting glitch cleaning for the Tomte glitch . . 108

6.13 `Bilby` PE corner plot for the Tomte glitch case 109

6.14 `BayesWave` time-domain reconstruction of GW150914-like signal injected near a Mountain glitch 110

7.1 Post-merger BNS spectra along with detector sensitivity curves 112

7.2 GW190425 post-merger upper limits 115

7.3 Comparison of Bilby and BayesWave f_{peak} posteriors v/s SNR for BNS post-merger signals 116

7.4 `BayesWave` analysis frequency-domain plots of post-merger BNS 120

7.5 Stacking time-frequency tiles of post-merger non-detections 121

A.1 Workflow of `igwn-wave-compare` 130

A.2 Screenshot of of `iwc` webpage 131

B.1 GW170608-like non-GR waveforms 135

B.2 GW150914-like non-GR waveforms 136

SUMMARY

The LIGO and Virgo detectors have detected 90 gravitational wave events so far. The gravitational waves have come from pairs of black holes or neutron stars. The astrophysical interpretation of these events was made possible by sophisticated modeling of both source and detector noise. In this thesis, I develop and apply model-independent methods to check for biases due to un-modeled astrophysical or terrestrial effects and to search for signals from the remnant of binary neutron star coalescences. The methods use a sine-Gaussian wavelet basis set to reconstruct the gravitational waveform which is sensitive to a wide range of waveform morphologies and enables us to increase detection confidence and improve data quality. I report the results of applying these methods to the first three observing runs of LIGO and Virgo. I also characterize these methods using various simulation studies.

CHAPTER 1
INTRODUCTION

Gravitational Waves are a prediction of General Relativity, the theory of gravity introduced by Albert Einstein in 1916 [1, 2]. Nearly 100 years later, on September 14, 2015, the Laser Interferometer Gravitational-wave Observatories (LIGO) in Hanford, WA, and Livingston, LA observed for the first time ever [3], Gravitational waves (GWs) originating from the merger of a pair of black holes nearly a billion light-years away [4]. The event, named GW150914, followed an effort spanning three decades of instrumentation, data analysis, and theoretical modeling to increase the sensitivity and reliability of the detectors [5].

Since then, LIGO, and Virgo [6], its sister project in Italy, have detected a total of 90 gravitational wave events from pairs of compact objects - black holes and neutron stars [7, 8, 9]. The properties of their sources are inferred by comparing the detector data to the waveforms predicted by Genereal Relativity (GR) [10]. However, since GR is a highly non-linear theory, it is important to investigate these detections for biases due to potential poorly modeled astrophysical effects, or due to transient noise in the detectors [11]. In this thesis, I focus on model-independent data-analysis techniques to characterize these biases and improve the detection confidence.

Additionally, due to the added complexity of matter fields in neutron star systems, physical models for post-merger GW emissions from binary neutron star (BNS) coalescences are either incomplete or prohibitively expensive to use in data analysis; studies agree that these emissions are short-lived bursts with a characteristic frequency [12, 13, 14]. I also discuss methods to reconstruct these bursts using model-independent methods.

Pairs of coalescing black holes or neutron stars are referred to as Compact Binary Coalesces (CBC). In this thesis, I will restrict my focus to stellar-mass CBCs. Additional sources predicted by GR are core-collapse supernovae (CCSN) [15] which emit short-lived

(O(< 1 second)) GWs, rotating asymmetric neutron stars (NSs) [16] which emit continuous (O(years)) GWs, and early universe black hole binaries which emit stochastic (O(billions of years)) GWs [17]. Although the methods I describe in this work are primarily applicable to CBCs, they can be extended to these other sources as well.

The dynamics of the CBCs are given by GR. When two stellar-mass objects orbit each other, they lose energy and momentum as gravitational radiation and their orbits shrink until they merge [18]. In the last few orbits, they become detectable by LIGO and Virgo. The radiated GWs are rich in information about the dynamical evolution. GR is a highly non-linear theory and requires sophisticated analytical [19, 20, 21, 22, 23, 24, 25, 26, 27, 28, 29, 30, 31, 32, 33] and numerical [34, 35, 36, 37, 38, 39] tools and frameworks . Although GWs validate GR, the source inference may be biased due to potential gaps in our models due to analytical conventions or numerical errors. Stellar-mass CBCs, particularly binary black holes (BBHs), emit short-lived (O(few seconds long)) GW *bursts* [4]. Model-independent methods which use discrete or continuous wavelet transforms are most sensitive to these GW bursts [40, 41, 42].

I discuss methods and results of model-independent analyses applied to real and simulated gravitational-wave observations. `BayesWave` [42] is an algorithm that uses minimal assumptions about the underlying gravitational wave morphology to reconstruct the true signal waveform. I employ `BayesWave` to do consistency tests of signal reconstructions [43] given by templated analyses and to do tests of GR [44]. `BayesWave` is also able to characterize stationary and transient instrument noise and separate it from astrophysical signals [45]. I describe methods to exploit this functionality to improve the detector data quality. I also discuss techniques to detect and characterize the post-merger signals from binary neutron star coalescences [46, 47]. Finally, I discuss future prospects of improving the detectability of more complicated systems using model-independent analyses.

The thesis is structured as follows. In chapter 2 I discuss the theoretical background of GWs, interferometric detectors, and the astrophysical inferences we can draw from GW de-

tections. In chapter 3 I introduce methods and techniques that are commonly used in LIGO and Virgo data analysis, including a detailed description of `BayesWave`. In chapter 4 I describe the methods and results of waveform reconstructions obtained with `BayesWave` and use them to perform signal consistency tests, investigate unmodeled features, and infer physical quantities without the use of templates. This chapter includes my original work in [43], and collaborative works with Chatziioannou et al.[48] and Ferguson et al [49]. In chapter 5, I design and implement a simple test of GR by studying the residual obtained by subtracting the best-fit template from the detector data. This chapter also includes collaborative work with Johnson-McDaniel et al [44]. In chapter 6, I describe the methodology we use to improve the detector data quality using `BayesWave`. This chapter includes my original work whose publication is in preparation. In chapter 7 I discuss various approaches to detect the post-merger signal from BNS events. I also discuss methods to combine or stack multiple BNS events when no single BNS has a detectable post-merger signal. This chapter includes collaborative work with Easter et al [47] and preliminary stacking work with Megan Arogeti, a graduate student at Georgia Tech. In addition to the individual works listed in each of chapters 4-7, all four chapters include results of data analysis and code development work I carried out as part of the LIGO and Virgo collaboration [7, 8, 9, 50, 51].

CHAPTER 2

GRAVITATIONAL WAVES

Issac Newton published his theory of Gravity in July 1687. For more than two centuries, this was the accepted theory used to describe the motion of celestial bodies [52]. It correctly predicted the motion of planets, the movement of stars in the celestial sphere, and the trajectories of air-borne bodies on earth. However, Newton's gravity required the existence of an inertial frame - the only frame at absolute rest. It elevated time above the spatial dimensions, and the flow of time was thought to be absolute regardless of the frame of the observer. It also did not place any limitation on the maximum speed attainable by a body. All of this came to a head when Newton's gravity, along with his theory of motion [52], came at odds with Maxwell's equations of electromagnetism, which would not retain their mathematical form upon going from one frame of reference to another [53]. Newtonian physics also necessitated that the universe has a preferred direction for the flow of light the and a change of direction or reference frame meant a change in the speed of light observed in that frame.

This inspired Albert Einstein to develop the special theory of relativity [54], which postulated that for observers in an inertial frame of reference (i.e. a frame that is not undergoing acceleration), the laws of physics are invariant, and the speed of light in vacuum is the same for all observers regardless of the motion of the observer or the light source. In this theory, time, like space, is also a coordinate, and its measurement is frame dependent. The theory of special relativity, or special relativity, solved the inconsistency in Maxwell's equations [55].

Special relativity only works when gravity is negligible and fails in strong gravity such as near a black hole. To extend his theory to frames in large gravitational potentials, Einstein developed General Relativity (GR) which reinterpreted space and time as a 4-

dimensional geometric entity that could curve due to matter or energy. GR received its first validations by correctly predicting the perihelion precession of Mercury, the observation of gravitational redshift, and the correct prediction of the deflection of the light from stars, visible during a solar eclipse.

GWs are a prediction of GR, in much the same way as electro-magnetic waves are a natural consequence of electro-magnetic theory. GR extends Newton's gravity to the non-linear regime of high masses and high velocities. Unlike the electro-magnetic force, however, gravity is a weakly interacting force, and GWs passes through objects effectively unperturbed. This also makes GWs a promising tool for studying the universe, as they contain un-corrupted information about the objects they originate from.

Due to the very weakly coupling nature of gravity, GWs emitted by bodies smaller than astronomical masses are extremely feeble and impossible to detect. For example, GWs from coalescing compact bodies such as black holes (BHs) and neutron stars NSs from a few hundred megaparsec (Mpc), have strain amplitudes $(O)(10^{-21})$ [4]. These waves can be detected by ground-based interferometric detectors such as the Laser Interferometer Gravitational-Wave Observatories (LIGO) in Hanford, WA, Livingston, LA [3], Virgo in Pisa, Italy, and most recently commissioned, the Kamioka Gravitational Wave Detector (KAGRA), Japan [56], and the planned LIGO India [57]. The next few sections describe the observable effects of GWs, the methods of observing them, and their expected sources.

2.1 General Relativity and Einstein field equations

Einstein Field Equations, are a set of 16 coupled non-linear second-order partial differential equations that encapsulate the dynamical properties of space-time. Mathematically,

$$R_{\mu,\nu} - \frac{1}{2}Rg_{\mu,\nu} = \frac{8\pi G}{c^4}T_{\mu,\nu}, \tag{2.1}$$

where $R_{\mu,\nu}$ is the Ricci curvature tensor, R is the Ricci curvature scalar, $g_{\mu,\nu}$ is the space-time metric, $T_{\mu,\nu}$ is the stress-energy tensor. G and c are respectively the gravitational constant and the speed of light in vacuum. We work in natural units where $G = c = 1$. The subscripts μ and ν are dummy variables that denote each dimension and take integer values of $[0-3]$ with 0 representing the time dimension and each of $1, 2, 3$ representing the spatial dimensions. Together, Equation 2.1 represents 16 coupled equations.

The left-hand side of Equation 2.1 describes the dynamics. $R_{\mu,\nu}$ and R are both second-order partial differential functions of $g_{\mu,\nu}$. The metric ($g_{\mu,\nu}$) describes the local properties of space and time. Given two events separated by space-time coordinates (dx^0, dx^1, dx^2, dx^3), the interval is defined as

$$ds^2 = g_{\mu,\nu} dx^\mu dx^\nu. \tag{2.2}$$

Here we use the Einstein summation convention that an index repeated in a subscript and superscript implies summation: $A_\mu B^\mu = \sum_{i=0}^{3} A_i B^i$.

In a flat space and time, $g_{\mu,\nu} = \eta_{\mu,\nu}$ where

$$\eta_{\mu,\nu} = \begin{pmatrix} -1 & 0 & 0 & 0 \\ 0 & 1 & 0 & 0 \\ 0 & 0 & 1 & 0 \\ 0 & 0 & 0 & 1 \end{pmatrix}, \tag{2.3}$$

is called the Minkowski metric.

The right-hand side of Equation 2.1 is the *source term* with local energy and momenta that curves space and time. Solving Equation 2.1 is a non-trivial task and analytical solutions exist only for the simplest one-body systems such as a stationary non-rotating black hole (Schwarzchild's solution) or a rotating black hole (Kerr's solution).

One of the solutions to these equations is GWs, perturbations to the metric caused

by a time-varying mass quadrupolar moment. Here, we show a reduced version of their derivation. We write the perturbation as:

$$g_{\mu,\nu} = \eta_{\mu,\nu} + h_{\mu,\nu}, \tag{2.4}$$

where $\eta_{\mu,\nu}$ is the familiar space-time metric, and $h_{\mu,\nu}$ is the perturbation.

Plugging this back into Equation 2.1, and gives us

$$\Box \bar{h}_{\mu,\nu} = -16\pi \bar{T}_{\mu,\nu}, \tag{2.5}$$

where $\Box = \eta_{\mu,\nu}\partial^{\mu}\partial^{\nu}$, and X denotes $\bar{X}_{\mu,\nu} = X_{\mu,\nu} - \frac{1}{2}X\eta_{\mu,\nu}$.

In vacuum, i.e., away from any energy and momentum, Equation 2.5 reduces to

$$\Box \bar{h}_{\mu,\nu} = 0, \tag{2.6}$$

which is a wave equation with a solution of the form

$$\bar{h}_{\mu,\nu} = A_{\mu,\nu}(k)e^{ik_{\alpha}x^{\alpha}}, \tag{2.7}$$

where k_{α} is the wave vector, x^{α} is a point in space-time and $A_{\mu,\nu}$ is the polarization tensor. Plugging this in Equation 2.6 we get

$$k_{\mu}k^{\mu} = 0, \tag{2.8}$$

which means that the k_{μ} is a null vector and so GWs travel at the speed of light. In the Lorentz gauage, we have $\partial^{\nu}\bar{h}_{\mu,\nu} = 0$. Applying this to Equation 2.6 we get

$$A_{\mu,\nu}k^{\nu} = 0, \tag{2.9}$$

which implies that GWs are transverse since the inner product of the polarization tensor with the propagation vector is 0. In the transverse traceless guage, which forces the trace of $\bar{h}_{\mu,nu}$ to be zero, $h = h^{\nu}_{\nu} = 0$,

$$\bar{h}_{\mu,\nu} = h_{\mu,\nu}. \tag{2.10}$$

We also enforce that the perturbation be only spatial in nature:

$$h_{0,0} = h_{0,i} = 0 \tag{2.11}$$

We are then left with 10 - 4 - 4 = 2 degrees of freedom.

$$h_{\mu,\nu} = \begin{pmatrix} 0 & 0 & 0 & 0 \\ 0 & h_{+} & h_{\times} & 0 \\ 0 & h_{\times} & -h_{+} & 0 \\ 0 & 0 & 0 & 0 \end{pmatrix} \cos(\omega(t-z)), \tag{2.12}$$

where h_{+} and $h_{\times}$ are the two GW polarizations, and the direction of the wave propagation is $k_{\mu} = (\omega, 0, 0, -k)$.

2.2 Gravitational Waves: effect and measurement

As shown above, GWs are transverse waves with two polarizations: $h_{+}(t)$, or *plus*, and $h_{x}(t)$, or *cross*. The qualitative effect on a ring of test masses is that the circle deforms into an ellipse; it expands in one direction, and contracts in the perpendicular direction. The crest of the wave corresponds to maximal expansion in one direction (and maximal contraction in the perpendicular direction). The ellipse then relaxes to its original circular shape and deforms in the perpendicular direction. The series of expansions and contractions cycle through with a frequency equal to the GW frequency [58]. Similar to electro-magnetic waves, GWs have two independent polarizations with the difference that the polarizations are separated by 45 degrees, rather than 90 degrees. Figure 2.1 shows the effect of the

two polarization modes of a passing GW on a ring of freely floating test masses, where the direction of wave propagation is transverse to the page.

Interferometric GW detectors such as LIGO and Virgo exploit this property to measure the GW waveform [59] with an L-shaped apparatus similar to a Michelson Interferometer. The corner of the "L" houses a 125 W monchromatic infrared frequency Laser [3, 6]. The Laser light is split by a beam splitter into two equal beams, which propagate through two perpendicular arms, the x-arm and the y-arm, of equal length (4km for LIGO, 3km in Virgo). The arms are under vacuum. The ends of each arm house suspended test masses from which extremely sensitive mirrors are suspended. The mirrors reflect the light at the corner station. As the two beams recombine, the interference pattern is detected by a photodetector placed at the corner station. A photodetector monitors the point of destructive interference (dark fringe) of the beams which makes it sensitive to minuscule changes in the detector arm lengths. A passing GW perturbs the lengths of the arms, and the resulting interference pattern is measured by the photodetector, converted to a digital time-series signal. Figure 2.2 shows the locations of current and planned second-generation GW detectors. In addition to these, third-generation detectors such as the Einstein Telescope [60] and Cosmic Explorer [61] have been proposed for the next decade.

I now describe the principle behind detecting GWs. Assuming the form of $h_{\mu,\nu}$ from Equation 2.12, and including only the plus polarization for simplicity, the metric $g_{\mu,\nu}$ due to a passing GW traveling along the z-direction is

$$g_{\mu,\nu} = \begin{pmatrix} -1 & 0 & 0 & 0 \\ 0 & 1+h_{+} & 0 & 0 \\ 0 & 0 & 1-h+ & 0 \\ 0 & 0 & 0 & 1 \end{pmatrix}. \tag{2.13}$$

If we assume that L is the length of each arm of the detector when there is no passing GW, then the length of the x-arm due to the GW metric perturbation is $L_x = L(1+h_{+})$ and that

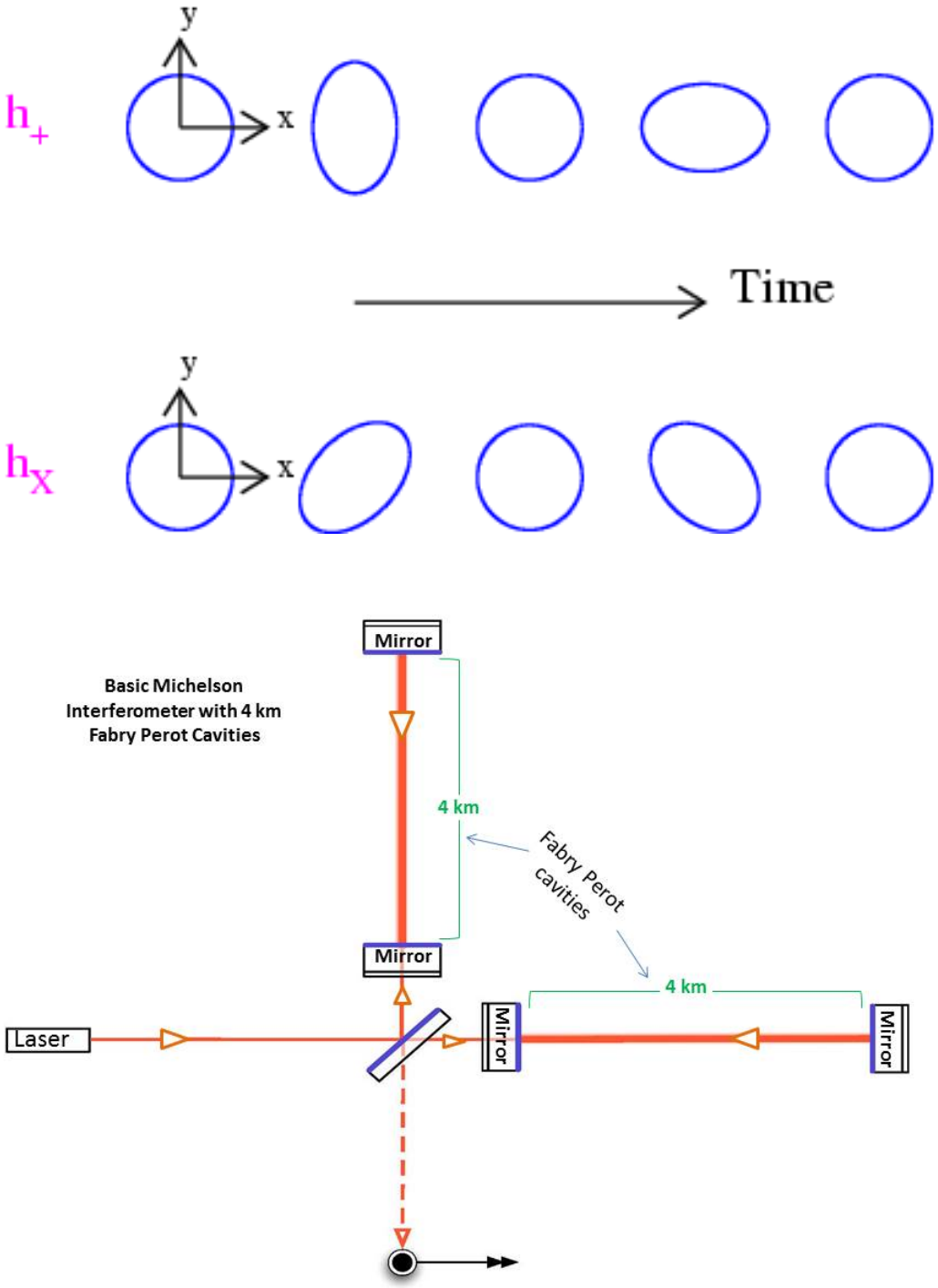

Figure 2.1: Laser interferometer detection principle. The plot on the top shows the (highly exaggerated) effect of a passing GW on a ring of masses through time. Image credit: [58]. The plot on the bottom is a simplified schematic of the LIGO detectors. A GW passing through the plane of the paper would cause a series of expansions and contractions of the horizontal (X) and vertical (Y) arms. Image credit: LIGO Labs

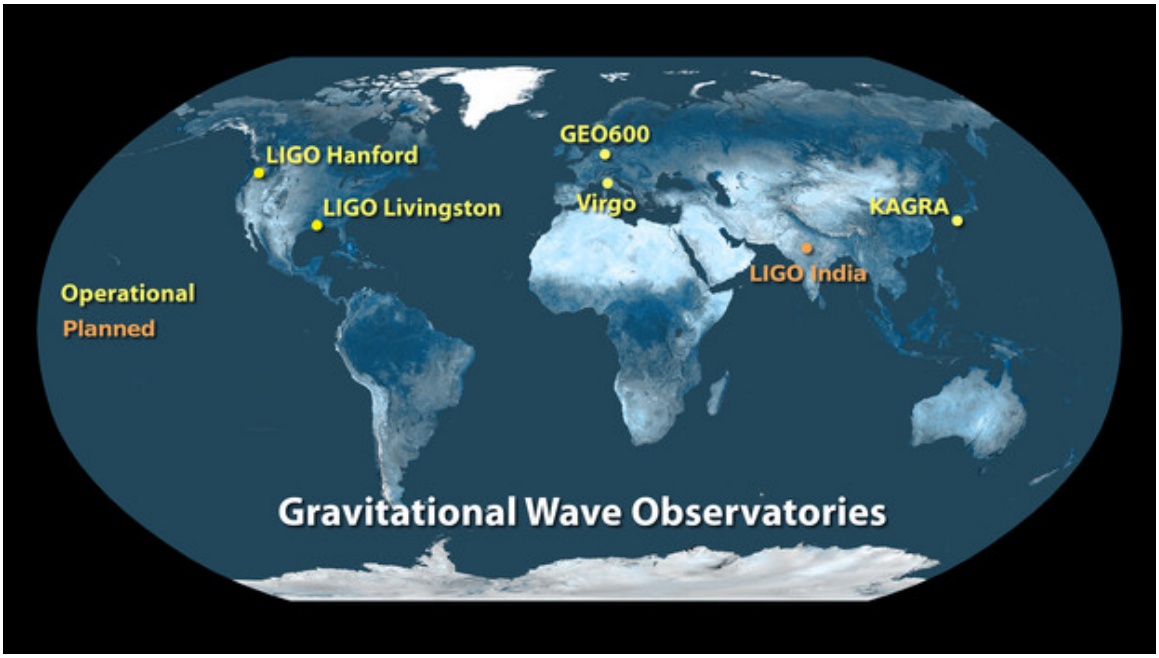

Figure 2.2: Network of first and second-generation GW detectors across the globe. Credit LIGO Labs

of the y-arm is $L_y = L(1 - h_+)$. The difference in the lengths of the arms is what we detect at the photodetectors. So,

$$L_x - L_y = 2Lh_+, \tag{2.14}$$

or

$$h_+ = \frac{\Delta L}{2L}, \tag{2.15}$$

where $\Delta L = L_x - L_y$ is the difference in the lengths of the two detector arms. Therefore, the GW readout channel is often referred to as the *strain* channel as it measures the fractional change in the arm lengths, although it differs from the elastic strain caused by mechanical stress.

In general, GWs can arrive from any direction in the sky. The sensitivity of ground-based detectors is dependent on the sky location through the antenna pattern functions, F_+

and $F_\times$ [62]:

$$\begin{aligned} F_+(\theta,\phi) &= (1+\cos^2\theta)\cos 2\phi\cos 2\psi + \cos\theta\sin 2\phi\sin 2\psi \\ F_\times(\theta,\phi) &= (1+\cos^2\theta)\cos 2\phi\sin 2\psi + \cos\theta\sin 2\phi\cos 2\psi \end{aligned}, \tag{2.16}$$

where θ and ψ are the sky location coordinates and ψ is the polarization angle. The strain observed by the detector is then

$$h(t) = F_+ h_+(t) + F_\times h_\times(t). \tag{2.17}$$

Due to the weakly coupling nature of gravity, however, the fractional length change in the interferometer arms, or strain, is minuscule. For example, the peak value of the strain during the first GW detection, G150914, was $\sim 10^{-21}$ [63], corresponding to a length change of $\sim 10^{-18}$ m in a 4 km arm. At such values, the detector sensitivity is limited by various noise sources. Below 10 Hz, it is dominated by seismic noise such as ground motion, winds, anthropogenic noise, etc. Above 1000 Hz, the sensitivity is limited by quantum shot noise [64] and brownian motion of the mirror surface. The noise curves of these low and high frequency sources then result in a "sweet spot" between 10 and 1000 Hz where LIGO is most sensitive as shown in Figure 2.3.

The detector strain readout is the addition of the signal and noise,

$$d(t) = h(t) + n(t), \tag{2.18}$$

where $d(t)$ is the detector data time-series, $h(t)$ is as usual, the GW signal and $n(t)$ is the instrument noise. We model this noise as stationary Gaussian, i.e, over a long enough period of time T, its average is 0:

$$\langle n(t)\rangle = \frac{1}{T}\int_0^T n(t)dt = 0. \tag{2.19}$$

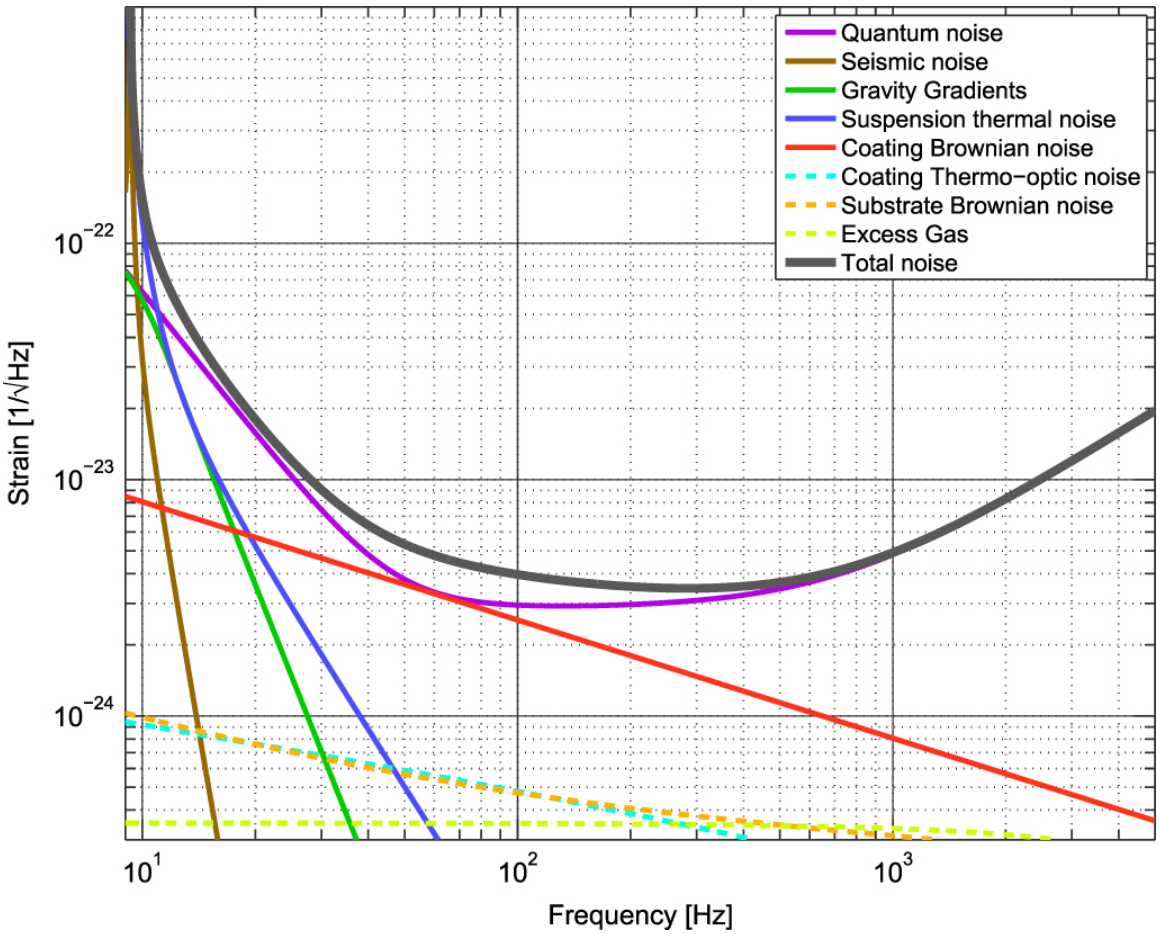

Figure 2.3: Noise sources in Advanced LIGO. Figure from [3]

The noise is "colored" and its spectrum is described by the Power Spectral Density (PSD),

$$\langle \widetilde{n}(f)\widetilde{n}^*(f')\rangle = \delta(f-f')S_n(f), \tag{2.20}$$

where $\widetilde{n}(f)$ is the fourier transform given by

$$\widetilde{n}(f) = \int_{\infty}^{\infty} e^{i2\pi ft} n(t)dt. \tag{2.21}$$

Assuming the detector noise is stationary and Gaussian [65], the PSD is the variance of the strain at each frequency. Figure 2.4 shows the noise Amplitude Spectral Density (ASD) (square root of the PSD) on June 04, 2019 for the LIGO and Virgo detectors as

well as GEO600, which is a 600 m interferometric detector. Because of the smaller length, GEO600 is less sensitive compared to the other detectors in the network but has the the advantage of being easier to test new technologies on [66].

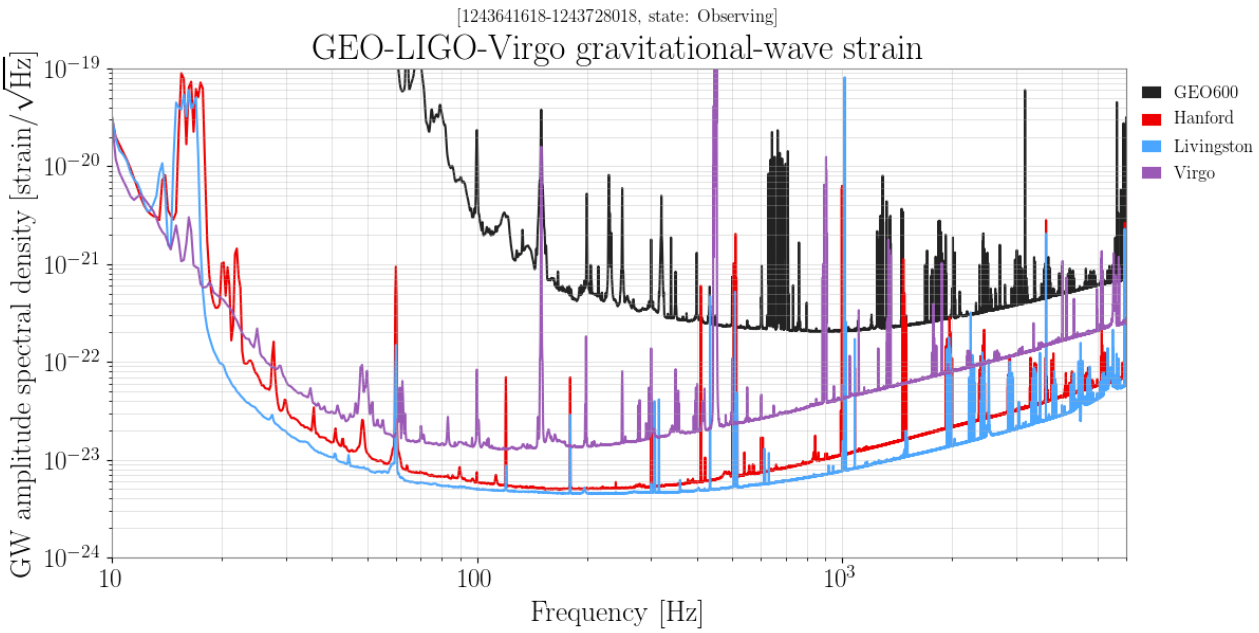

Figure 2.4: Sensitivity of the LIGO-Hanford (red), LIGO-Livingston (blue), and Virgo (purple) detectors on June 04, 2019. The plot also shows the ASD of GEO600 a 600m arm-length GW detector in Starstedt, Germany, currently used as a test-bed for new technologies. Image credits: Gravitational Wave Open Science Center

The very sensitive nature of the detector also makes it susceptible to disturbances from the environment or the internal control system. Occasionally, transient noise events, also known as "glitches" corrupt the detector data [11]. From a data-analysis perspective, these glitches manifest as non-Gaussianities of excess amplitude. Glitches are often caused by various non-astrophysical sources such as winds, train tracks, earthquakes, or imperfections in the detector control system [64, 11]. They typically occur every few hours and usually do not coincide with the glitches in other sites. These glitches can sometimes mimic the morphology of a GW and cause a false detection by GW search algorithms [64]. They can also affect offline analyses such as source inference and signal reconstructions.

Future improvements such as A+ upgrade to LIGO [67] are expected to mitigate some

of these noise transients. Additionally, future generation detectors such as Cosmic Explorer (CE) [61], Einstein Telescope (ET) [68, 60], NEMO [69], and space missions such as the laser interferometer space antenna (LISA) [70] are in various stages of development and will dramatically increase our sensitivity to various GW sources.

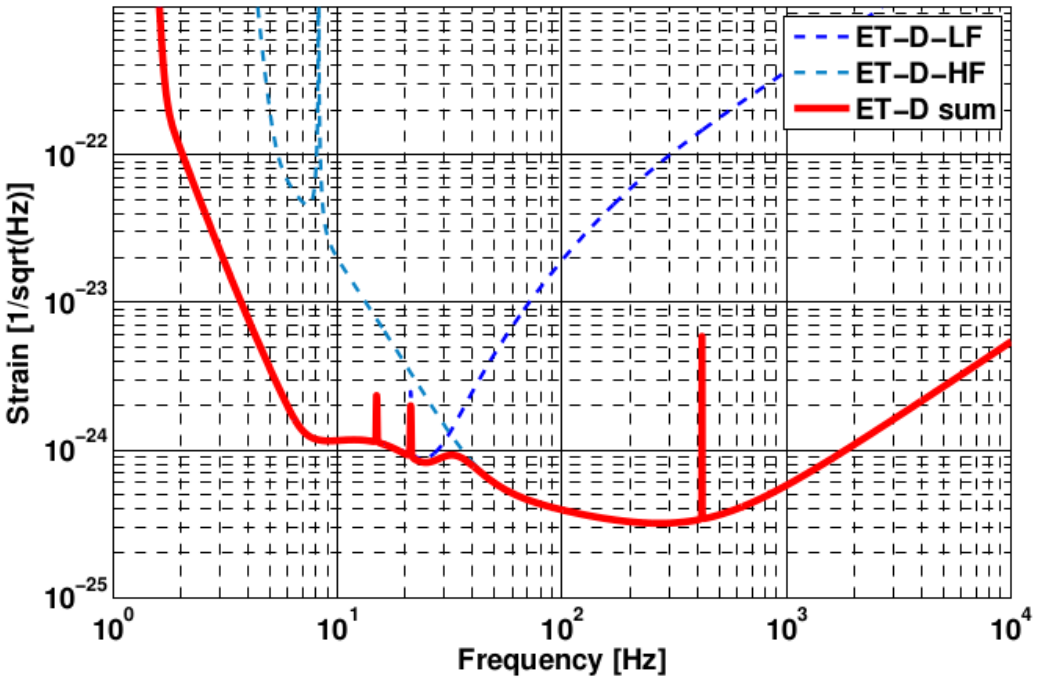

Figure 2.5: Einstein Telescope sensitivity. The plot shows the low frequency (dark blue dashed line) and high frequency (light blue dashed line) sensitivity curves, and the combined sensitivity curve (red solid line). Figure from [71].

The Einstein Telescope (ET) is a proposed third-generation detector by the European Commission that is expected to be operational by the first half of the 2030s. The geometry of ET will be different from LIGO and Virgo; it will have three corner stations placed 10 km apart in an equilateral triangle, effectively making three nested detectors as shown in Figure 2.6. To shield it from seismic noise at frequencies 3 - 100 Hz, it will be built 100 m to 200 m underground. Each detector station will have two interferometers with distinct hardware strategies to focus on the different frequency ranges. The low frequency (1.5 Hz to 30 Hz) interferometer will be cryogenically cooled 10 Kelvin, while the high frequency

(30 Hz to 10 kHz) interferometer will operate at room temperature. The effective sensitivity would be the combination of the two as shown in Figure 2.5. ET's low-frequency sensitivity will substantially improve our ability to detect the early inspiral of stellar ($< 100M_{\odot}$) and intermediate-mass ($100M_{\odot}$ to $1000M_{\odot}$) binaries, while its high-frequency sensitivity will improve the detectability of the merger phase of stellar-mass compact binary coalescences (CBCs), core-collapse supernovae, and continuous waves from asymmetric NSs.

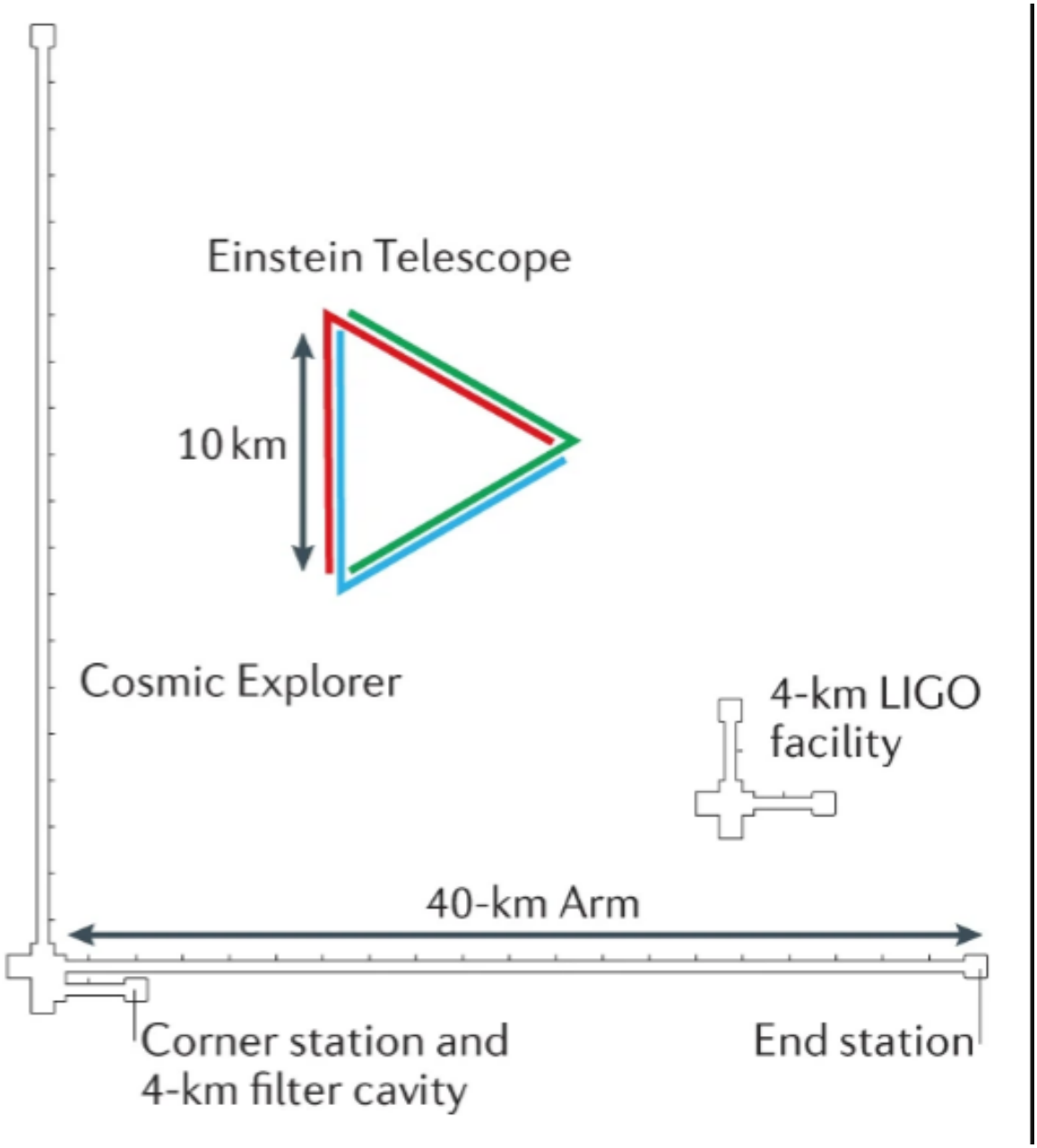

Figure 2.6: Einstein Telescope, Cosmic Explorer schematic cartoon. Figure from ego-gw.it

Cosmic Explorer (CE) is a proposed third-generation detector in the United States, with an "L" shaped geometry placed above the ground, similar to the current second-generation detectors as shown in Figure 2.6. The current proposal envisions multiple possible scenarios based on the relevant science goals, with arms lengths ranging from 10 km to 40 km, and one or two detectors placed sufficiently far apart from one another, similar to the current twin LIGO detectors. Figure 2.7 shows the CE sensitivity curves for various arm lengths with the compact binary (CB) and post-merger (PM) optimized configurations.

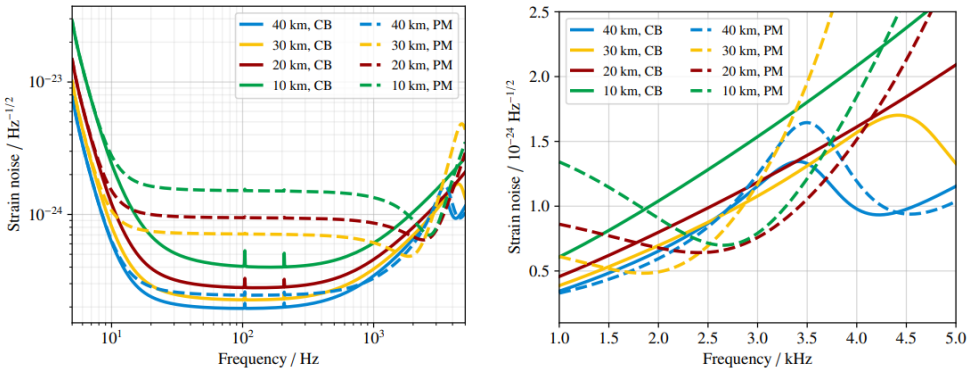

Figure 2.7: Cosmic Explorer sensitivity for various observation configurations and science goals. Figure from [61]

LISA is a planned space-based mission by the European Space Agency (ESA) with smaller contributions from the US National Aeronautics and Space Administration (NASA) to study GWs in the millihertz band. It is expected to fly in the first half of the 2030s. Similar to ET, it will exhibit an equilateral triangular with arm lengths of 2.5 million km. The corners spacecraft will make a plane that is inclined at 60 degrees with the earth's orbit, and the whole constellation will trail behind the earth by 20 degrees. LISA will be able to observe tens of thousands of astrophysical sources ranging from mergers of white dwarf binaries in the Milky way, the merger of massive black holes ($M_T = 10^4 M_\odot$ to $M_T = 10^7 M_\odot$), from redshifts beyond the reionization epoch, extreme mass-ratio inspirals (EMRI, $m_2/m_1 < 0.01; m_2 < m_1$) [70].

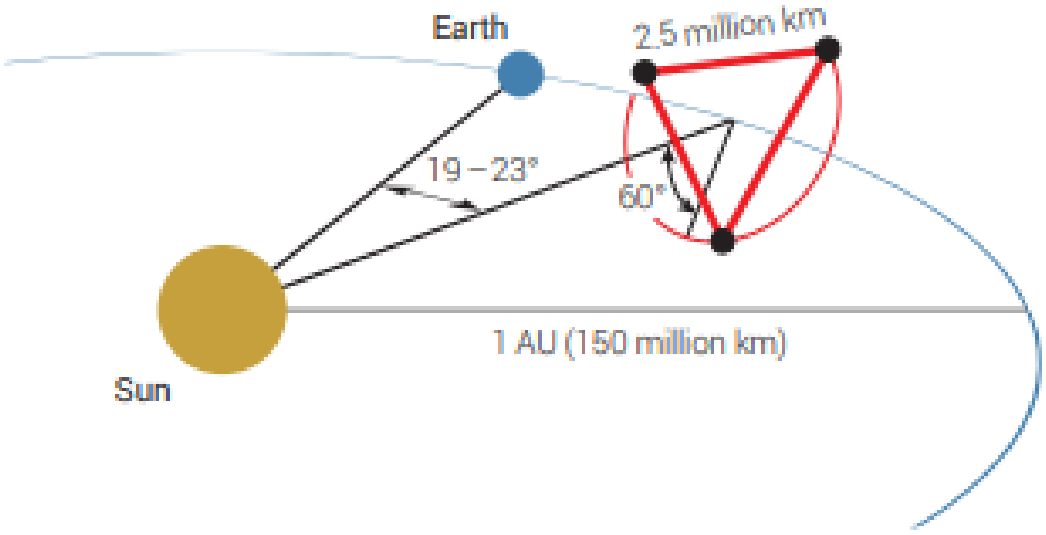

Figure 2.8: Cartoon plot showing the LISA constellation in a heliocentric orbit with its plane oriented at 60 degrees to the plane of earth's orbit. Figure from [70]

ET, CE, and LISA will also provide early warning alerts for stellar-mass CBCs to LIGO and EM observatories due to their sensitivity to the lower frequencies.

Pulsar timing arrays are another interesting detection method. Pulsars are rotating neutron stars or white dwarfs stars that emit jets of electromagnetic radiation out of their magnetic poles [72]. These poles are usually at an inclination to their rotating axes with the result that the jets are detected on earth as discrete pulses. Due to the density and stability of the rotating period of neutron stars, the time between these pulses is extremely precise and in some cases rivals the accuracy of atomic clocks. Pulsars with a pulse period of the order of milliseconds are called millisecond pulsars [73], and the international pulsar timing array (IPTA) [74] uses 30 such millisecond pulsars to detect GWs. The principle here is that a passing GW would perturb the delays in the pulses which would then be detectable.

Figure 2.9 shows the sensitivity curves of LIGO, Virgo, ET, CE, LISA, and IPTA, and the amplitude spectra of some of the various possible GW sources.

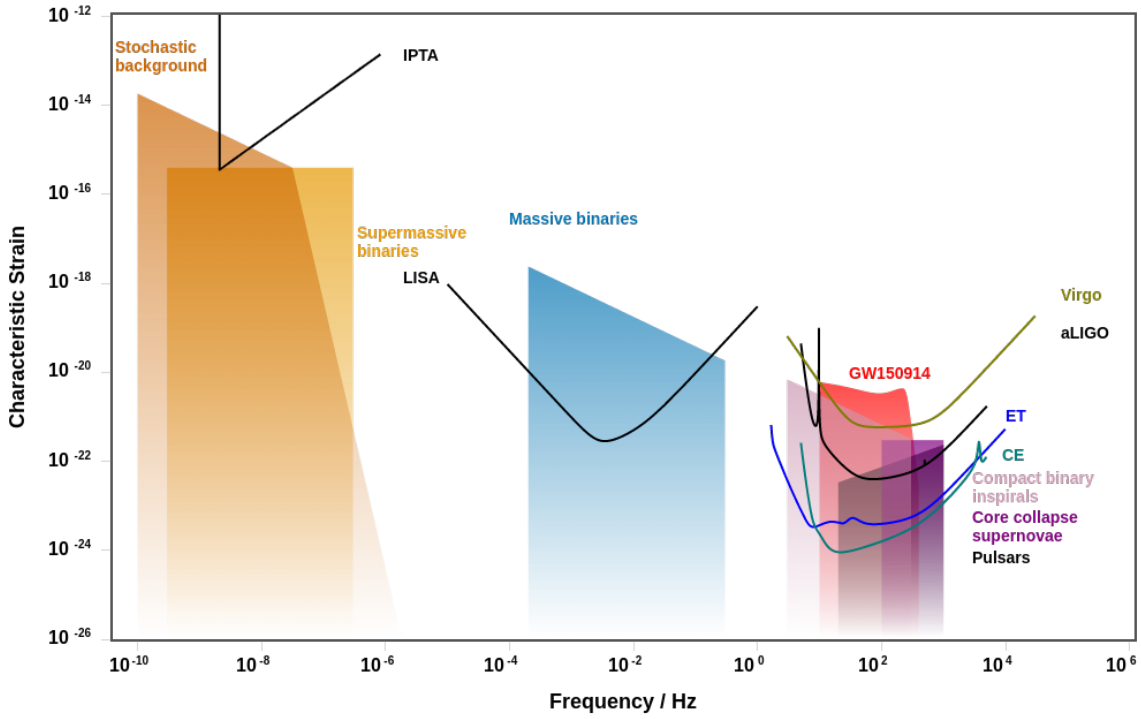

Figure 2.9: Sensitivity and source spectra plots. Plots show the sensitivity of LIGO (black), Virgo (green), ET (blue), CE (teal), LISA (black), IPTA (black), and the various strain amplitude and frequency regions of some of the predicted GW sources. Plots made using [75]

2.3 Gravitational Waves: astrophysics

GWs are challenging to detect due to the weak coupling property, but this also makes them effectively immune to absorption by matter in the line of sight, in contrast with electromagnetic waves. Another fundamental difference between GWs and electromagnetic waves is the typical length scales of the physics they represent. While the latter carries information about the micro-scale interactions of the system, the former is a function of the macro-scale properties [76]. For example, electromagnetic waves emitted by pulsars are dictated by the interaction of particles at the subatomic scale and their wavelengths are typically much smaller than the scale of the pulsar. On the other hand, GWs emitted by BNSs are dictated by the bulk mass of the component NSs, their angular momenta, etc, and their wavelength is typically greater than or similar to the scale of the system.

One can therefore see that GWs present a new window to observe the universe and can help solve several previously unsolved problems. As of this writing, the LIGO and Virgo collaboration has released three GW transient catalogs (GWTC-$\{1,2,3\}$) which respectively contain events from the first and second observing run (O1+O2), the first half of the third observing run (O3a), and the second half of the third observing run (O3b). Cumulatively, these include 82 BBH, 2 neutron star-black hole (NSBH), and 2 BNS, and 4 events consistent with both BBH and neutron star-black hole (NSBH) models [77] [7, 8, 9]. These detections have led to a wide range of astrophysical implications.

For example, before 2015, X-ray detections of galactic BBH systems had led to total mass upper limits of $\sim 10M_{\odot}$ [78]. The total mass of GW150914 was $\sim 65M_{\odot}$ which presented a new population of mass ranges unknown to us [79]. Prior to GW detections, our estimates of BH spins relied on modeling accretion disks and inferring the X-ray spectra. However, spins estimated from GWs rely exclusively on the vacuum solution of GR.

GW170817 is so far, the only GW event that also had associated detections in EM observatories [80]. The gamma-ray burst (GRB) emitted from the source was detected by the Fermi [81] and INTEGRAL satellites[82] 1.7 seconds after the merger time in LIGO/Virgo. GW170817 was the first confirmation that short GRBs occur in BNS mergers, and was the first link between GWs, GRBs and kilonovae. The event was observed by over 70 earth and space-based observatories and remains the most observed (in terms of the number of independent observations) astrophysical event till-date.

GW190521 originated from the merger of pair of BHs of masses 85 $M_{\odot}$ and 66 $M_{\odot}$ [83, 84]. The larger BH's mass is consistent with the mass-gap predicted by the pair-instability supernova theory [85] and the detection helped characterize the formation possibilities of BHs in this mass gap through various channels: multiple stellar coalescences [86], or via hierarchical mergers of lower-mass black holes in star clusters [87] or in active galactic nuclei [88]. The remnant's mass was 150 $M_{\odot}$ which led to the first direct observation of an intermediate-mass BH (IMBH) system [89]. The existence of IMBH systems helped

confirm the formation mechanism of supermassive BH systems (M_T = $10^6 M_\odot$ to $10^9 M_\odot$) at the centers of galaxies and globular clusters.

GW190814 was likely the first detection of GWs from a black hole and neutron star (NSBH) pair [90]. The system had (at the time), the most unequal mass ratio of m_2/m_1 = $0.112; m_2 < m_1$. Several astrophysical channels predict the existence of binaries with mass ratios similar to GW190814. However, the combination of mass ratios, component masses, and inferred merger rate challenges all current population synthesis models for the formation and mass distribution of compact object binaries [91, 92, 93, 94, 95].

The latest catalog of events [9] constrains the constrain three types of merger rates compact binaries:between 13 $\text{Gpc}^{-3}\text{yr}^{-1}$ to 1900 $\text{Gpc}^{-3}\text{yr}^{-1}$ for BNSs, between 7.4 $\text{Gpc}^{-3}\text{yr}^{-1}$ to 320 $\text{Gpc}^{-3}\text{yr}^{-1}$ for neutron star-black holes (NSBHs), and between 17.3 $\text{Gpc}^{-3}\text{yr}^{-1}$ to 45 $\text{Gpc}^{-3}\text{yr}^{-1}$ at redshift (z=2) [96]. It also constraints the current value of the Hubble constant H_0 =68^{+13}_{-7} km s^{-1} Mpc^{-1} (68%) after the inclusion of GW170817 and its EM counterpart.

2.4 Compact Binary Coalescences (CBC)

Binaries comprising of compact objects, BHs and NSs, are highly dynamical systems with extremely high densities and velocities. As their orbits shrink, the dynamics eventually fall into the strong-field regime of GR. The coalescence evolves in three separate phases: inspiral, merger, and ringdown as shown in Figure 2.10. In the inspiral phase, the binary loses energy and angular momentum in the form of GWs. It also sheds its eccentricity and the orbit becomes quasi-circular [18]. The radius of the orbit shrinks, the orbital frequency (and the GW frequency, which at the leading order, is twice the orbital frequency) also increases. This causes the orbit to shrink faster as time passes. The frequency, amplitude, and energy emitted go up very quickly in the last few cycles resulting in a *chirp*-like signal as in Figure 2.10. During the merger, the objects combine into a remnant BH (or NS in some BNS mergers). When the remnant is a BH, it sheds its asymmetry in the form of ringdown quasi-normal modes (QNMs) [97]. The precise morphology and phase evolution

of the waveform is dictated by the parameters of the system.

The frequency spectrum of a CBC signal inversely scales with the total mass (M_T) i.e., increasing the M_T by a factor of 10 shifts the frequency spectrum to lower values by an order of magnitude. CBC systems in the stellar mass mass range ($1M_\odot < M_{Total} < 100M_\odot$) enter the sensitive band of LIGO and Virgo ($20 - 1000$ Hz) [59] just a few seconds before the merger, just as their GW emission becomes extremely energetic. For example, 4.8% of the total mass of the system was emitted in the GW150914 event. In the 0.2 seconds it spent in LIGO's sensitive frequency band, it outshone all radiation received by the earth from the visible part of the electromagnetic spectrum.

2.5 GW astronomy: state of the art

In the past few decades, there have been several developments in the fields of modeling and Bayesian inference towards the goal of efficiently searching GWs from detector data and inferring parameters of the systems they originate from [98, 99, 42].

Inference algorithms offer "best-fit" signal reconstructions and probability distributions on the source parameters by comparing model waveforms with detector data. These models are obtained by solving Einstein's field equations through various methods.

Analytical solutions of GR for CBC systems exist but do not capture the entire dynamics, especially the highly non-linear effects of GR in the late inspiral [30, 31, 32, 33, 100]. Exact solutions from numerical relativity (NR), are computationally expensive, with each multi-core simulation taking up to several weeks and they cannot directly be used to explore an uncertain parameter space with arbitrary precision. In some cases, simulations for the system of interest simply don't exist with full physics [34, 35, 36], and semi-analytical approximations of GR solutions to CBC systems have been developed for fast waveform model generation . These are used in template-based methods, where the signal in the detector is modeled as a function of the physical properties of the system such as its mass, spins, location, etc [101].

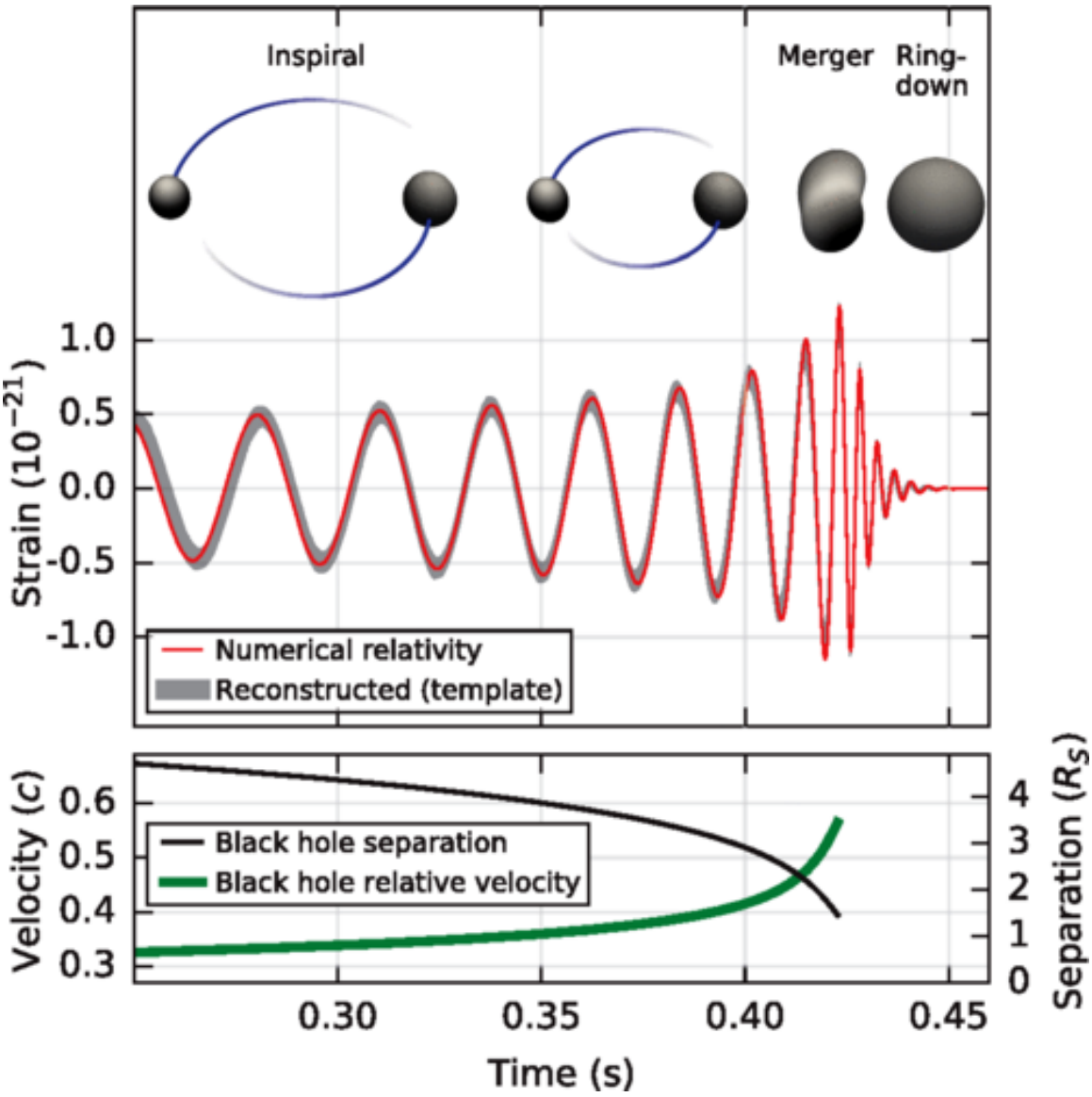

Figure 2.10: GW150914 phases. The top panel shows a cartoon depiction of the phases of the coalescence: inspiral merger and ringdown, and, GW waveform reconstructed by numerical relativity (red) and GR-based templates (grey). The bottom panel shows the relative separation between the black holes (black) and the relative velocity (green). Figure from [63]

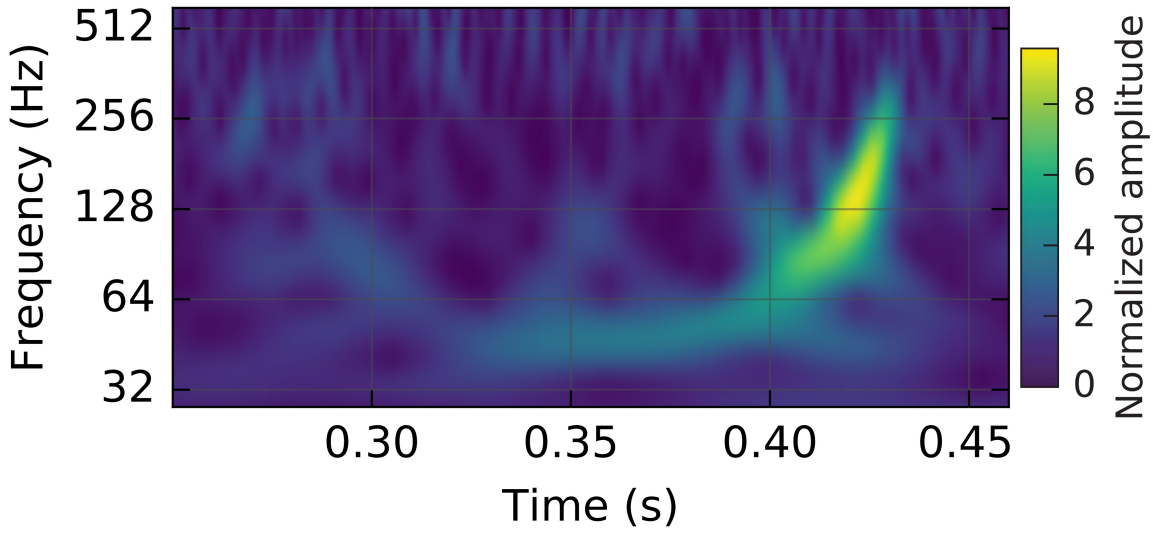

Figure 2.11: Time-frequency heat map of the data at the time of GW150914 as observed by the LIGO Hanford detector. The y axis is the frequency and the x-axis is the time in seconds after the nearest integer GPS second. The brightness of the pixel corresponds to the amplitude of the signal observed by the detector. The *chirp* is visible as the collection of yellow pixels from ~ 0.35 s to 0.45 s going up in frequency and brightness. Credit: LIGO Labs

There have also been advancements in *burst* waveform models, which project the GW signal waveform on a wavelet basis [42] [40]. Unlike templates, therefore, burst models are not constrained by limitations in waveform modeling due to uncertain physics or computational considerations.

In their current form, templates methods may be poorly calibrated for complicated BBH systems such as highly precessing orbits, unequal mass ratios, eccentric orbits, etc. Burst models provide a complementary means to study such cases. Even for less extreme and well-characterized systems, burst models provide a means of validating the results of templates by providing independent estimates of the best fit waveform morphology. For example, [4] characterizes the agreement between CBC and burst reconstructions on a set of simulated GW signals injected into real data.

The dynamics of BNS mergers are complicated by the presence of matter. As the NSs get close to each other, the point object approximation, which is valid for BHs, no longer holds, and the vacuum solution needs correction terms to account for tidal effects [102, 103,

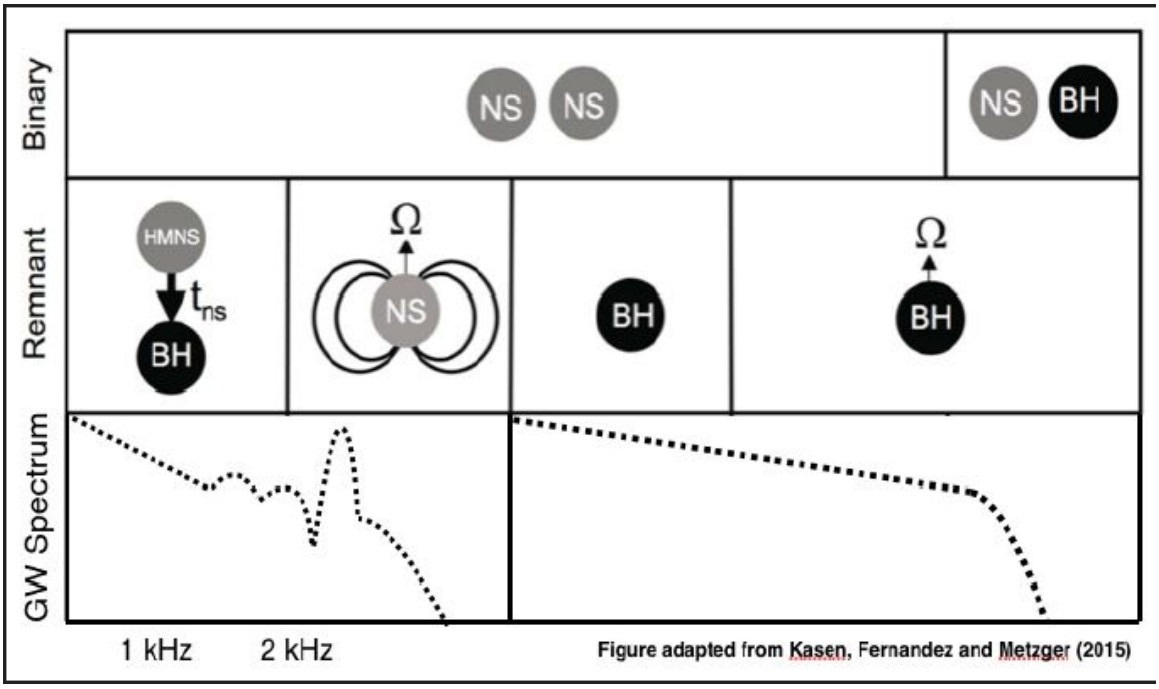

Figure 2.12: Post merger scenarios cartoon. The top row shows the two types of CBC systems containing NSs. The middle row shows the possible fates of the remnant. The bottom row shows the morphology of the GW spectrum emitted by the remnant. Figure adapted from [108].

104]. The effect of the NS equation of state (EOS) is imparted into the phase evolution of the late inspiral [105]. Measuring these effects helps us place constraints on EOS models as has been done in [106, 107].

Complementary information on the EOS is encoded into the post-merger part of a BNS waveform[109, 110]. Kasen et al [108] describe the four major possibilities of a BNS coalescence and the characteristic time scales of GW emission as shown in Figure 2.12. The first is the prompt collapse into a BH which causes GW emissions at frequencies above 6 kHz, where LIGO and Virgo are dominated by quantum shot noise. The second is a short-lived hypermassive NS (HMNS) which is supported by differential rotation and thermal gradient with an approximate emission time scale of 10 ms. The third is a short-lived supramassive NS (SMNS) which is supported by differential rotation with an approximate emission time scale of 100 ms. The fourth possibility is of a stable NS remnant with an emission time scale of a few seconds to weeks. Of the above, the HMNS and SMNS cases

are of interest to us, since they are more massive, and tend to have larger core density than their component NSs. Due to the complexity of the physical processes involved, however, modeling the post-merger dynamics is a highly non-trivial task, and simulation studies have only recently started unfolding their true nature. Studies such as [12, 13, 14] have shown that this short lived remnant emits GW radiation that peaks in the $1-4$ kHz frequency range for a variety of realistic EOSs. Burst methods present a promising tool to detect these post-merger GWs since they can accommodate any unexpected features, without the added cost associated with physically modeling those features.

CHAPTER 3

DECRYPTING THE GW SIGNAL: INFERENCE FROM DATA TO SOURCE

GW data analysis is a highly sophisticated pursuit with non-trivial challenges. The high-level workflow of the data analysis is as follows: we construct a model for the underlying signal waveform as a function of some parameter set $\vec{\theta} = \{\theta_1, \theta_2, .., \theta_n\}$. Then, we compare the data with the model waveform and sample the space of $\vec{\theta}$ till we get a sufficient agreement between data and model.

This task presents three major challenges. (i) GWs are minuscule disturbances in the fabric of space and time. Therefore, at the sensitivities required to detect these waves, non-astrophysical, terrestrial, and anthropogenic sources introduce noise in the detector [11]. Inferring the true GW from the data is akin to finding a needle in a haystack. (ii) The models we use to infer the waveform are not easy to construct as GR is a highly non-linear theory. (iii) The model parameters $\vec{\theta}$ represent a multi-dimensional space, and obtaining probability density functions by deterministically sampling the space requires a prohibitively high number of computations. Thanks to advances in instrumentation, waveform modeling, statistics, and computing power, these challenges have been surmounted.

In this chapter, I discuss the formalism and methods of numerical analysis applied to the data collected by the LIGO and Virgo detectors. I first introduce Bayes' theorem and its application for inferring the true waveform. I also introduce signal processing techniques and useful figures of merit. I then discuss various template-based and burst methods of the waveform. Next, I describe online low-latency *searches* that identify candidate GW signals. I then give an overview of parameter estimation analyses used to precisely determine the source properties of candidate events. Finally, I describe `BayesWave`, a burst algorithm for inferring the waveform, and its various use cases. The `BayesWave` algorithm is central to this thesis.

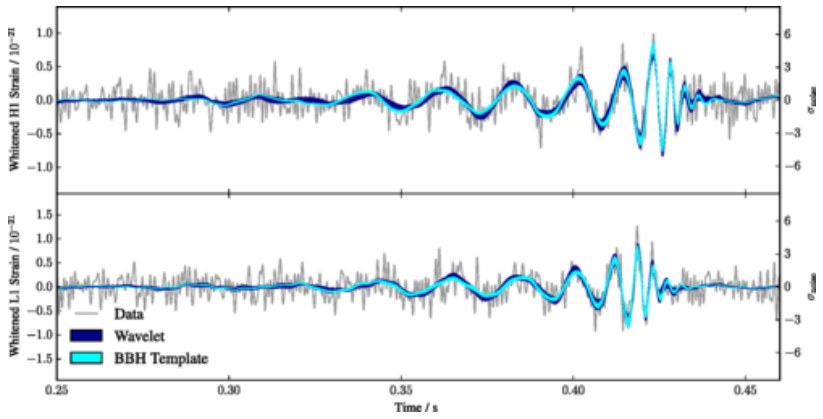

Figure 3.1: Time domain reconstructions of the template (blue) and wavelet (cyan) overlayed against detector data (gray) for GW150914. The top and bottoms panels correspond to LIGO Hanford and LIGO Livingston respectively. Figure from [79]

3.1 Bayesian inference of source properties

The Bayesian statistical approach of data analysis is to start with a set of prior "truths" and then update these truths with observations. This is in contrast with the frequentist approach which relies on multiple occurrences of events to make probabilistic statements. We restrict our focus to the Bayesian approach.

The properties of a detected signal are inferred by modeling the detector data $\mathbf{d}$ with the parameterized waveform $\mathbf{h}(\theta)$. The boldface here is to emphasize that $\mathbf{d}$ and $\mathbf{h}$ represent quantities in multiple detectors. $\vec{\theta}$ may represent a point in the parameter space of the underlying GR system such as masses, spins, and other extrinsic parameters (total of 17 parameters), or a point in the parameter space of wavelets such as the central frequency, amplitude, and the number of wavelets (up to hundreds of parameters). The data $\mathbf{d}$ are assumed to be a time series that contains the true GW signal, plus additive stationary Gaussian noise characterized by the one-sided noise PSD $S_n(f)$. We are interested in sampling the posterior probability distribution function of $\mathbf{h}$ given $\mathbf{d}$. According to Bayes' theorem [111, 112]:

$$p(\vec{\theta}|\mathbf{d}) = \frac{p(\vec{\theta})p(\mathbf{d}|\vec{\theta})}{p(\mathbf{d})}, \tag{3.1}$$

where $p(\vec{\theta})$ is the prior knowledge about the system. $p(\mathbf{d}|\vec{\theta})$ is the likelihood function, the probability of obtaining data $\mathbf{d}$ given the signal $\mathbf{h}(\vec{\theta})$:

$$p(\mathbf{d}|\vec{\theta}) \propto \exp\left(-\frac{1}{2}\langle \mathbf{d} - \mathbf{h}(\vec{\theta})|\mathbf{d} - \mathbf{h}(\vec{\theta})\rangle\right), \tag{3.2}$$

The posterior probability distribution function for a single parameter θ_1 can be obtained by *marginalizing* over the rest of the parameters

$$p(\theta_1|\mathbf{d}) = \int d\theta_2..d\theta_N p(\vec{\theta}|\mathbf{d}) \tag{3.3}$$

The denominator on the right-hand side of Equation 3.1 is called the *evidence* for the model which defines $\mathbf{h}(\vec{\theta})$ and is given by

$$Z = p(\mathbf{d}) = \int p(\vec{\theta})p(\mathbf{d}|\vec{\theta})d\vec{\theta}. \tag{3.4}$$

We compare two competing models M_1, M_2 using the ratio of evidences called the *Bayes Factor*:

$$BF_{1,2} = \frac{Z_1}{Z_2} \tag{3.5}$$

which quantifies how much more likely the data $\mathbf{d}$ are consistent with model M_1 as compared to model M_2

3.2 Signal processing methods

The $\langle\cdot|\cdot\rangle$ on quantities with boldface indicates the noise weighed inner product over the network of detectors given by:

$$\langle \mathbf{a}|\mathbf{b}\rangle = \sum_i^n \langle a^i|b^i\rangle, \tag{3.6}$$

here i sums over all n detectors in the network, and $\langle a^i|b^i\rangle$ is the inner product in an

individual detector defined as

$$\langle a^i | b^i \rangle \equiv 4\,\mathrm{Re} \int_0^\infty \frac{\widetilde{a}^i(f)\widetilde{b}^{i*}(f)}{S_n^i(f)} df, \tag{3.7}$$

$\widetilde{a}^i(f)$ is the Fourier transform of time series a^i, and the superscript $*$ denotes the complex conjugate. $S_n^i(f)$ is the PSD of the i^{th} detector. Dividing by the PSD effectively reweights the integral towards frequencies where the detectors are most sensitive. The optimal Signal to Noise Ratio (SNR) is defined as

$$\rho = \sqrt{\langle \mathbf{d}|\mathbf{d} \rangle}, \tag{3.8}$$

and is often used as a figure of merit for the strength of the signal in the detector.

3.3 Sampling multi-dimensional parameter space

Infer the posterior probability distribution function $p(\vec{\theta}|\mathbf{d})$. is not a trivial task. The computational cost of estimating the posterior function using deterministic methods is extremely high since the number of evaluations required to explore the parameter space on a fixed grid grows exponentially with the number of dimensions.

As an example, consider the parameter space of GW waveform parameters. As I will show in the next section, it is a collection of 17 parameters. Let's say for the sake of simplicity, to get an accurate estimate of the probability distribution in this parameter space, we require each parameter dimension to be sampled with 10^3 points. That scales to a total of 10^{51} points. Let's also assume that computing the likelihood of each point in the parameter space requires $\mathcal{O}(1)$ time (in reality, it scales as N log(N) where N is the number of samples in the waveform). That means we are required to do 10^{51} computations. The fastest super-computer in 2021, the *Fugaku*, [113], does approximately 10^{18} floating-point operations per second (FLOPS). To compute the posterior probability, it would require 3.16 x 10^{25} years - many times the age of the universe. Therefore, stochastic sampling-based

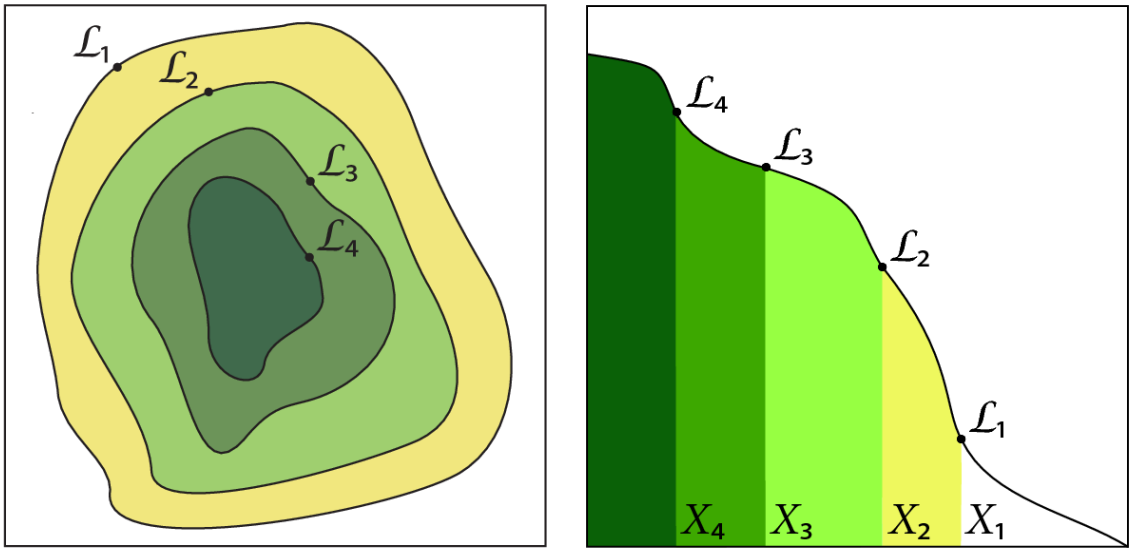

Figure 3.2: Cartoon illustration of nested sampling mapping a 2-D parameter space to a 1-D function. The multi-dimensional integral in Equation 3.4 is mapped to a one-dimensional integral over an inverse survival function (with respect to the prior mass) for the likelihood. Figure from [123].

methods such as Markov Chain Monte Carlo (MCMC) [114, 115, 116, 117, 118, 119, 120] and Nested Sampling [121, 122] are often used which generate a set of samples whose distribution represents the true probability distribution.

MCMC is can be thought of as a selective random walk algorithm where the multiple *walkers* traverse the parameter space with various jump proposals. The walkers are programmed to traverse in such a way that they spend most of their iterations in regions of parameter space where the probability posterior is high, and conversely, spend the least amount of iterations where it is low. After a few burn-in iterations, typically the first 25%, the collection of parameter points traversed by the walkers are used as a sample whose probability distribution represents the true probability distribution $p(\vec{\theta}|\mathbf{d})$.

Nested sampling is also as Monte Carlo method, but one which maps the contour in n-dimensional parameter space to a 1-dimensional estimate such as the evidence. It then progressively reduces the size of the contour by converging on areas of higher evidence as shown in Figure 3.2.

Next, I discuss how we construct the signal waveform $\mathbf{h}(\vec{\theta})$.

3.4 Waveform models

In this section, I review the background and development of various waveform models that are used in signal and source inference. Compact binaries are promising laboratories for tests of strong-field GR. Their dynamics are obtained by solving the Einstein field equations, which are coupled non-linear second order differential equations of the space-time metric $g_{\mu\nu}$.

3.4.1 GR-based models

To a good approximation, the early inspiral phase of the gravitational waveform can be modeled analytically using post-Newtonian (PN) corrections to the Newtonian trajectory of the orbit, with PN expansion terms of increasing powers of the orbital velocity, v/c [29, 26], that are valid for small values of v/c where v is the velocity of the objects and c is the speed of light. As the orbit decays, the velocity becomes large enough that the approximation is no longer valid. The final cycles of the inspiral phase, as well as the merger and ringdown phases, require NR, which provides the computational infrastructure needed to solve the Einstein field equations without PN approximations [34, 35, 36]. As shown in van de Meent et al. [124], for systems with mass ratio ($q = m_2/m_1; m_1 > m_2$) smaller than 0.1, the perturbation theory can be used. Figure 3.3 shows the various regions of applicability of the PN, NR, and perturbation theory.

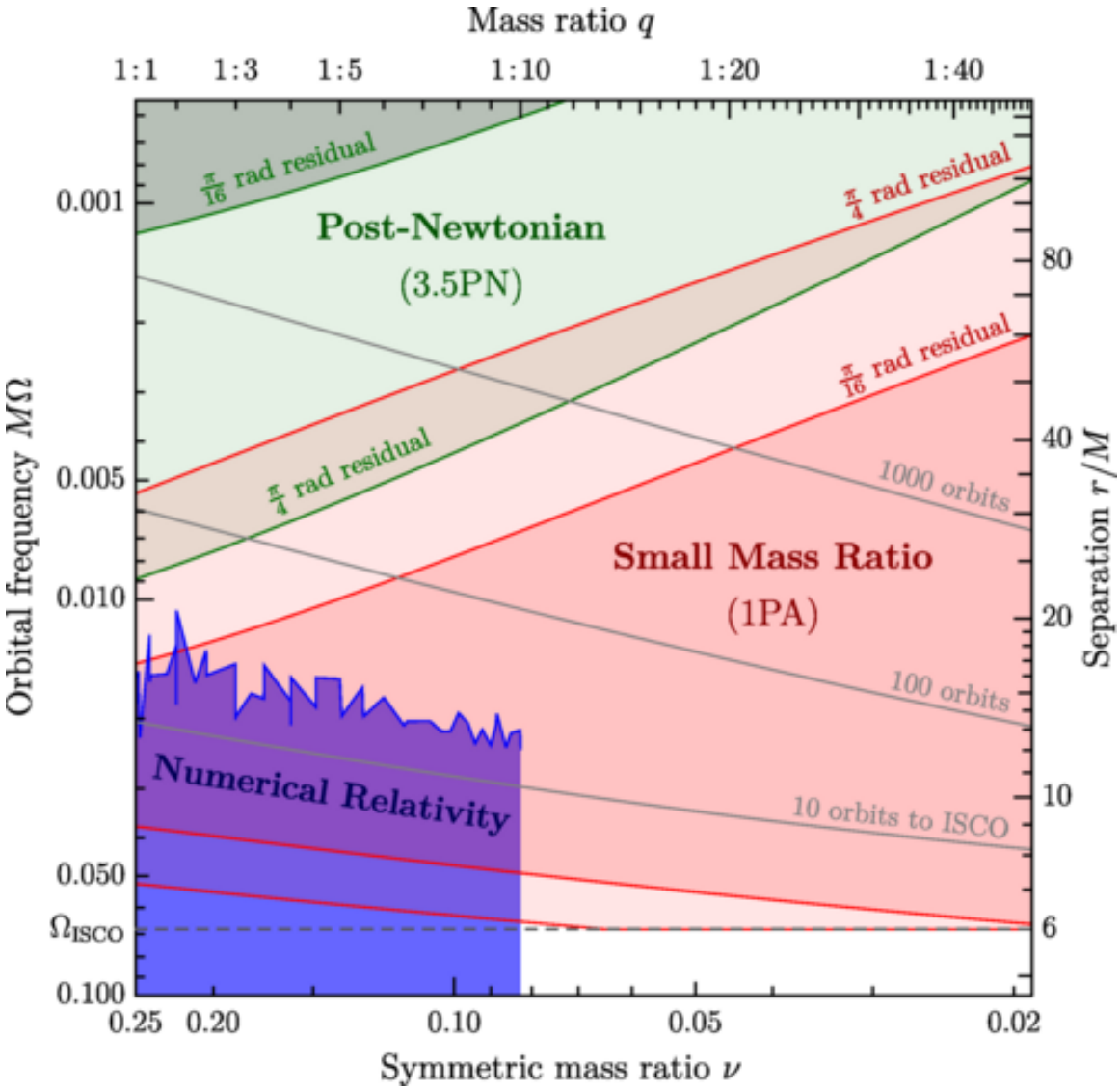

Figure 3.3: Regions of applicability of various GR-modeling methods for non-spinning black holes. Figure from [124].

CBC waveforms are described by 8 intrinsic parameters: the masses $m_{1,2}$ and the spins $\vec{S}_{1,2}$ (magnitude and direction) of the two compact objects. The two mass parameters are usually also inferred in the form of total mass $M_{Total} = m_1 + m_2$ which strongly dictates the ringdown, and chirp mass $\mathcal{M} = \frac{(m_1 m_2)^{3/5}}{M_{Total}^{1/5}}$, which strongly dictates the inspiral. The spin is typically described in terms of the dimensionless quantity, $a = c|S|/Gm^2$; a BH can have a maximum dimensionless spin of $a = 1.0$. Most NSs have spins that are lower than this value. For example, [125] places an upper limit of $a < 0.7$ for NSs with $M_{NS} > 1M_{\odot}$

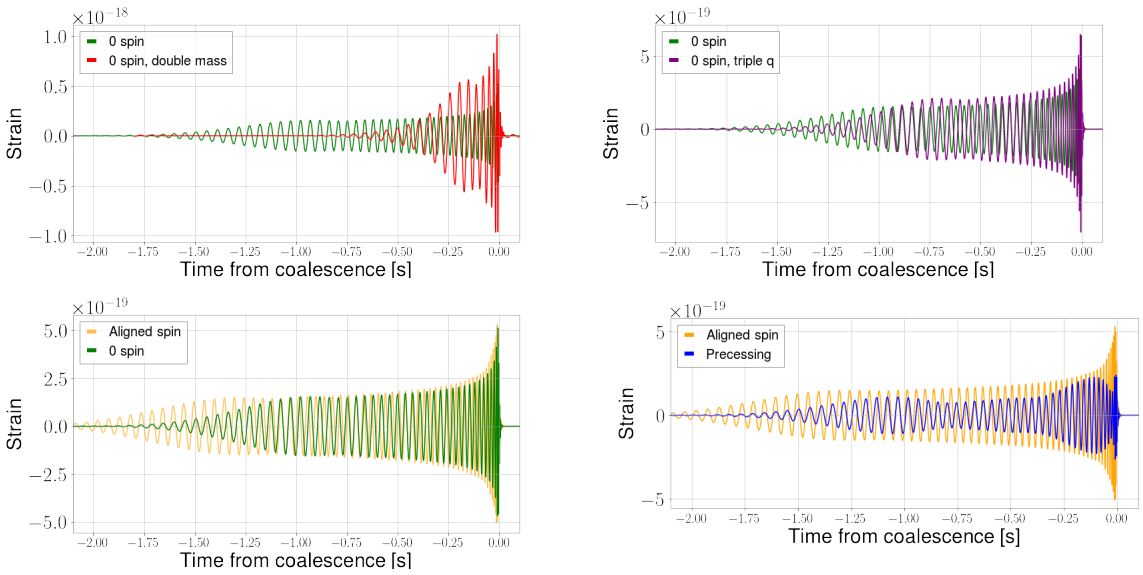

Figure 3.4: The effect of various parameters on the waveform. I show time-domain plots comparing the effect various parameters have on the signal waveform. I use an example system with component masses $(m_1, m_2) = (45M_\odot, 15M_\odot)$ spins set to 0 (green plots). The inclination, initial phase, and polarization angle are set to 0, and the luminosity distance (D_L =1 Mpc). All the waveforms are aligned such that their time of coalescence $t_c = 0$. In each of the four panels, I vary one aspect of the waveform parameters while keeping everything else the same. The top left plot shows the effect of doubling the total mass which causes the waveform frequencies to reduce but the duration of the waveform also reduces. The top right panel shows the effect of tripling the mass ratio which causes the signal amplitude to increase. The bottom left panel shows the effect of introducing a dimensionless spin of $a = 0.9$ in each BH along the z-direction of the orbital angular momentum which causes a longer waveform. The bottom right panel shows the effect of having the same spins in the planar direction, which causes the orbit to precess. This causes amplitude modulations in the waveform

for most realistic EOSs. Additional extrinsic parameters characterizing the CBC waveform are the luminosity distance D_L, right ascension and declination α, δ, the binary orientation with respect to the line of sight (inclination angle ι and polarization angle ψ), the time and phase of coalescence t_c, ϕ_c, and the eccentricity parameters (magnitude e and its argument of periapsis). Collectively, the intrinsic and extrinsic parameters make a 17 dimensional parameter space.

At the leading PN order, the GW inspiral phase evolution is described by the chirp mass, $\mathcal{M}$. At the next PN orders, the mass ratio $q = m_2/m_1, m_1 > m_2$, and the components of the

spin parallel to the orbital angular momentum $\vec{L}$ become significant. The mass M_f and spin a_f of the final black hole dictate the ringdown frequencies. Other parameters such as the inclination and polarization angles ι, ψ do not influence the morphology but cause minor changes in the amplitude and phase. The signal amplitude is inversely proportional to the luminosity distance D_L. Figure 3.4 shows the effect of varying some of these parameters with examples.

For analyses used in LIGO and Virgo, we use analytical models to efficiently sample this parameter space [126]. They can capture the complete dynamics of the inspiral merger and ringdown while being computationally inexpensive to obtain. NR simulations are by definition, discrete and represent singular points in the parameter space, and usually model the late inspiral, merger, and ringdown part of the waveform. Because of their high computational cost, we are also unable to obtain them "on the fly" as typical NR simulations can take weeks on multiple computing cores. Therefore, over the past couple of decades, there has been a large body of work done in formulating semi-analytical waveform approximations, also known as "approximants" [23, 127, 22, 128, 129, 130]. These approximants are formulated by combining the information of the inspiral from the PN corrections, and the merger-ringdown from NR simulations. Once formulated, they can be used to produce waveform templates fairly quickly. For example, a typical parameter estimation job using `LALInference`can have the order of 50000 sample points from the physical parameter space. Each of these points corresponds to a signal waveform of ~ 8000 floating point numbers which are used in an inner product computation with another set of ~ 8000 numbers corresponding to the detector data. This usually takes one or two days on a single-core computer.

There are three main families of such approximants. The first treats the inspiral part of the waveform (where the distance between the compact objects is large compared to their individual sizes) analytically using a perturbative Effective One Body (EOB) approach with a weak field PN approximation [30, 31, 32, 33, 100]. The latter part of the wave-

form is obtained using NR. The unknown higher-order analytical model coefficients are then calibrated using the NR results to obtain a semi-analytical formula for a given set of parameters. This formalism is thus known as `EOBNR` [23, 127, 22]. Variants of this include the non-precessing spins [23, 127, 131, 132], as well precessing spin cases [22].

The second models the inspiral, merger, and ringdown (IMR) parts of the waveform in the frequency domain using a phenomenological approach. The method breaks the waveform spectrum into sections that are piece-wise continuous in amplitude, phase, and their derivatives in the frequency domain [128, 129, 130] . The waveform is modelled as being a function of the PN approximants plus some free parameters, which are then fit using NR waveforms. This family of waveforms, known as `IMRPhenom`, also has non-precessing [128, 129, 130] as well as precessing cases [133].

The third uses surrogate models to interpolate between discrete parameter points. The waveforms at these discrete points are given by NR simulations. However, since NR waveforms only simulate the last few cycles, they are "hybridized" to include the early inspiral cycles. The early inspiral is given by an EOB model that is smoothly stitched with the NR waveform. These are known as `NRSurrogate` waveforms.

I discuss more details of approximant families in chapter 4.

3.4.2 Burst waveform models

Burst analyses model GWs as a superposition of a number of suitable basis functions parameterized by observable quantities such as amplitude and frequency [40, 41]. The inexact match of the basis functions with underlying GW signals results in generally lower intrinsic sensitivity than targeted CBC searches but the larger number of degrees of freedom allows for the recovery of un-modeled waveform phenomenology and, potentially, new physics. Burst methods are also used to search for GW signals from sources such as supernovae [134] and the post-merger phase of binary neutron star coalescence, where the physics is too uncertain to develop a sufficiently robust matched-filter template [106, 135,

46, 136].

3.4.3 Spherical harmonics and unmodeled deviations

In the GR formulation, GW strain can be expressed as a sum of spin weighed spherical harmonics ${}_{-2}Y_{l,m}$ [137]:

$$h(t,\theta,\phi) = \sum_{l,m} {}_{-2}Y_{l,m}(\theta,\phi)h_{l,m}(t) \tag{3.9}$$

where $h_{l,m}$ is the amplitude of the l,m mode and t is time. Here, $l = 0,1,2..$ and $m = -l,-(l-1)..0,l-1,l$. The angles θ,ϕ are quantities in the frame of reference of the source. There exists a direct mapping between these and the inclination and polarization angles ι,ψ defined in the detector frame of reference.

The $l = 0$ and $l = 1$ components have zero amplitudes since GR does not permit monopole and dipole radiation. The most dominant contribution for systems we are interested in is from the $l = 2, |m| = 2$ mode quadrupolar mode [138]. The $|m| = 0,1$ modes are significant for head-on collisions or highly eccentric inspirals [139]. For large swathes of parameter space (i.e., a majority of observer-source orientations, and mass and spin configurations) the most commonly detected signals are expected to be dominated by the $l = |m| = 2$ mode content. However, the effect of higher order modes becomes relevant in asymmetric mass ratios below 0.5 and large inclination angles.

Many of the low-latency searches (described in section 3.5) and initial parameter estimation studies, therefore, use approximants that are dominated by this mode. However, they present an incomplete picture of the information that can be inferred about the source. Inclusion of sub-dominant or higher order modes in helps resolve degeneracies such as the ones between mass ratios and spins, and, distance and inclination leading to better constraints on certain parameters as shown in [140]. Studies such as Bustillo et al [141] also show the effect of emission of higher order modes which are emitted asymmetrically

around a BBH orbit axis. The asymmetry causes a momentum reaction that imparts a *kick* [142] on the remnant BH, which gives rise to a secondary *chirp* detectable by LIGO and Virgo.

Recent works such as [143, 144, 145, 146, 147], introduce approximants which include higher order modes and allow for obtaining more precise estimates of the system parameters.

3.5 GW Searches

Low-latency searches are online algorithms that look for candidate GW signals in real-time i.e., within seconds to minutes from when the data is collected. They then report event candidates to a central database called graceDB [148]. Depending on the classification of the event, an alert is also sent out to various electromagnetic and neutrino observatories. There are two main types of searches: (i) GR-based searches which use template waveforms described above, such as `PyCBC`, `GsTLAL`, and multi-band template analysis (MBTA)(`MBTA`), and (ii) searches which use morphology-independent waveform models such as coherent WaveBurst (cWB) [40].

To assist in fast identification, searches maintain a pre-computed set of waveform signal models with which the data are matched. In the case of CBC searches, they maintain a *bank* of GR-based templates with which they, while burst searches typically use the discrete wavelet transforms.

3.5.1 GR-based searches

GR-based searches use a bank of waveform templates that provide a discrete sampling of the parameter space defined by the component masses (m_1, m_2) and the dimensionless spins ($\vec{\chi}_1$, $\vec{\chi}_2$. The banks cover total masses ($M_T = m_1 + m_2$) from $1M_\odot$ to 500 $M_\odot$ (`PyCBC`), 758 $M_\odot$ (`GstLAL`), and 200 $M_\odot$ (`MBTA`). Matching the templates with data generates a set of triggers and only the triggers SNRs are greater than a threshold are used

in further analysis. The thresholds are 4 for `PyCBC` and `GstLAL` and 4.5 or 4.8 for `MBTA` depending on the region of the parameter space.

The selected triggers then undergo an additional test of screening by comparing them with background estimates to assign them a false alarm rate (FAR) which defines how regularly we would expect to see a noise event with the same, or higher, ranking statistic as the candidate [149]. The approximants described above are used as templates in LIGO and Virgo searches based on the matched filter techniques [150, 10, 151, 152].

3.5.2 Burst searches

The cWB pipeline uses wavelets to project the data onto discretely sampled frequencies and times to construct a multi-resolution time-frequency tiling of the data segment under analysis. It calculates a *maximum likelihood ratio* statistic which represents the total SNR, and selects triggers that pass a certain threshold. It then calculates other network coherence quantities to decide if the trigger's origin is astrophysical or terrestrial. The cWB pipeline primarily targets BBH sources and is limited to the 15-512 Hz range. It operates in two configurations that target high-mass (central frequency f_c < 80 Hz) and low-mass (f_c > 80 Hz) BBH systems.

Following the detection of a GW candidate an offline parameter estimation (PE) analysis is performed on the data to calculate posterior probability distributions on the source parameters by algorithms which I describe below.

3.6 Offline parameter estimation

`LALInference` [153] is an offline follow-up analysis that models any non-Gaussianities in the detector data as template-based GW signals. It samples the probability distribution functions of the physical parameter space ($\vec{\theta}$) of binary systems. The sampling is done using MCMC or nested sampling.

As an example, Figure 3.5 shows the 50% and 90% 2D probability contours of the

component masses for GW150914 obtained using the `LALInference_nest` algorithm [79, 153]. These were obtained by marginalizing (Eq Equation 3.1) over all but the two parameters shown in the figure.

`LALInference` uses the same waveform families as described above to model the signal waveform. Most recently, two newer software packages have become the mainstream PE analysis tools: `Bilby` [154] and Rapid parameter inference on gravitational wave sources via Iterative FiTting (`RIFT`) [155]. Due to the large development overhead with the host software package of `LALInference`, `LALSuite` [156], the LIGO and Virgo collaborations have shifted to using these newer algorithms since O3b. The difference between them and `LALInference` is at the level of implementations of the sampler. The underlying template-based models remain the same.

3.7 `BayesWave`

`BayesWave` is the burst equivalent of `LALInference`[42, 157]. It models the non-Gaussianities in the detectors as a summation of a variable number of Morlet-Gabor wavelets parameters of the wavelets as well as the number of wavelets is sampled over.

To model an astrophysical signal, `BayesWave` assumes a *Signal* model in which the waveform $\mathbf{h}$ is coherent across the detectors. The waveform comprising of the wavelets is projected onto the network of detectors. Each wavelet, Ψ, is described by 5 parameters: the central time t_0, the central frequency f_0, the quality factor Q, the amplitude A, and the phase offset ϕ_0. The wavelet is given by

$$\begin{aligned} \Psi(t;\vec{\lambda}) &= A e^{(t-t_0)^2/\tau^2} \cos(2\pi f_0(t-t_0)+\phi_0) \\ \widetilde{\Psi}(f;\vec{\lambda}) &= \frac{\sqrt{\pi}A\tau}{2} e^{-\pi^2\tau^2(f-f_0)^2} e^{-i2\pi f t_0}\left(e^{i\phi_0} + e^{-i\phi_0} e^{-Q^2 f/f_0}\right)) \end{aligned} \tag{3.10}$$

where $\vec{\lambda} = (t_0, f_0, Q, A, \phi_0)$.

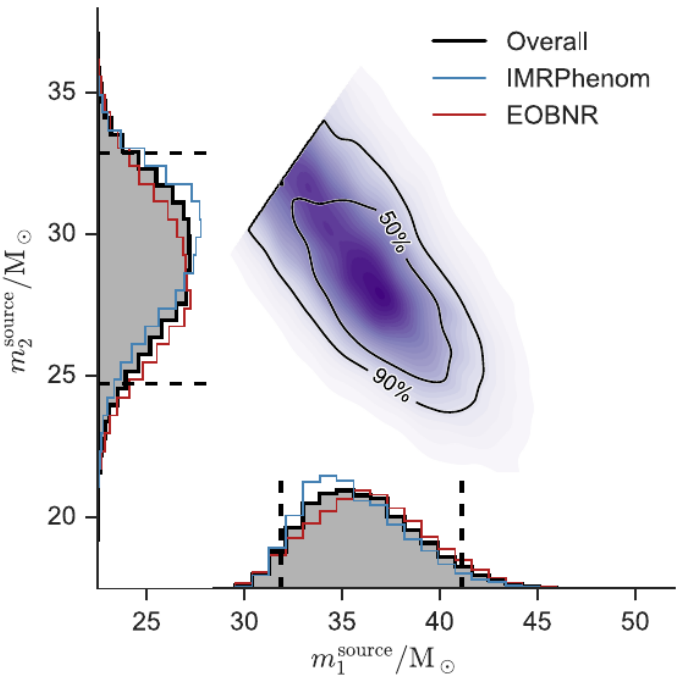

Figure 3.5: GW150914 mass posteriors. The figure shows the 2-D posterior probability distribution on the component masses as measured in the source frame obtained using `LALInference`. The grey pixels to regions with low probability while the blue pixels correspond to high probability. The grey histograms on each of the axes are the marginalized 1-D posteriors of the masses. The blue histograms correspond to the values obtained using the `IMRPhenom` approximant while the red histograms correspond to the `EOBNR` approximant. From [79]

.

A generalization of the wavelet model is the chirplet model which includes a time-dependent frequency component $\dot{f}_0$ as [158]

$$\begin{aligned}
\Psi(t;\vec{\lambda}) &= Ae^{(t-t_0)^2/\tau^2}\cos\left(2\pi f_0(t-t_0)+\pi\dot{f}_0(t-t_0)^2+\phi_0\right) \\
\widetilde{\Psi}(f;\vec{\lambda}) &= \frac{\sqrt{\pi}A\tau}{2(1+\pi^2\beta^2)^(1/4)}e^{\frac{-\pi^2\tau^2(f-f_0)^2}{1+\pi^2\beta^2}}e^{-i2\pi ft_0}\left(e^{i(\frac{\phi_0+\delta-\pi^3\beta\tau^2(f-f_0)^2}{1+\pi^2\beta^2})}\right. \\
&\quad \left. + e^{-i(\frac{\phi_0+\delta-\pi^3\beta\tau^2(f-f_0)^2}{1+\pi^2\beta^2})}e^{-Q^2f/f_0}\right)
\end{aligned} \tag{3.11}$$

where $\vec{\lambda}(t_0, f_0, \dot{f}_0, Q, A, \phi_0)$, $\tau = Q/2\pi f_0$, $\delta = \frac{1}{2}\arctan\pi\dot{f}_0\tau^2$, and $\beta = \dot{f}_0\tau^2$ is a dimensionless parameter which is called the chirplet parameter.

Figure 3.6 shows the time-domain plots of a wavelet and a chirplet with the same parameters except for $\beta = 0.8$ which causes an increase in the frequency in the chirplet case. Figure 3.7 shows a time-frequency plot of chirplets with various values of central time, frequency, quality factor, and chirplet parameter. Past studies such as [48] have shown that the wavelet and chirplet models have similar levels of agreement with template-based waveforms for the observed BBH systems.

In the standard `BayesWave` implementation we assume an elliptically polarized GW signal. The plus component (h_+) of the strain is given by

$$\widetilde{h}_+ = \sum_{j=0}^{N} \Psi_j \tag{3.12}$$

, where N is the number of wavelets that describe the signal model. The cross-component ($h_\times$) is given by

$$\widetilde{h}_\times = ie\widetilde{h}_+ \tag{3.13}$$

, where e is the ellipticity parameter which is also sampled over. `BayesWave` was initially developed using the elliptical polarization assumption since the early era of GW astronomy had only two nearly-aligned LIGO detectors which resulted in poor polarization sensitivity. Recent works such as [140] show that higher order modes are measurable with the current detector network sensitivities and it is important to relax the ellipticity constraint, where the parameters of $\widetilde{h}_+$ and $\widetilde{h}_\times$ are independently sampled. This has recently been implemented and discussed in [159] which introduces generic polarizations in the `BayesWave` signal model. The two polarizations in that model are given using

$$\begin{aligned} h_+ &= \sum_{j=0}^{N} \Psi(t_0, f_0, Q, A_+, \phi_{0,+}) \\ h_\times &= \sum_{j=0}^{N} \Psi(t_0, f_0, Q, A_\times, \phi_{0,\times}). \end{aligned} \tag{3.14}$$

The ellipticity parameter is absent, and the wavelets share the central time, frequency, qual-

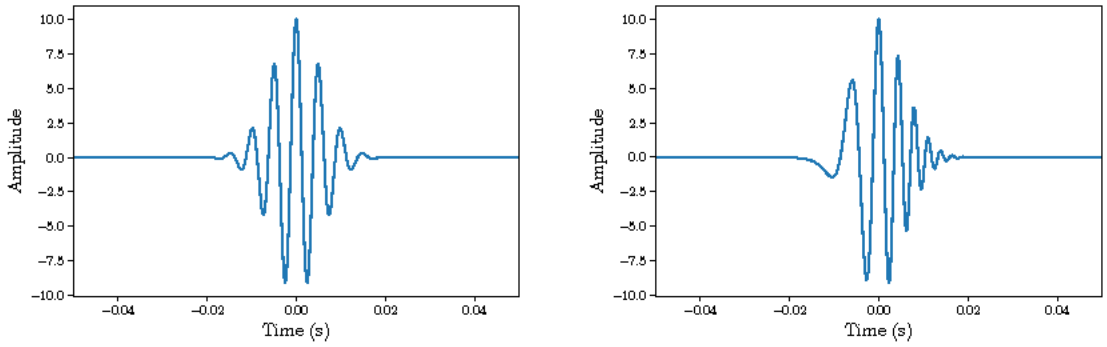

Figure 3.6: Example `BayesWave` wavelet (left) and chirplet (right) time domain plots. For both examples $f_0 = 200$, $t_0 = 0$, and $Q = 10$. In the chirplet example $\beta = 0.8$. Figure from [158].

ity factor parameters but the amplitude and phase parameters are independent.

The majority of my work in this thesis is limited to the use of the wavelet model with the elliptically polarized GW strain.

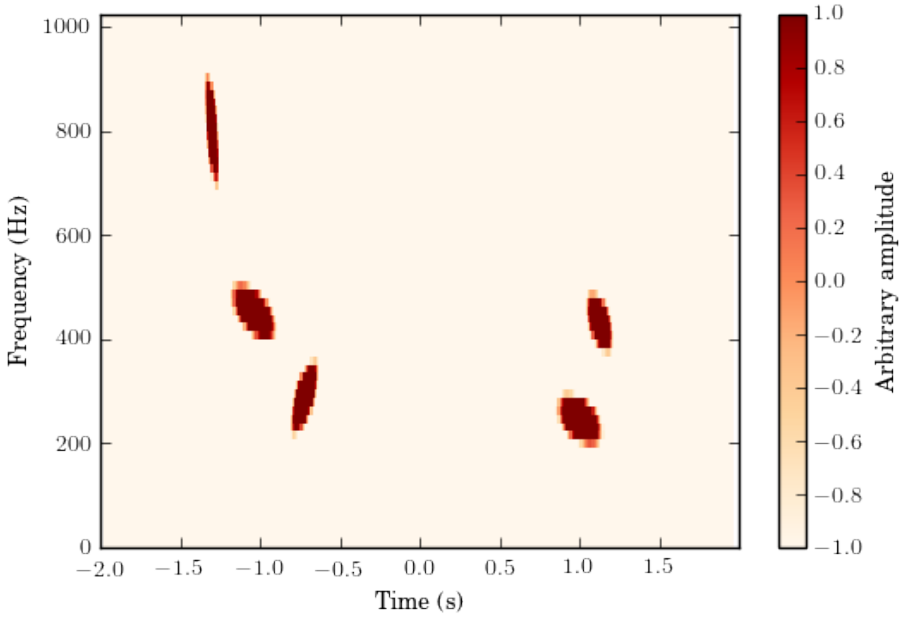

Figure 3.7: Spectrograms of `BayesWave` wavelets and chirplets with t_0, f_0, Q, and β. Figure from [158].

LIGO and Virgo detectors are also plagued by noise glitches which are generally not causally related between detectors [11]. `BayesWave` fits the data with a *Glitch* model,

which, similar to the signal model, uses Morlet Gabor wavelets, with the difference that the waveforms are not coherent across detectors. The wavelets that are fit to any non-Gaussianities are independent of each other. Hence, each detector has a glitch reconstruction that is independent of the other detectors.

In addition to the wavelet (and chirplet) model to reconstruct the signal or glitch waveform, `BayesWave` also parameterizes the PSD given using the `BayesLine` [157] algorithm which is a fully integrated part of `BayesWave`. `BayesLine` models the PSD with two components: a cubic spline to fit the broad band noise, and a sum of Lorentzians to fit the narrow band spectral lines (see Figure 3.8). The number and location of Lorentzians and cubic spline control points are also sampled over. This is in contrast with traditional methods of estimation the PSD, such as the Welch's method, which use averaging techniques applied to a large number of noise realizations in times surrounding the analysis segment. The `BayesLine` PSD estimate is completely determined by the data segment under analysis, which is more robust to slowly varying non-stationary noise compared to the Welch's method. Details of the `BayesLine` algorithm can be found in [157], and an in-depth study describing its merits over using the Welch's method can be found in [160].

`BayesWave` uses reversible-jump Markov chain Monte Carlo (RJMCMC) [161] to sample over a variable dimensional parameter space as wavelets can be added to removed from a model based on the improvements to the fit. This flexibility allows for robust fits to the waveform. The signal model will reconstruct any feature in the data that is coherent across the detector network if the feature is loud enough compared to the background noise. This makes the wavelet model flexible enough to fit a wide range of signal morphologies. For the case of BBH signals, it is most sensitive to times close to the merger where the amplitude peaks.

To discourage run-away inclusion of wavelets, however, the places a prior peaked at 5 on the number of wavelets and a penalty for the inclusion of wavelets beyond that. It has a hard limit of 100 by default. Similarly, it places a limit on the quality factor (Q) to a

maximum of 40. Q is proportional to the number of cycles in a wavelet ($Q = 2\pi f_0 \tau$), and a limit on Q is desirable since CBC waveforms increase in frequency over a few cycles. Multiple wavelets with different central frequencies fit are better than a single long wavelet at fitting a signal whose frequency changes through time.

`BayesWave` relies on estimating the Bayesian posterior probability distribution of the model waveform $\mathbf{h}$ describing the data $\mathbf{d}$ assuming model M. Using the ratio of the evidences, it computes the relative probabilities that the data are described by any of the competing Signal, Glitch, and Noise models. In the standard implementation of `BayesWave`, the Signal and Glitch models are run independently, or sequentially, and the data are modeled as summation of Noise + Signal or Noise + Glitch. However, it is useful to model the data as a superposition of these two models in cases where the data have noise glitches present near astrophysical signals. We call this the `Signal+Glitch`model and it is discussed in chapter 6.

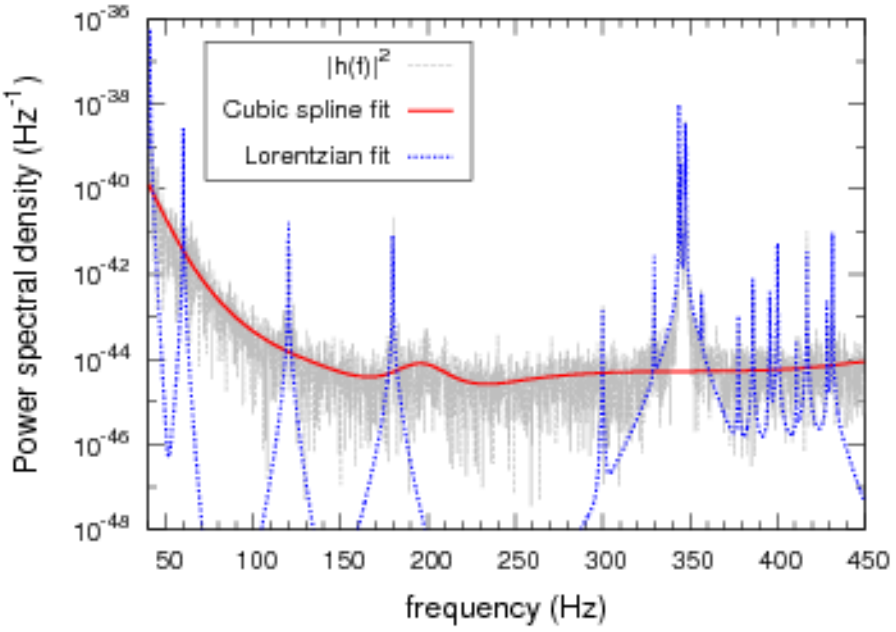

Figure 3.8: Modeling detector noise with `BayesLine`. The plot shows the cubic spline model (red solid line) which models the smoothly varying PSD, Lorentzians (solid dashed line) which model the spectral lines due to hardware resonances, and the detector data power spectrum (gray). Figure from [157].

3.8 `BayesWave` use cases

Signal consistency and reconstructions studies

The signal inferred by the template-based models relies on several assumptions, such as the correctness of GR, the precision of NR simulations, approximations used in calculating the coefficients of semi-analytical approximants, etc. `BayesWave` lends is a useful tool for inferring the signal waveform that is model-independent. Signal consistency tests compare the waveform computed by `BayesWave` and template-based models and help an additional level to validity to the waveform.

The test can also be used for investigating the presence of higher order modes in the data. For example, GW170729 was the heaviest BBH that LIGO and Virgo had observed in O1 and O2. It also had an unequal mass ratio which pointed toward possible higher order mode content. I performed investigations to characterize the higher order mode content by comparing results using various approximants with and without higher order modes. In [48], I compared the reconstructed template-based waveforms with `BayesWave` reconstructions. We did not find any significant evidence for higher order modes, however, we outlined the procedure that could be used for future events which show signs of higher order modes. I used this procedure on GW190412 which was the first GW event with a confirmed observation of higher order modes [140]. In [140], I compared the various GR based approximants with `BayesWave` reconstructions. The GR approximants were in increasing level of complexity: from $(l, |m|) = (2, 2)$ spin aligned to higher order mode spin aligned to higher order mode with spin precession. We found that the agreement is highest for the GR approximants that include higher order modes with spin precession. This gave credence to the claim of the discovery of higher order modes in this event.

Apart from this, the consistency test can be used to detect deviations in the model. The deviations could be in the strong field regime of GR such as in the generation of GWs. Examples include deviation in the (PN) coefficients and Lorentz invariance violation [162,

163, 164].

Tests of GR and residuals analysis

The simplest test of GR is to subtract the best-fit template waveform model from the data and check the consistency of the residual with detector noise. This is known as the residuals test and we use it for testing GR models.

Since `BayesWave` is adept at characterizing coherent non-Gaussianities, I use it in the residuals test to check for any residual signal power that is not accounted for by the template-based waveform model.

A population analysis then helps us place limits on GR. I cover this topic in further detail in chapter 5

Cleaning detector data

As described in chapter 2, glitches are transient noise events with known or unknown causes. When they coincide with GW detections, they threaten to affect the quality of source inference. In cases where the cause of a glitch is unknown, it cannot be subtracted from the data. We use `BayesWave` to model the signal and glitch parts of the data so that the glitch can effectively be "cleaned" from the data and the latter is then used for inference analysis.

This procedure has been in past GW detections [165] but it has never been characterized. In chapter 6, I describe this method in detail and discuss the results of characterization.

Inferring BNS post-merger signals

The post-merger signal from a BNS merger is a short-duration (less 0.1 seconds) burst signal with a primary peak in its frequency spectrum. This makes it an ideal candidate for detection with `BayesWave`.

I have used `BayesWave` to search for post-merger GW signals in the GW190425 event. I have also done a study that reports on the detectability of a post-merger signal by `BayesWave` as a function of the loudness. The simulated GW signal we use is from a particular EOS. I cover this in detail in chapter 7.

3.9 Commonly used data products

In GW data analysis, we describe and interpret our results via a set of data products that make inference easy. For the sake of convenience, I list and explain some of the commonly used ones below using plots from the `BayesWave` run on the BBH GW event GW200129 from the third GW transient catalog (GWTC-3).

Power spectral density and amplitude spectral density: LIGO and Virgo's noise is colored Gaussian noise, i.e., the noise amplitude varies as a function of frequency. The usual method of characterizing this is through the power spectral density (PSD) as shown in Equation 2.20. When discretized, this quantity represents the variance of the Gaussian noise in a given frequency bin. The square root of the PSD is the amplitude spectral density (ASD). Plots of the PSD and the ASD are shown using the log-log scale since the values of the curves as well as the frequencies vary across several orders of magnitude as shown in Figure 3.9.

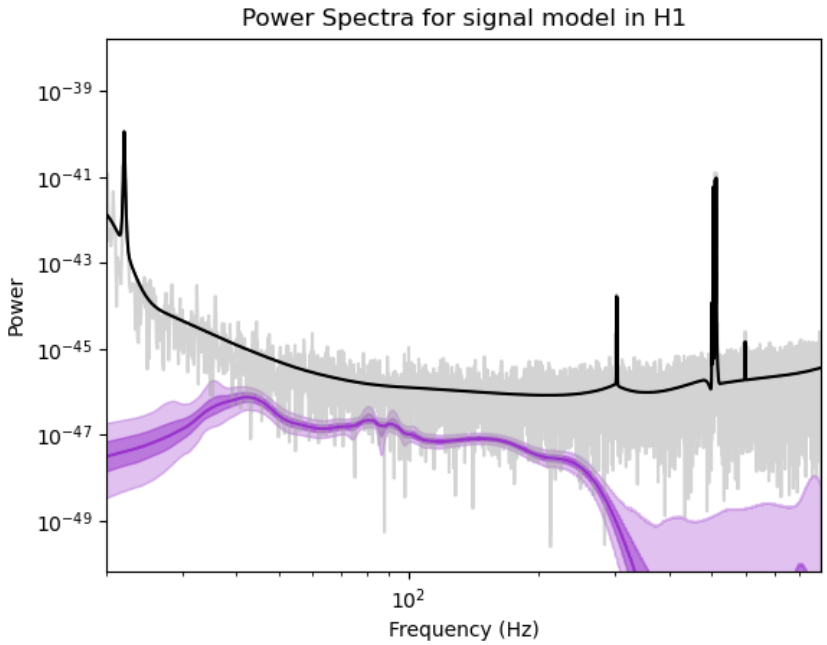

Figure 3.9: The power spectral density observed in LIGO Hanford during GW200129. Plot shows the detector data (gray), median PSD computed by `BayesLine` (black), and the power spectrum of the reconstructed median `BayesWave` GW waveform for GW200129 (solid orchid line) and the 50% and 90% credible intervals (shaded orchid lines). The x-axis is the frequency in Hz and the y-axis is the power spectrum in Hz^{-1}

Whitened data: Since LIGO and Virgo have varying sensitivities, the inner product (Equation 3.6) used in likelihood calculations is weighed in favor of sensitivities where the detector is more sensitive by dividing PSD:

$$\langle a|b\rangle \equiv 4\,\mathrm{Re}\int_0^\infty \frac{\widetilde{a}(f)\widetilde{b}^*(f)}{S_n(f)}df, \tag{3.15}$$

We absorb the PSD in the integrand into the strain terms on the right hand side:

$$\langle a|b\rangle \equiv 4\,\mathrm{Re}\int_0^\infty \widetilde{a}_w(f)\widetilde{b}_w^*(f)df, \tag{3.16}$$

where

$$\widetilde{a}_w(f) = \frac{\widetilde{a}(f)}{\sqrt{S_n(f)}}, \tag{3.17}$$

is the *whitened strain*. We convert this into the time domain using the inverse Fourier transform

$$a_w(t) = \int_{\infty}^{\infty} e^{-i2\pi ft} \widetilde{a}_w(t) df. \tag{3.18}$$

to get the whitened strain in the time domain (see Figure 3.10). Its amplitude is in units of the loudness of the noise. I use the whitened waveform in the majority of the plots where I show the time-domain quantities.

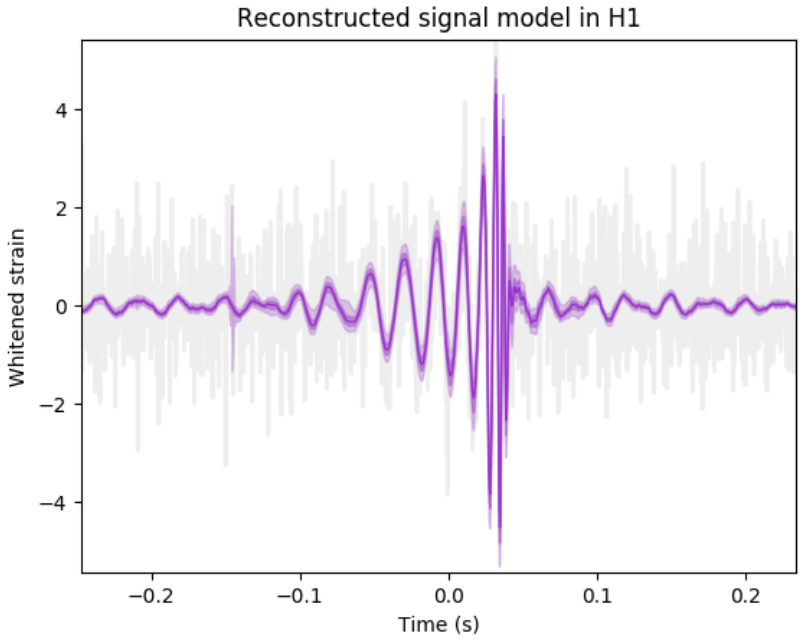

Figure 3.10: Whitened signal of GW200129. The plot shows the whitened data in the LIGO Hanford detector (gray), and median whitened `BayesWave` GW waveform of GW200129 (solid orchid line) and the 50% and 90% credible intervals (shaded orchid lines). The x-axis is the time in seconds from the merger and the y-axis is the whitened amplitude in units of the standard deviation of the noise $\sigma_{\rm noise}$ The signal and data plotted here are obtained respectively dividing the signal and data by the square root of the PSD show in Figure 3.9 and taking the inverse Fourier Transform.

Spectrogram: Spectrograms are used to visualize the frequency evolution of a signal through time. It is made up of a series of short Fourier transforms. SFTs are constructed by chopping the whitened time series into several smaller, usually overlapping chunks, and taking their Fourier transform. This gives a 2-D representation of the signal which is plot-

ted as a heatmap (see Figure 3.11). The quieter pixels point to nominal Gaussian while the brighter pixels point to an excitation above the Gaussian noise.

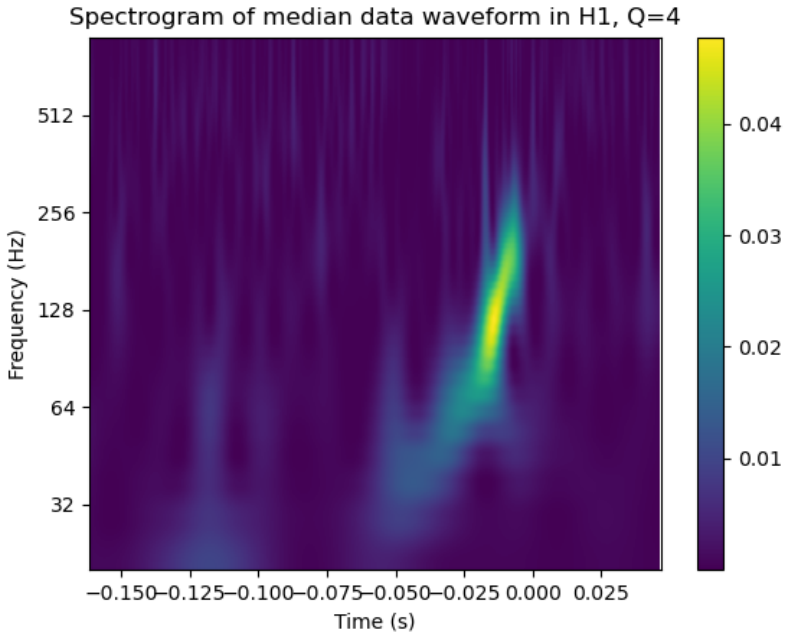

Figure 3.11: Spectrogram of GW200129. The plot shows the spectrogram of the data from the `BayesWave` run on GW200129. The x-axis shows the time in seconds from the coalescence time, the y-axis shows the frequency in Hz. The chirp is seen as the bright series of pixels increase in frequency as time progresses.

Corner plots: Corner plots are a useful way to view multi-dimensional probability distributions using pairs of parameters at a time. A corner plot has multiple panels arranged in a 2-D matrix where rows and columns represent parameters as shown in Figure 3.12 which shows the distribution of the wavelet parameters discussed in section 3.7 for the signal model. Each row and column pair has one panel which shows the 2-D histogram of the points. When the row and column parameters are the same, the panel shows the 1-D histogram plot.

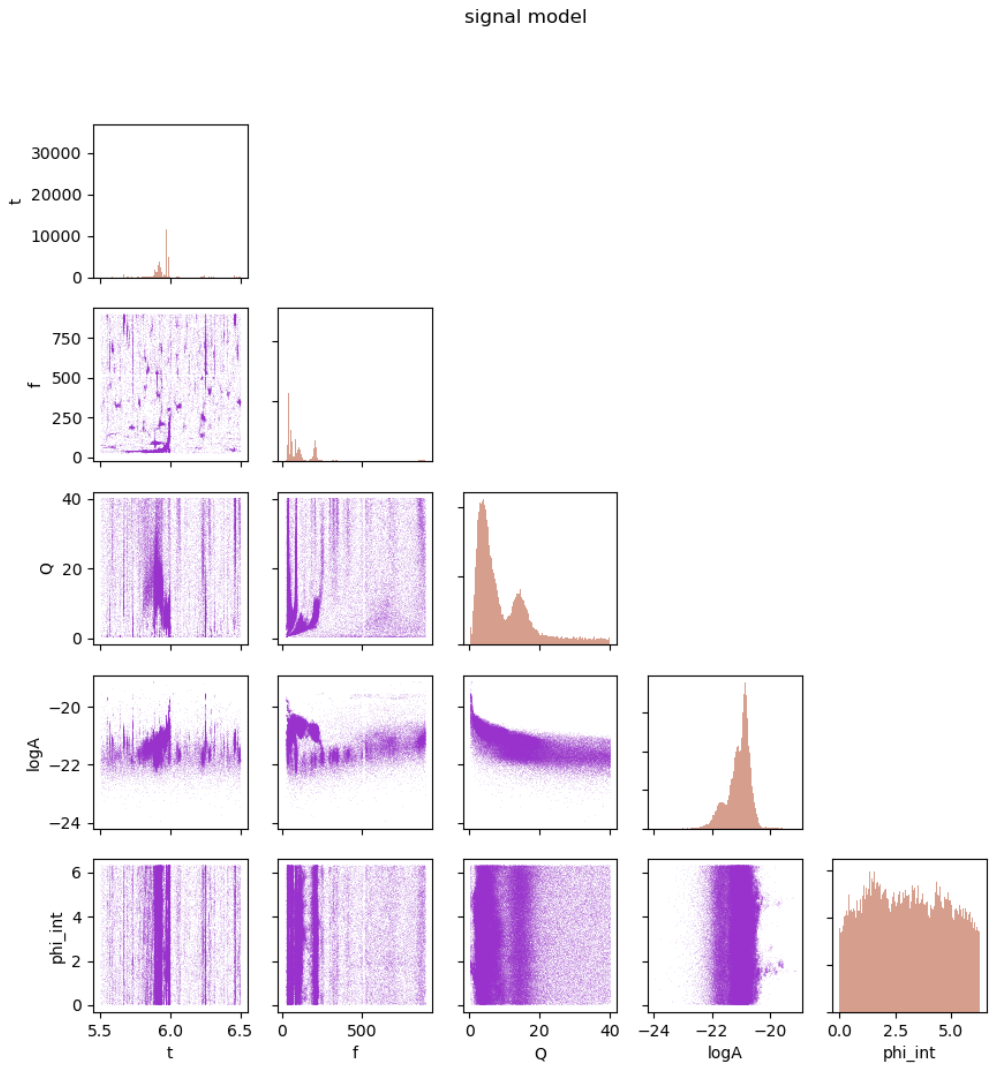

Figure 3.12: Corner plot of the `BayesWave` signal wavelets for GW200129. The plot shows the 2-D histograms (orchid) of the central time (t_0, t in figure), central frequency (f_0, f in figure), Quality factor (Q), log amplitude (logA) and the phase (ϕ_0, phi_int in figure). The diagonal panels (pony) show the 1-D histograms.

CHAPTER 4

WAVEFORM RECONSTRUCTIONS AND CONSISTENCY TESTS

In this chapter, I discuss inferences made with `BayesWave` model-independent waveform reconstructions. `BayesWave` models the signal in the detectors as a summation of coherent Morlet-Gabor wavelets whose number and parameters are sampled by a trans-dimensional reversible-jump Markov chain Monte Carlo (RJMCMC) sampler. The resulting signal is an independent estimate of the true waveform; calculating its agreement with GR template-based reconstruction is an important step in the event validation. The agreement depends on several factors such as the signal-to-noise ratio (SNR), the total mass of the binary (M_T), type of approximant used, etc.

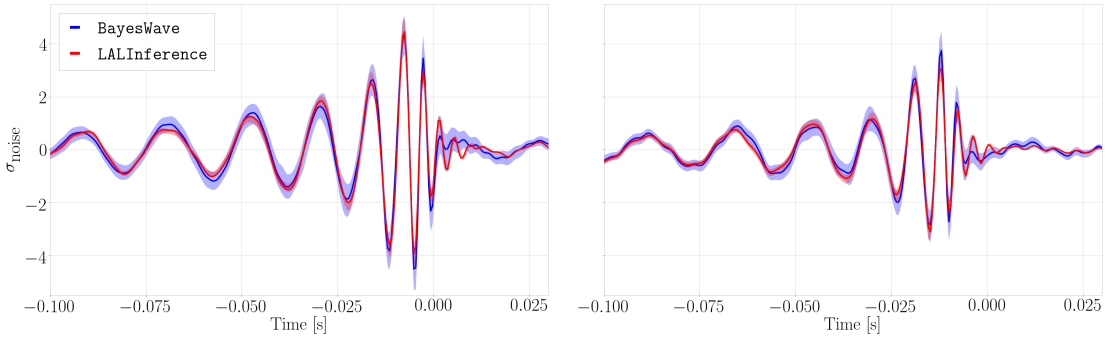

Figure 4.1: `LALInference IMRPhenomPv2` (red) [166] and `BayesWave` (blue) reconstructions of GW150914 [167] using data from GWTC-1 [168]. The left and right panels respectively show the waveform in LIGO Hanford and LIGO Livingston. The x-axis represents the time in seconds before the coalescence. The y axis represents the strain amplitude whitened using a filter which is the inverse amplitude spectral density (ASD). The units are in multiples of the standard deviation of the noise. Figure from [43].

4.1 Waveform families

The agreement between `BayesWave` and the template-based waveform depends on the approximant used. The three main approximant families used by the LIGO and Virgo Col-

laborations for PE are the (i) Inspiral Merger Ringdown Phenomenological (`IMRPhenom`) waveform family, the (ii) Effective One Body Numerical Relativity (`SEOBNR`) waveform family, and the (iii) NR surrogate waveform family. All three of these combine aspects of analytical relativity and NR and offer waveforms that cover the inspiral, ringdown, and merger phases of waveforms.

The IMRPhenom family uses post-Newtonian approximations [29] to compute the inspiral, and uses a phenomenological approach to capture the merger by calibrating with effective one body NR (EOBNR) hybrid waveforms [38, 21, 166]. Examples include waveforms that are spin aligned: `IMRPhenomD` [38, 21] and `IMRPhenomHM` [143], of which the latter includes higher order modes, effective spin precessing: `IMRPhenomPv2` [166], `IMRPhenomPv3`, `IMRPhenomPv3HM` and the most recently commonly used waveform approximant is `IMRPhenomXPHM` which includes full spin-precession and higher order modes. Table 4.1 summarizes some of the important waveform approximants used in PE.

The EOBNR waveform family uses resummation of post-Newtonian approximations to compute the inspiral and calibrates NR simulations for late-inspiral and merger. Examples of this family are waveforms that are spin aligned: `SEOBNRv4` [24] and `SEOBNRv4HM` [144] of which the latter includes higher order modes, fully spin precessing: `SEOBNRv3` [23, 22], `SEOBNRv4P`, and the most recently used `SEOBNRv4PHM` which includes full precession and higher order modes. Both families use BH perturbation theory to describe the ringdown of the final BH [169, 170].

The NR Surrogate family uses *surrogate* models i.e., interpolants built from NR simulations to generate waveforms at arbitrary values of the parameters. Because NR simulations include spherical harmonic modes till $\ell = 4$, the NR Surrogate family includes all higher order modes till $\ell = 4$.

Table 4.1: Approximants used in GW inference analysis. Note that that the ROM in SEOBNRv4_ROM SEOBNRv4HM_ROM stands for *reduced-order model* which makes the waveform generation much faster by delivering the same likelihood computations but with fewer terms.

Family	Waveform Model	Spin Dynamics	Modes $(\ell, \lvert m\rvert)$
Phenom	IMRPhenomD [38, 21]	Aligned	(2,2)
	IMRPhenomPv2 [166]	Effective spin precession	(2,2)
	IMRPhenomHM [143]	Aligned	(2, 2), (3, 3), (4, 4), (2, 1), (3, 2), (4, 3)
	IMRPhenomPv3 [171]	Double spin rotation precession	(2,2)
	IMRPhenomPv3HM [172]	Double spin rotation precession	(2, 2), (2, 1), (3, 3), (3, 2), (4, 4), (4, 3)
	IMRPhenomXHM [173]	Improved spin-aligned	(2, 2), (2, 1), (3, 3), (3, 2), (4, 4)
	IMRPhenomXPHM [174]	Full spin-precession	(2, 2), (2, 1), (3, 3), (3, 2), (4, 4)
EOBNR	SEOBNRv3 [23, 22]	Effective spin precessing	(2,2), (2,1)
	SEOBNRv4 [24]	Aligned	(2,2)
	SEOBNRv4HM [175]	Aligned	(2, 2), (2, 1), (3, 3), (4, 4), (5, 5)
	SEOBNRv4_ROM [24]	Aligned	(2,2)
	SEOBNRv4HM_ROM [175]	Aligned	(2, 2), (2, 1),(3, 3),(4, 4),(5, 5)
	SEOBNRv4P [176]	Precessing	(2,2)
	SEOBNRv4PHM [176]	Precessing	(2, 2), (2, 1), (3, 3), (3, 2), (4, 4), (4, 3)
NRSurrogate	NRSur7dq4 [177]	All the dynamics from NR	All available modes
	NRHybSur3dq8 [178]	All dynamics from NR and hybridization	All available modes

4.2 Quantifying agreement between waveforms (overlap)

To quantify the agreement between `BayesWave` and the template-based waveform, we use point estimates of the signal waveform from each. Here, we use `LALInference` to sample parameter space of the templates and we use the posterior sample for which the likelihood function described in Equation 3.2 is maximum, which we will call the maximum likelihood waveform ($\mathbf{h}_{\rm LI}$). I should caution that this is a good approximation of, but not necessarily, the true maximum, as `LALInference` is a posterior distribution inferring algorithm, rather than a peak finding algorithm. For `BayesWave` we use the estimate obtained by taking the median of the waveform value at every time index from the whole set of samples. We call this the median `BayesWave` waveform ($\mathbf{h}_{\rm BW}$). We do not use the maximum likelihood `BayesWave` waveform since, unlike template-based waveforms, the wavelets are "nuisance parameters" that do not have any physical meaning themselves. Instead, it is the fit waveform that is fundamentally of interest. $\mathbf{h}_{\rm BW}$ is a collective estimate across samples that is stable because it is relatively immune to the stochastic fluctuations of the variable dimensional sampler. More discussions about these choices can be found in [43, 48].

We quantify the agreement between the waveform reconstructions via the *overlap* [179]:

$$\mathcal{O}_{\rm B,L} \equiv \frac{\langle \mathbf{h}_{\rm LI} | \mathbf{h}_{\rm BW} \rangle}{\sqrt{\langle \mathbf{h}_{\rm LI} | \mathbf{h}_{\rm LI} \rangle \langle \mathbf{h}_{\rm BW} | \mathbf{h}_{\rm BW} \rangle}}, \tag{4.1}$$

where the quantity $\langle \mathbf{h}_{\rm LI} | \mathbf{h}_{\rm BW} \rangle$ follows the definition from Equation 3.6

The overlap is a generalization of the cosine of the angle between two vectors, where $\mathbf{h}_{\rm BW}$ and $\mathbf{h}_{\rm LI}$ are the two vectors in an m dimensional complex vector space, where m is the number of frequency components. The overlap value ranges between -1 (complete disagreement) to 0 (no agreement) to 1 (complete agreement).

4.3 Variation of the overlap with SNR and M_T

To study the variation of the overlap $\langle \mathbf{h}_{\rm LI} | \mathbf{h}_{\rm BW} \rangle$ as a function of the system properties, I run `LALInference` and `BayesWave` on simulated GW signals added to noise from the LIGO and Virgo detectors, also called "injections", to give simulated observation data streams $\mathbf{d}$. For this study, I used the `IMRPhenomPv2` approximant to perform injections and use a reduced-order quadrature (ROQ) [180] of `IMRPhenomPv2` to compute the likelihood while analyzing with `LALInference`. The ROQ reduces the computational cost of parameter estimation by reducing redundant computations. I did not use the EOB approximants for recovery as they are computationally more expensive, and NR Surrogate models did not exist at the time of this study.

The `BayesLine` algorithm which computes the median PSD, $S_n(f)$, that is used in the likelihood computations described in Equation 3.2 and in the overlap calculation in Equation 4.1. $S_n(f)$ and $\mathbf{d}$ are then fed into `LALInference` and `BayesWave` for analysis. This is the procedure used in LIGO and Virgo data offline PE follow up analyses on actual GW event detections. We compute the overlap between $\mathbf{h}_{\rm LI}$ and $\mathbf{h}_{\rm BW}$ using Eq. Equation 4.1.

The agreement between burst and template-based waveforms is most sensitive to the total mass M_T of the GW source and the SNR of the GW signal [181]. To systematically study the overlap as a function of these quantities, I analyzed injections of a population of `IMRPhenomPv2` waveforms using `LALInference` and `BayesWave`. These help us establish typical trends in the overlap over a broad range of systems. I injected into noise from the second observing run of the LIGO detectors [182]. I divided the population injections into four different subsets based on their total mass M_T:

1. $10\,M_\odot < M_T < 30\,M_\odot$
2. $30\,M_\odot < M_T < 60\,M_\odot$
3. $60\,M_\odot < M_T < 90\,M_\odot$

4. $90\,M_\odot < M_T < 120\,M_\odot$.

The mass ratios, spins, orientations, and sky locations are distributed uniformly. For each of the mass ranges, I create five population sets of SNRs: 10, 20, 30, 60, 90. To strike a balance between computational cost and the number of sample points, I perform 50 injections per SNR range per mass range, for a total of 1000 injections.

For each M_T range and SNR pair, I computed overlaps between $\mathbf{h}_{\rm BW}$ and the injected GR signal, $\mathbf{h}_{\rm INJ}$ ($\mathcal{O}_{\rm B,I}$), and the overlap between the $\mathbf{h}_{\rm LI}$ and $\mathbf{h}_{\rm INJ}$ ($\mathcal{O}_{\rm L,I}$). The subscripts "B", "L", and "I" respectively represent `BayesWave`, `LALInference`, and the injection. As reconstruction performance improves, the overlaps is closer to 1. For ease of visualization, I define $\Delta = 1 - \mathcal{O}$, where $\mathcal{O}$ is the overlap, and we use the same subscripts as for the overlap. Δ quantifies the disagreement between two waveforms. For each M_T range, I obtain Δ distributions. I then plot the medians and 90% confidence intervals of these distributions as a function of the SNR in Fig. Figure 4.2.

We see that at low SNRs, $\Delta_{\rm B,I}$ is high as `BayesWave` is unable to recover the full signal. This is even more pronounced in systems with lower M_T since the signal waveform is longer and the SNR is spread over a longer duration. We also see that at a particular SNR, $\Delta_{\rm B,I}$ decreases with increasing M_T, since the signal waveform gets increasingly shorter and is more compactly represented with the wavelet model. $\Delta_{\rm B,I}$ falls steadily as the SNR increases. On the other hand, $\Delta_{\rm L,I}$ is less than 0.2, even for low SNRs, as `LALInference` can reconstruct the GR signal morphology better than `BayesWave` at lower SNR. This is expected since `LALInference` is using templates that predict the signal over the entire observing band. `BayesWave` however, can only reconstruct high amplitude features in the data. $\Delta_{\rm B,I}$ becomes smaller as M_T and SNR increase, and `BayesWave` is able to reconstruct more and more parts of the signal. Past studies [4, 183] have shown that we expect $\Delta_{\rm B,I}$ and $\Delta_{\rm L,I}$ to vary as $\propto 1/\mathrm{SNR}^2$ [184]. I plot this curve and up to a constant scaling factor, we see that the slopes of the reconstructions follow this relationship to a large extent.

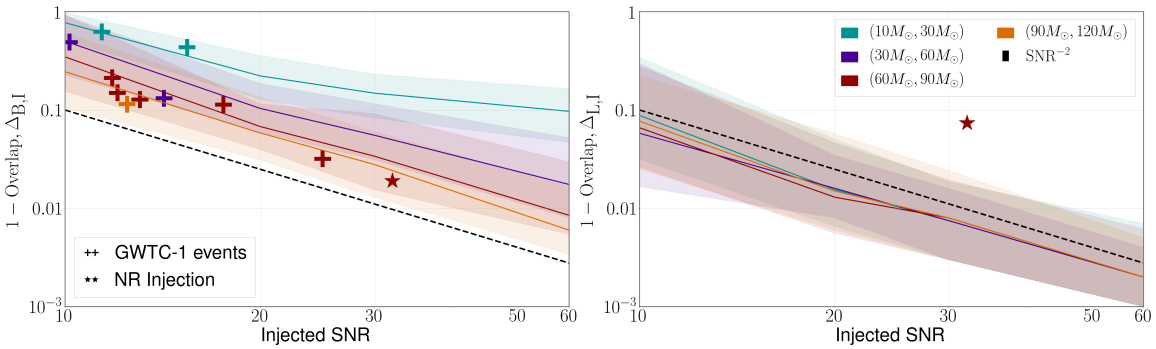

Figure 4.2: Medians (solid lines) and 90% uncertainty bands (shaded regions) of $\Delta_{\mathrm{B,I}}$ (left) and $\Delta_{\mathrm{L,I}}$(right) against the SNR ($\sqrt{\langle \mathbf{h}_{\mathrm{INJ}}, \mathbf{h}_{\mathrm{INJ}} \rangle}$) of the CBC signal colored by the total mass ranges M_T. The black dashed-dot line represents the curve $1/\mathrm{SNR}^2$ which is the expected variation of $\Delta_{\mathrm{B,I}}$ and $\Delta_{\mathrm{L,I}}$ for a signal. The overlaid "+" markers indicate the onsource values of $\Delta_{\mathrm{B,L}}$ plotted against the SNR of the $\mathbf{h}_{\mathrm{LI}}$ waveforms for each of the GWTC-1 events, and are colored by the to M_T of the $\mathbf{h}_{\mathrm{LI}}$ waveform. The overlaid "$*$" markers indicate the values inferred from the NR injection described in Section section 4.6. Figure from [43].

4.4 Application to GWTC-1 detections

I have applied the above analysis to GWTC-1 injections which are simulated signals with parameters are drawn from the posterior distributions of GWTC-1 events. The purpose of these injections is to establish an expectation of the overlap for each GW event, which we then use to compare with the overlap on the actual data. GWTC-1 injections focus on systems specific to events in GWTC-1 to gauge the reconstruction performance of the catalog, whereas the population injections described in the prior section explore trends in the overlap over the range of systems that are detectable in ground-based detectors. To test the reconstruction fidelity for real events, I designed a set of 500 injections, 50 for each of the 10 GWTC-1 events. The parameters of these injections were sampled from their measured `IMRPhenomPv2` [166] posterior probability density functions. I used the `LALInference` posterior samples files available on the Gravitational Wave Open Science Center (GWOSC) [182] and for each of the above injections, compute the "offsource" overlap ($\mathcal{O}_{\mathrm{OFS}} = \langle \mathbf{h}_{\mathrm{LI}} | \mathbf{h}_{\mathrm{BW}} \rangle$). I then compared the distribution resulting from these 50 $\mathcal{O}_{\mathrm{OFS}}$ values with the "onsource" overlap ($\mathcal{O}_{\mathrm{ONS}} = \langle \mathbf{h}_{\mathrm{LI}} | \mathbf{h}_{\mathrm{BW}} \rangle$) obtained from the data containing

the real event.

Since the parameters of these events are mostly consistent with nearly equal mass, spin-aligned systems with little to no evidence for precession, we expect the $\mathcal{O}_{\text{ONS}}$ value(s) to be no worse than the $\mathcal{O}_{\text{OFS}}$ overlaps(s).

We quantify this consistency using the p-value which we define as the fraction of $\mathcal{O}_{\text{OFS}}$ that are less than or equal to $\mathcal{O}_{\text{ONS}}$,

$$p \coloneqq P(\text{O}_{\text{OFS}} \leq \text{O}_{\text{ONS}}). \tag{4.2}$$

A small p-value indicates a small chance that the onsource reconstruction performance is consistent with expectation. This could be due to features in the onsource data that corrupt the reconstruction performance, either astrophysical or terrestrial.

I plotted $\mathcal{O}_{\text{ONS}}$ as a function of $\mathcal{O}_{\text{OFS}}$ for each BBH in GWTC-1 in Fig. Figure 4.3. Due to variations in the parameter posteriors and/or noise properties, the distribution of O_{OFS} has a spread. The overlaid diagonal line here ($y = x$) represents the null hypothesis that the $\mathcal{O}_{\text{OFS}}$ and $\mathcal{O}_{\text{ONS}}$ are equal. Dots represent the median and the horizontal error bars are the 90% credible intervals of the $\mathcal{O}_{\text{OFS}}$ distributions. From Fig. Figure 4.3, we find that all events are consistent with $y = x$ within 90% credibility. The median of $\mathcal{O}_{\text{OFS}}$ decreases and its spread increases with decreasing SNR and M_T of the event. For example, GW150914 with an SNR ~ 24 and $M_T \sim 65M_\odot$ has a larger $\mathcal{O}_{\text{OFS}}$ median and a smaller spread compared to GW170823 which has a similar M_T but has SNR ~ 11. Similarly, GW170729, with a $M_T \sim 84M_\odot$ and SNR ~ 10 has a larger median value and a smaller spread compared to GW151012 with similar SNR but $M_T \sim 27M_\odot$.

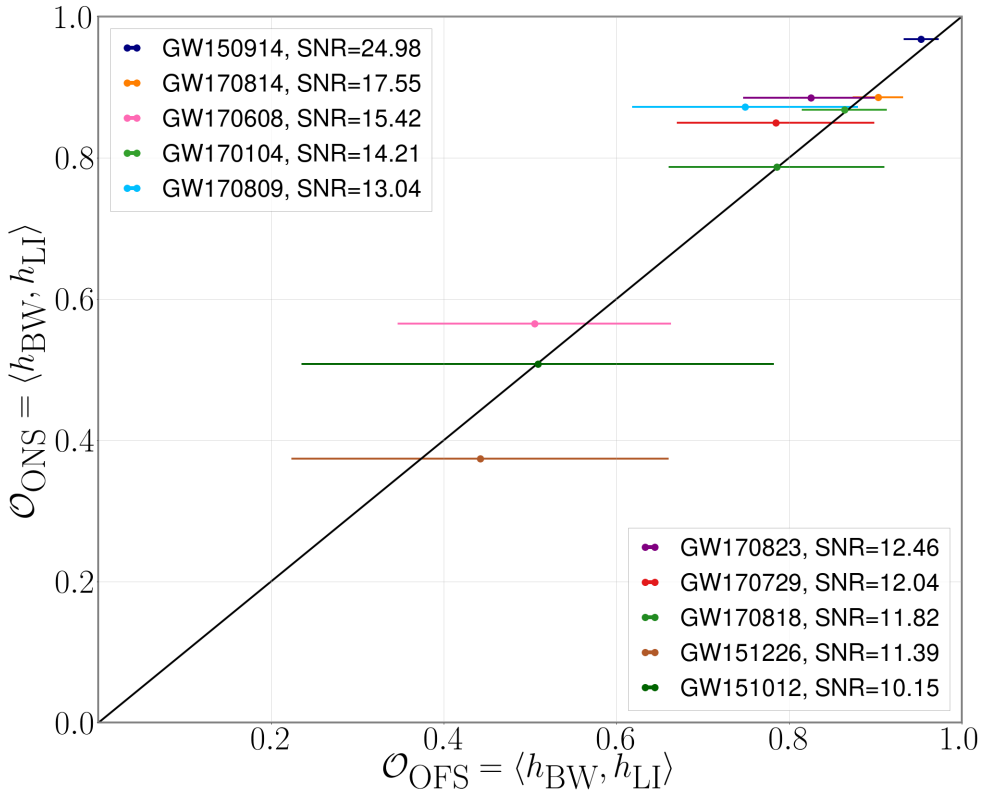

Figure 4.3: Onsource overlap (y-axis) plotted against the median offsource overlap (x-axis) for each of the GWTC-1 events. The horizontal error bars are the 90% credible intervals in the overlap. The diagonal black line is $y = x$. Figure from [43].

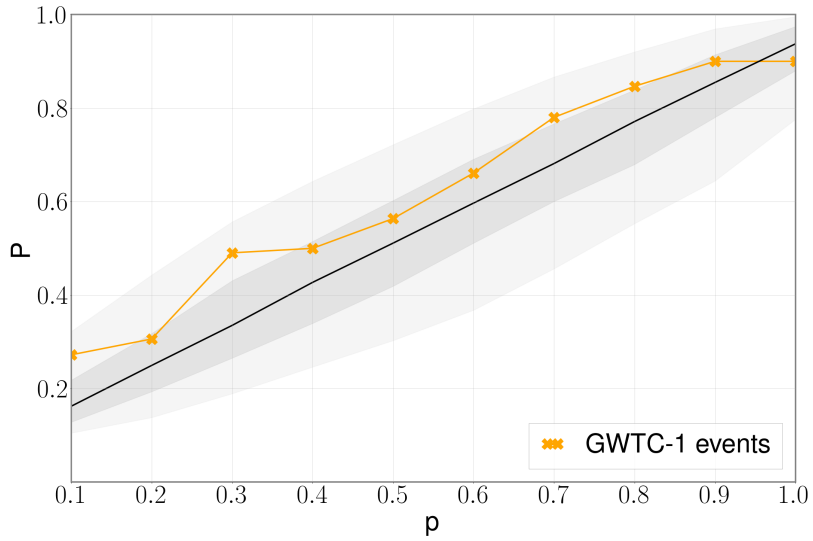

Figure 4.4: p-values (P) of GWTC-1 events (orange) plotted against the cumulative fraction events (p), along with the null hypothesis (black) and the 50% and 90% credible intervals (shaded regions). Figure from [43].

I computed the p-values and record them in Table Table 4.2. We find that the p-values are broadly consistent with the null hypothesis that the onsource performance is no worse than the offsource performance. The lowest p-value that we compute is for GW151226 at 0.27. Assuming the null hypothesis to be true for all events, we expect the p-values to be uniformly distributed between 0 and 1. I followed a procedure similar to [50], and used Fisher's method [185] to compute the population p-value (p_{pop}) of the distribution of p-values. A p_{pop} close to 1 indicates higher evidence for the population null hypothesis, and a p_{pop} less than 0.05 is considered low enough to reject the population null hypothesis. I obtained a $p_{pop} = 0.95$ which indicates that there is no evidence for aberrant behavior in the onsource reconstruction performance as compared to the offsource injections.

I also plotted the p-values against the cumulative fraction of events in Fig. Figure 4.4. The black line represents the null hypothesis that the p-values are uniformly distributed, and the shaded bands represent the 50% and 90% credible intervals. The orange curve is consistent with the black line within the 90% credible interval. Overall, this means that the agreement between the `BayesWave` and template waveforms for GWTC-1 events is statistically consistent with expectation.

Table 4.2: p-values of GWTC-1 events computed by comparing the onsource overlap of $\langle \mathbf{h}_{\rm LI}, \mathbf{h}_{\rm BW} \rangle$ versus the offsource distribution of the same. Table from [43].

Event	p-value
GW150914	0.90
GW151012	0.49
GW151226	0.27
GW170104	0.56
GW170608	0.66
GW170729	0.78
GW170809	0.90
GW170814	0.30
GW170818	0.50
GW170823	0.84

As an additional test of consistency, I overlayed the values obtained from the onsource results of the GWTC-1 events in Fig. Figure 4.2. Specifically, I plotted the $\Delta_{\rm B,L}$, the complement of the overlap between $\mathbf{h}_{\rm BW}$ and $\mathbf{h}_{\rm LI}$ against the SNR of the $\mathbf{h}_{\rm LI}$ given by $\sqrt{\langle \mathbf{h}_{\rm LI}, \mathbf{h}_{\rm LI} \rangle}$, using $\mathbf{h}_{\rm LI}$ as a proxy for the true waveform. I justify this approximation by noting from Figure 4.2 that $\Delta_{\rm L,I}$ is less than 0.1 which is an order of magnitude smaller than $\Delta_{\rm B,I}$. The markers are colored according to the color scheme of the M_T parameter as shown in Fig. Figure 4.2. We find that the $\Delta_{\rm B,L}$ values fall within the bounds obtained from the population injections.

The above procedure is computationally expensive for the offsource runs since my studies show that a single `LALInference` run can take approximately 5 times as many computing resources as a single `BayesWave` run. A cheaper alternative for the offsource overlap $\rm O_{OFS}$ is to use the overlap between the recovered `BayesWave` waveform and the injection, i.e $\mathcal{O}_{B,I}$. The right panel of Figure 4.2 shows that the misoverlap between the `LALInference` waveform and the injection is an order of magnitude smaller than the misoverlap between `BayesWave` and the injection. This means that from the point of view of `BayesWave`, the injected signal and the recovered `LALInference` signal are nearly identical. However, $\mathcal{O}_{B,L}$ will always be slightly higher than $\mathcal{O}_{B,I}$ since the `LALInference` waveform includes the effect of the noise realization that is included in

the BayesWave reconstruction. The injected signal, however, does not include information about the noise realization. Hence, we can use $\mathcal{O}_{B,I}$ for the p-value calculation in Equation 4.2 while keeping in mind that the returned p-value is marginally higher than the true value. Indeed we see this in Figure 4.5 where $\mathcal{O}_{\mathrm{B,L}}$ plotted on the y-axis is generally higher than $\mathcal{O}_{\mathrm{B,I}}$. The increased p-values are then seen in Figure 4.6.

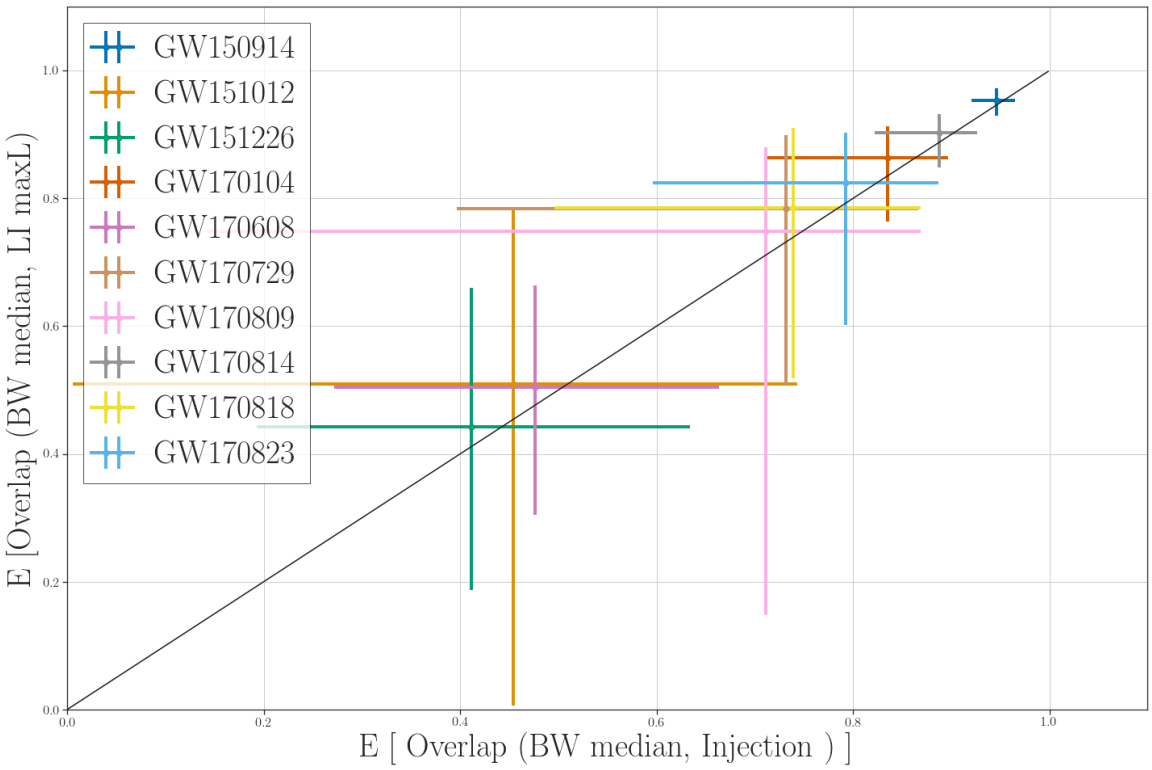

Figure 4.5: Comparison of offsource overlaps of BayesWave with injected waveform (x-axis) and BayesWave with the recovered LALInference waveform (y-axis).

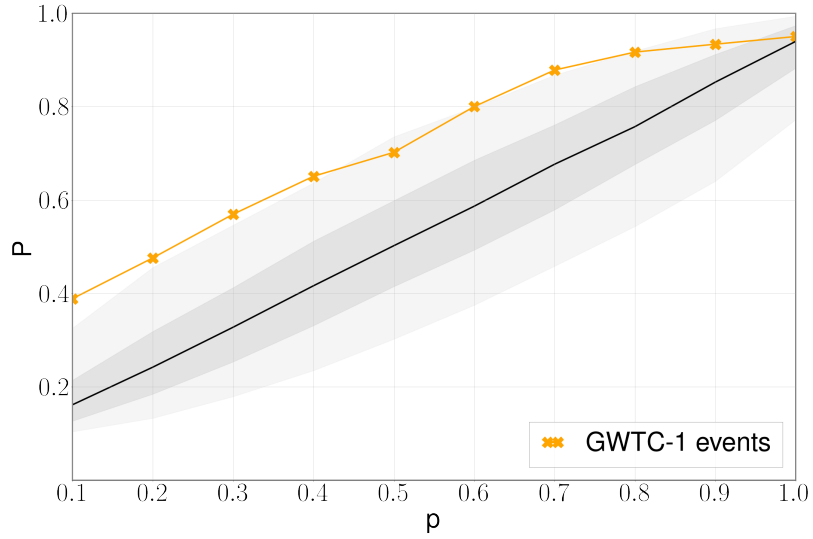

Figure 4.6: p-values (P) of GWTC-1 events (orange) plotted against the cumulative fraction events (p), along with the null hypothesis (black) and the 50% and 90% credible intervals (shaded regions).

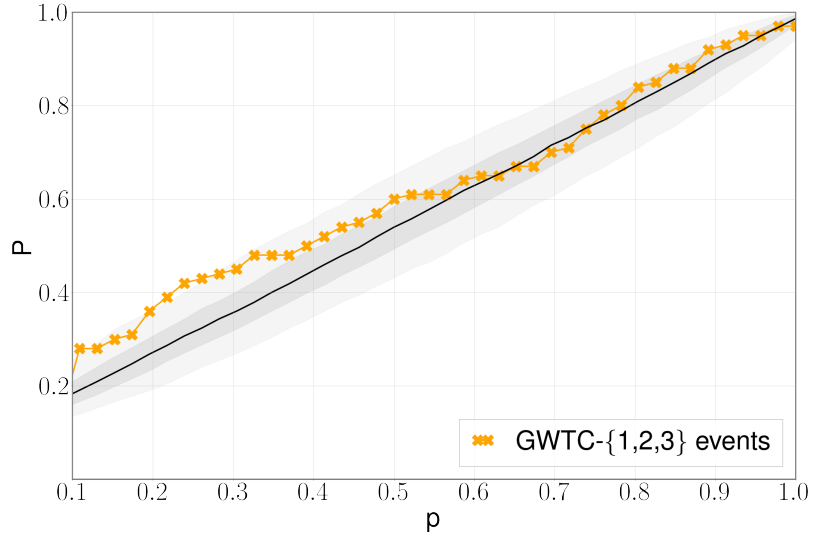

Figure 4.7: p-values (P) of GWTC-{1,2,3} events (orange) plotted against the cumulative fraction events (p), along with the null hypothesis (black) and the 50% and 90% credible intervals (shaded regions).

4.5 Application to GWTC-{1,2,3} detections

The LIGO and Virgo collaboration applied this procedure to significant BBH events from GWTC-2 and GWTC-3. The results of these have been included in the respective cat-

Table 4.3: p-values of GWTC-{1,2,3} events computed by comparing the onsource overlap of $\langle \mathbf{h}_{\rm LI}, \mathbf{h}_{\rm BW} \rangle$ versus the offsource distribution of $\langle \mathbf{h}_{\rm Inj}, \mathbf{h}_{\rm BW} \rangle$.

Run	Event	p-value
O1	GW150914	0.95
	GW151012	0.48
	GW151226	0.7
O2	GW170104	0.8
	GW170608	0.93
	GW170729	0.92
	GW170809	0.88
	GW170814	0.65
	GW170818	0.39
	GW170823	0.57
O3a	GW190408_181802	0.61
	GW190412	0.85
	GW190421_213856	0.5
	GW190503_185404	0.64
	GW190512_180714	0.84
	GW190513_205428	0.55
	GW190517_055101	0.36
	GW190519_153544	0.42
	GW190521	0.14
	GW190521_074359	0.54
	GW190602_175927	0.11
	GW190630_185205	0.48
	GW190706_222641	0.43
	GW190707_093326	0.78
	GW190708_232457	0.65
	GW190720_000836	0.08
	GW190727_060333	0.6
	GW190728_064510	0.71
	GW190814	0.28
	GW190828_063405	0.31
	GW190828_065509	0.61
	GW190910_112807	0.09
	GW190915_235702	0.3
	GW190924_021846	0.28
O3b	GW191109	0.45
	GW191129	0.61
	GW191204	0.95
	GW191215	0.88
	GW191216	0.44
	GW191222	0.67
	GW200129	0.52
	GW200208	0.48
	GW200219	0.67
	GW200224	0.97
	GW200225	0.97
	GW200311	0.75

alog papers, and I was responsible for designing and deploying the analysis. Note that for GWTC-2, the approximant used in PE is `IMRPhenomPv2` and the algorithm used is `LALInference`. For GWTC-3, the approximant is `IMRPhenomXPHM` and the algorithm is `Bilby`. The p-values from GWTC-1, GWTC-2, and GWTC-3 are plotted in Figure 4.7 and tabulated in Table 4.3. I also calculate the p_{pop} using Fisher's method and obtain $p_{pop} = 0.99$.

4.6 Detecting deviations in templates

My analysis so far has been focused on the agreement between `LALInference` and `BayesWave` reconstructions. The results serve as a reference to check for consistency

in future observations, and to identify outliers due to potential disagreements between reconstructions. These disagreements could arise for example due to higher order modes, highly precessing orbits, deviations from GR or noise. I demonstrate one such example of an injection of BBH GW signal containing higher order modes. In the GR, BBH signals are typically dominated by the $(l, |m|) = (2, 2)$ spherical harmonic mode. This is true for most signals that are detectable by ground-based detectors, and especially for binaries with comparable mass components observed face-on. `IMRPhenomPv2` waveforms do not account for the presence of higher order modes.

The relative power of higher order modes to the dominant mode is most dependent on the mass ratio and the inclination angle [186]. To demonstrate this, I consider the case of NR simulation `GT0745` from the Georgia Tech NR catalog [187]. This system has a component mass ratio of $6:1$. I placed the system in the "edge-on" configuration where the angle between the line of sight and the normal vector to the plane of the orbit, known as the inclination angle, is $90°$. A combination of unequal masses and edge-on inclination yields a high higher order mode content in the waveform. I also set the distance such that SNR~ 30.

I injected the waveform into a noise realization set equal to zero, and analyze the data stream using both `LALInference` and `BayesWave`. Since we assume that the noise is Gaussian, the expectation value of the noise stream **n** over multiple noise realizations is 0. Hence the performance of the algorithms on zero noise data is the "average" result over many noise realizations [188].

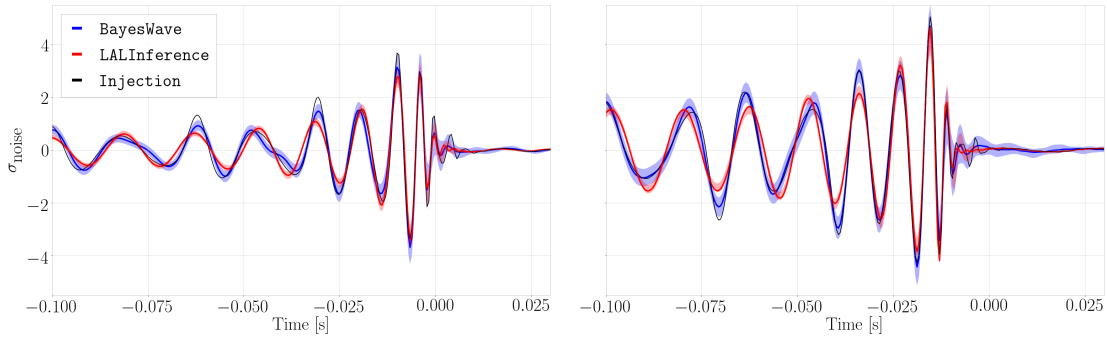

Figure 4.8: LALInference(red), BayesWave (blue), and the injected waveform (black) for the injection analysis performed using the Georgia Tech NR waveform GT0745. The plotting conventions are similar to Fig. Figure 4.1. Note the disagreement between $\mathbf{h}_{\rm LI}$ and $\mathbf{h}_{\rm BW}$, especially before -0.04 seconds. Figure from [43].

I computed the overlaps $\mathcal{O}_{\rm B,I}$, $\mathcal{O}_{\rm L,I}$ and plotted all three waveforms in Figure 4.8. Inspecting the SNRs and overlaps in Table Table 4.4, we find that BayesWave reconstructs the injection more faithfully than a LALInference analysis uses a model without higher order modes. This is also reflected in the fact that the former is able to recover a larger SNR compared to the latter. I plotted $\Delta_{\rm L,I}$ and $\Delta_{\rm B,I}$ (red stars) in Figure 4.2. As we see, the former is an outlier, while the latter falls within the confidence band based on expectations from simulated signals. In case of a real detection with potential un-modeled effects, it will not be possible to calculate $\Delta_{\rm L,I}$ and $\Delta_{\rm B,I}$ since we cannot know the true waveform. The quantity of interest is $\Delta_{\rm B,L} = 1 - \mathcal{O}_{\rm B,L}$. In this particular case, I computed the $\Delta_{\rm B,L} = 0.06$ which lies outside the 90% credible interval of the distribution of $\Delta_{\rm B,L}$ obtained from the population injections.

Table 4.4: SNRs and Overlaps for a LALInference and BayesWave analysis on an injection, Georgia Tech NR waveform GT0745 with $M_T = 60M_\odot$ and mass ratio, $q = 6$, that includes higher order modes. BayesWave recovers a larger part of the waveform since LALInference with IMRPhenomPv2 does not include higher order modes. Table from [43].

IFO	LI SNR	BW SNR	Inj SNR	$\langle h_{\rm LI}, h_{\rm INJ}\rangle$	$\langle h_{\rm BW}, h_{\rm INJ}\rangle$
Hanford	14	15	16	0.94	0.96
Livingston	24	26	28	0.92	0.98
Network	28	30	32	0.92	0.98

I note that approximants that include higher order modes exist as discussed in Table 4.1, and the above is only meant as an exercise to demonstrate how a disparity between `LALInference` and `BayesWave` would manifest itself.

4.7 The hunt for higher order modes

. I applied the signal waveform consistency test to hunt for higher order modes in two events: GW170729 and GW190412.

4.7.1 GW170729

GW170729 was (at the time) the heaviest BBHdetected by LIGO and Virgo. As I showed in Figure 3.4, heavier BBH systems coalesce at lower frequencies since the waveform spectrum shifts down linearly with the total mass of the binary. In the case of GW170729, most of the inspiral cycles were at frequencies 8 Hz. As can be seen from Figure 2.4, LIGO and Virgo are not sensitive at these frequencies and only observed the last few cycles of the GW inspiral. higher order modes become relevant during the late inspiral and merger-ringdown phase of the GW waveform due to the non-linear effects of GR at small orbital separations. Additionally, since higher order mode amplitudes become significant in asymmetric mass ratio binaries, GW170729's inferred mass ratio (m_2/m_1 = 0.3 to m_2/m_1 = 0.8), made it a prime candidate for detecting higher order modes.

In Chatziioannou et al. [48], we performed PE with and without approximants containing higher order modes and find the Bayes Factors of 5.1:1 in favor of higher order modes compared to models without them. However, this is consistent with the fact that higher order mode approximants like `IMRPhenomHM` have more power compared to dominant mode approximants like `IMRPhenomPv2` due to the inclusion of a larger number of waveform modes in the former.

As a different approach, I compared the reconstructed GR template-based signals with `BayesWave` signals and find that overlaps of waveforms with higher order modes are

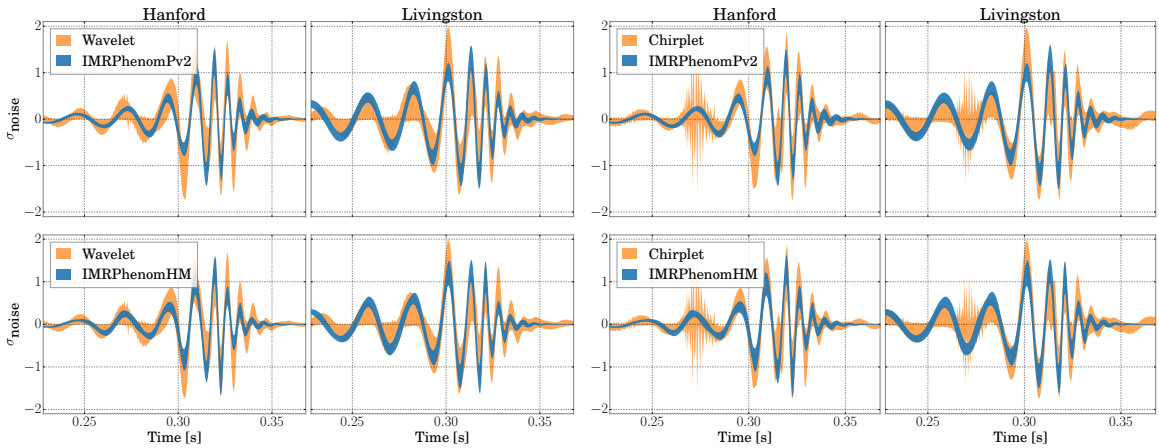

Figure 4.9: Waveform comparisons for GW170729. I plot the 90% credible interval of the whitened strain data as a function of time for each of the LIGO detectors computed with CBC waveform models (blue) and BayesWave (orange). The top plots show `IMRPhenomPv2` while the bottom plots show `IMRPhenomHM`. The left plots use the wavelet model of `BayesWave`, while the right plots use the chirplet model. The x-axis represents the time in seconds from the nearest integer GPS time before the event. The y axis represents the whitened strain amplitude. The generic signal reconstruction is consistent with the template signal reconstruction both when the latter includes higher-order modes and when it does not. Figure from [48].

slightly higher than the ones without. Figure 4.9 shows the comparison of the `BayesWave` reconstruction with the two approximants: `IMRPhenomPv2` and `IMRPhenomHM`. Table 4.5 shows the overlaps of the maximum-likelihood waveform of different template-based approximants with the `BayesWave` reconstruction. Note that the overlap is consistently higher for chirplets and is higher for the approximants containing higher order modes. As far as `BayesWave` is concerned, the inclusion of higher order modes is favored. However, since the increase in overlap is of a few percent, this did not exclude `IMRPhenomPv2` from the set of models that sufficiently describe GW170729.

Table 4.5: Overlaps between the median BayesWave reconstruction and the maximum likelihood template waveform with different waveform models for GW170729. Table from [48].

	Wavelets	Chirplets
IMRPhenomPv2	0.88	0.90
IMRPhenomD	0.87	0.89
IMRPhenomHM	0.89	0.90
SEOBNRv4	0.87	0.90
SEOBNRv4HM	0.88	0.89

4.7.2 GW190412

GW190412 was (at the time of this analysis) the loudest BBH system detected by LIGO and Virgo with asymmetric mass ratios: a $30M_{\odot}$ mass merging with a $6M_{\odot}$ mass. Since higher order modes are more prevalent in systems with asymmetric mass ratios and high inclination, GW190412 was a prime candidate to study them. Indeed through various analyses, the LIGO and Virgo collaboration found evidence for higher order modes. I participated in the signal consistency test for this event and found that the overlap of the BayesWave reconstruction grew with the inclusion of higher order modes and precession in the waveform approximants. For this particular case, I computed the overlap between the median BayesWave waveform and 200 template waveforms corresponding to random draws from the parameter estimation samples.

For the models of the EOBNR family, I find that the agreement with the unmodeled BayesWave reconstruction increases slightly from overlaps of $0.84^{+0.01}_{-0.02}$ (median value and 90% errors) for the dominant-multipole, nonprecessing model (SEOBNRv4_ROM) to $0.86^{+0.01}_{-0.02}$ when higher order modes are included (SEOBNRv4HM_ROM), to $0.88^{+0.01}_{-0.02}$ for the most complete EOBNR PHM model (SEOBNRv4PHM) that includes precession and higher order modes. The increasing overlaps are consistent with the findings of the other meth-

ods presented in this section which indicate that the extra physical effects included in the higher order mode precessing model match the data better. The Phenom family shows a similar trend. The overlap for nonprecessing dominant multipole model is $0.85^{+0.01}_{-0.03}$ (`IMRPhenomD`) , and it increases to $0.84^{+0.02}_{-0.02}$ for the nonprecessing higher multi-poles model (`IMRPhenomHM`), to $0.86^{+0.02}_{-0.02}$ for the precessing higher order mode model(`IMRPhenomPv3HM`). Similar to GW170729, the waveform comparison method favors the higher order mode approximants but does exclude the dominant-mode approximants as from the set of models that describe GW190412.

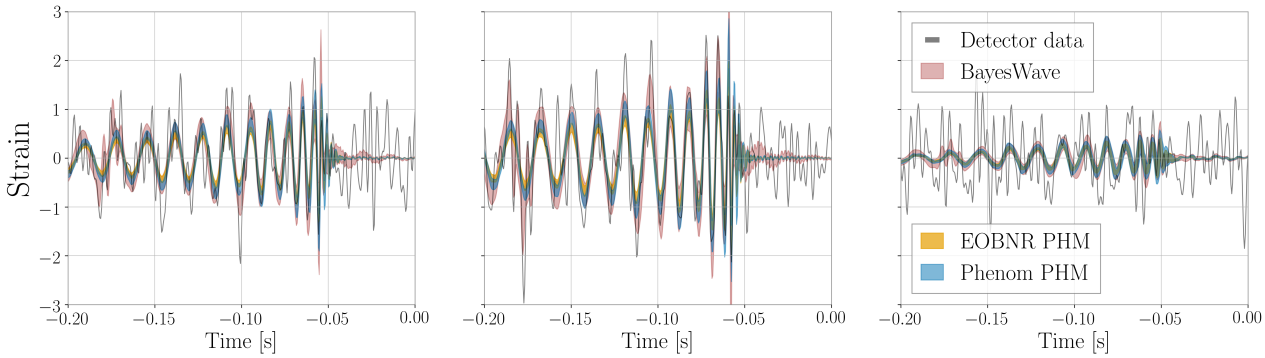

Figure 4.10: Waveform comparisons of the gravitational waveform of GW190412 in the LIGO Hanford, LIGO Livingston, and Virgo detectors (from left to right). Plot shows detector data (gray), `BayesWave` reconstruction (red) and the template reconstructions from `IMRPhenomPv3HM` (blue) and `SEOBNRv4PHM` (gold). The bands indicate the 90% credible intervals at each time. Figure from [140].

4.8 Inferring the BBH remnant spin from model-independent reconstructions

Another novel use of `BayesWave` waveform reconstructions is in inferring properties of the remnant black hole from a BBH coalescence. In [189], Healy et al derive a relationship between the instantaneous frequency at the peak of the GW emission to the coefficients of the quasi-normal modes. Although it is not obvious that such a relationship should exist, empirical studies of NR simulations point to the presence of such a relationship.

Following that work, in Ferguson et al [49], we infer the dimensionless remnant spin (a_f) using the observed quantities the instantaneous frequency at maximum amplitude

(ω_{peak}), the derivative of the instantaneous frequency at maximum amplitude ($\dot{\omega}_{peak}$), the chirp mass ($\mathcal{M}$) via a empirical relationship from NR. The relation between these quantities using non-precessing NR simulations is:

$$\hat{\omega}\eta^{\frac{3}{5}} = \omega\mathcal{M} \tag{4.3}$$

and

$$\hat{\dot{\omega}}\eta^{\frac{6}{5}} = \dot{\omega}\mathcal{M}^2 \tag{4.4}$$

where $\hat{\omega}$ is the dimensionless instantaneous frequency, $\hat{\dot{\omega}}$ is the derivative of the dimensionaless instantaneous frequency, η is the symmetric mass ratio defined as a function of the component masses, m_1 and m_2:

$$\eta = \frac{m_1 m_2}{(m_1 + m_2)^2}\,, \tag{4.5}$$

and $\mathcal{M}$ is the chirp mass given through the frequency evolution as using the $(\ell, |m|) = (2, 2)$ from PN approximation:

$$\mathcal{M} = \eta^{\frac{3}{5}} M = \frac{c^3}{G}\left(\frac{5}{96}\pi^{-\frac{8}{3}} f^{-\frac{11}{3}} \dot{f}\right)^{\frac{3}{5}}\,. \tag{4.6}$$

Figure 4.11 shows the spin of the remnant BH against a function of the dimensionless instantaneous frequency at maximum amplitude $(\hat{\omega}_{peak})\eta^{\frac{3}{5}}$ and the derivative of the dimensionless instantaneous frequency at maximum amplitude $(\hat{\dot{\omega}}_{peak})\eta^{\frac{6}{5}}$ which will take the form

$$x = ln\left(\left(\hat{\omega}_{\text{peak}}\eta^{\frac{3}{5}}\right)^{-\frac{11}{5}}\left(\hat{\dot{\omega}}_{\text{peak}}\eta^{\frac{6}{5}}\right)^{\frac{4}{5}}\right). \tag{4.7}$$

Taking the same form as Healy et al, we get the following relationship:

$$a_f = -0.216x^3 + 0.415x^2 - 0.252x + 0.989, \tag{4.8}$$

with an average error of $\Delta a_f = 0.032$

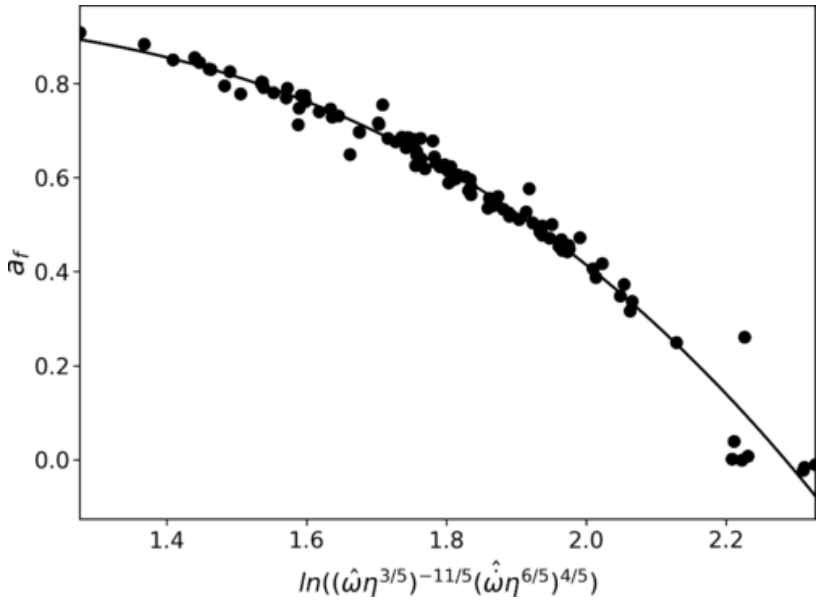

Figure 4.11: Relationship between ω_{peak}, $\dot{\omega}_{peak}$, $\mathcal{M}$ and a_f. Figure from [49].

To test the reliability of this fit in inferring the spin, we performed a set of 2000 injections with parameters similar to GW150914, and SNR set 100. We added the injections to simulated LIGO data with O1 era sensitivity and analyze them with `BayesWave`. We then use the waveform reconstructions to obtain ω and $\dot{\omega}$. ω is obtained by first calculating the amplitude envelope of the median whitened `BayesWave` waveform using the Hilbert-Huang transform [190] then calculating the time of maximum amplitude. Then we used the median frequency-evolution curve given by `BayesWave` to infer the instantaneous frequency and the time derivative of the instantaneous frequency at the given time. Note that although our `BayesWave` analysis is performed over the two detector network (LIGO Hanford and LIGO Livingston), we only used the `BayesWave` reconstructions from LIGO Livingston for inferring ω and $\dot{\omega}$.

$\mathcal{M}$ can be obtained from a burst search such as coherent wave-bursts (cWB) which gives an accurate estimation of the inspiral frequency evolution [40]. Past studies with cWB have shown that that the uncertainty in $\mathcal{M}$scales as ~ 1.5/SNR which contributes an additional uncertainty of 1.26/SNR to a_f. In the SNR=100 runs, this adds an uncertainty of 1.26 x 10^{-2} to a_f

The observed quantities are obtained by purely model-independent methods. ω_{peak} and $\dot{\omega}_{peak}$ are obtained by `BayesWave`, while $\mathcal{M}$ is given by cWB.

We plotted the cumulative distribution function of a_f obtained from the 2000 injections in Figure 4.12. The red vertical line is the true value of a_f while the solid (dashed) line denotes the median(90% confidence interval). The plot shows that the inferred value matches well with the true value. With increasing detector sensitivities in the future, this method would be an important independent test of inferred spin parameters.

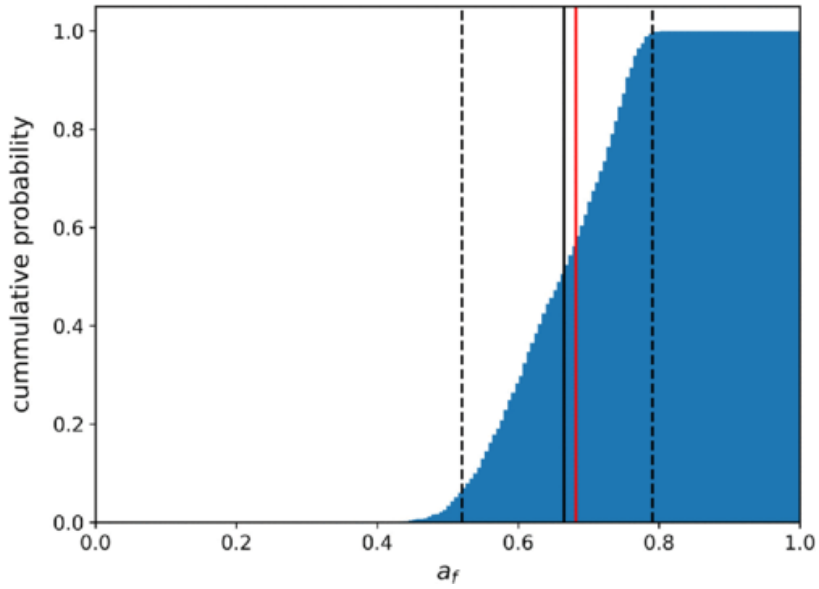

Figure 4.12: Histogram of the recovered spin from `BayesWave` analysis and using Equation 4.8. Figure from [49].

4.9 Conclusions

In this chapter, I showed a signal consistency test using the agreement `BayesWave` and template reconstructions. I also showed how to use model-independent reconstruction to

hunt for un-modeled or poorly-modeled effects, and demonstrated how a potential deviation from models would manifest. I applied the methods to two events GW170729 and GW190412 which were strong candidates for higher order modes. Finally, I described a method of inferring the spin of a BBH remnant using quantities estimated by model-independent methods. Future works could include applying and characterizing the strength of the signal consistency test to complicated systems involving higher order modes, or other GW sources such as core-collapse supernovae.

CHAPTER 5

EMPIRICALLY TESTING FOR DEVIATIONS IN GENERAL RELATIVITY

GR is a highly non-linear theory and only the most trivial cases are completely analytically solvable. We use a wide range of analytical approximations and numerical techniques as discussed in section 3.4 and section 4.1. These predict the physics of compact objects and gravitational waves and we use them to model the systems that we study. It is also, however, important to constantly test our models and Tests of GR (TGR) place constraints on potential deviations using gravitational wave events detected by LIGO and Virgo such as in [191, 192, 51, 193])

Discovery analyses report constraints on parameters within the realm of GR, while TGR reports constraints on deviations from GR. For this, TGR typically employs stricter event selection criteria for events since a minimum loudness is required to perform unambiguous strong-field tests of gravity. For example, GWTC-2 has a total of 44 [8] events that satisfied the selection criterion of false alarm rate (FAR) less than 2 per Julian year whereas the GWTC-2 TGR analysis required FAR of less than 1 per 1000 Julian years which was only satisfied by 24 events. Similarly, of the 35 events in GWTC-3, we apply TGR to subset of 15 events [9].

5.1 Types of tests

TGR analyses within the LIGO-Virgo-KAGRA framework broadly perform four standard tests of GR.

1. Residual test: The residual is constructed by subtracting the best-fit template-based waveform from the detector data. If the template-based waveform models the astrophysical signal correctly, the residual will be consistent with detector noise. To test this, we analyze the residual data stream using `BayesWave`. Since `BayesWave` is a GR model-

independent wavelet-based algorithm its flexibility allows it to reconstruct potential coherent astrophysical features in the data that the template-based model would have missed.

2. Inspiral-merger-ringdown test: The inspiral-merger-ringdown test compares the low and high-frequency parts of the signal. The low-frequency part corresponds to the inspiral while the high-frequency parts correspond to the merger and ringdown. The cut-off frequency f_c is the frequency of the innermost stable circular orbit of the final black hole.

3. Parameterized waveform generation test: The parameterized test of waveform generation analyzes the evolution of the GW phase which directly maps to the orbital phase. An alternate theory of gravity would modify the dynamical evolution of the CBC and this would impart its signature in the GW phase evolution which would be different from GR. The phase evolution is described by frequency-domain coefficients calculated by either analytical or numerical relativity. This test places constraints on the inferred deviations of these coefficients. In the frequency domain, the phase evolution of a non-precessing binary is given by

$$\Phi(f) = \frac{3}{128\eta\, v^5} \sum_k (p_k v^k + p_{kl} v^k \ln v), \tag{5.1}$$

There are two main sub-types of the parameterized waveform generation test: (i) Test Infrastructure for GEneral Relativity (TIGER) approach which modifies the PN terms in the `IMRPhenomPv2` model [194, 195] and the (ii) Flexible Theory-Agnostic (FTA) introduced in [193] and applied to the `SEOBNRv4_ROM` model.

4. Parametrized waveform propagation test: The parameterized tests of waveform propagation explore the possibility of GWs exhibiting a modified dispersion relation due to a massive graviton or Lorentz invariance violation. We use a parameterized dispersion relation as according to [196]

$$E^2 = p^2\, c^2 + A_\alpha\, p^\alpha\, c^\alpha. \tag{5.2}$$

$\alpha = 0$ corresponds to a massive graviton with mass $m_{\rm g} = A_0^{1/2}/c^2$. For all other values of

α from 1 to 4 in steps of 0.5 (except α which is equivalent to a change in c which leaves no observable effect), Equation 5.2 corresponds to a Lorentz-invariance violation. In this model, the GW evolution remains consistent with GR to a good approximation, and the only deviation is due to the de-phasing that builds up during the wave's propagation to earth [192].

The residuals test is the broadest test of potential deviations from GR models since it does not assume an underlying structure to the deviation and is based on testing the consistency of the residual with noise. However, due to its is model-independent nature, it is also not very sensitive in cases where the deviation's amplitude is consistent with noise. In other words, if the SNR of a non-GR or modified-GR waveform is fully recovered by a template, the residuals test fails to report a deviation, while the other tests can potentially succeed.

5. Waveform consistency test We have discussed the waveform reconstruction comparisons as a test of signal consistency in chapter 4. It can also serve as a test of GR and a tool for detecting deviations from GR, similar to the residuals test. Depending upon the type of deviation, it is a weaker or a stronger test than the residuals test. The reconstructions test is most sensitive in cases where the deviation is strong enough for `BayesWave` to have reconstructed the signal waveform and is only able to infer deviations that express as strong departure from GR based models.

In Section section 5.5 I briefly describe the relationship between these tests and discuss the results and implications of the reconstruction and residual tests applied to non-GR waveforms.

5.2 The Gaussian nature of detector noise

We model noise from the detector in the frequency domain as stationary Gaussian with a mean equal to 0 and variance in each frequency bin equal to the PSD. In the absence of any astrophysical signal or terrestrial transient noise, the histogram of the whitened frequency

domain data should appear to be consistent with the standard normal distribution. However, due to the realities of noise coupling, there exist non-Gaussianities and non-stationarities in the data which are not fully captured by the stationary Gaussian model. To test the consistency of the residual with detector noise, we apply the `BayesWave` treatment to 200 random time segments of the same duration and sampling rate at times surrounding the event under consideration. We then check whether the results from the residual are consistent with the background times.

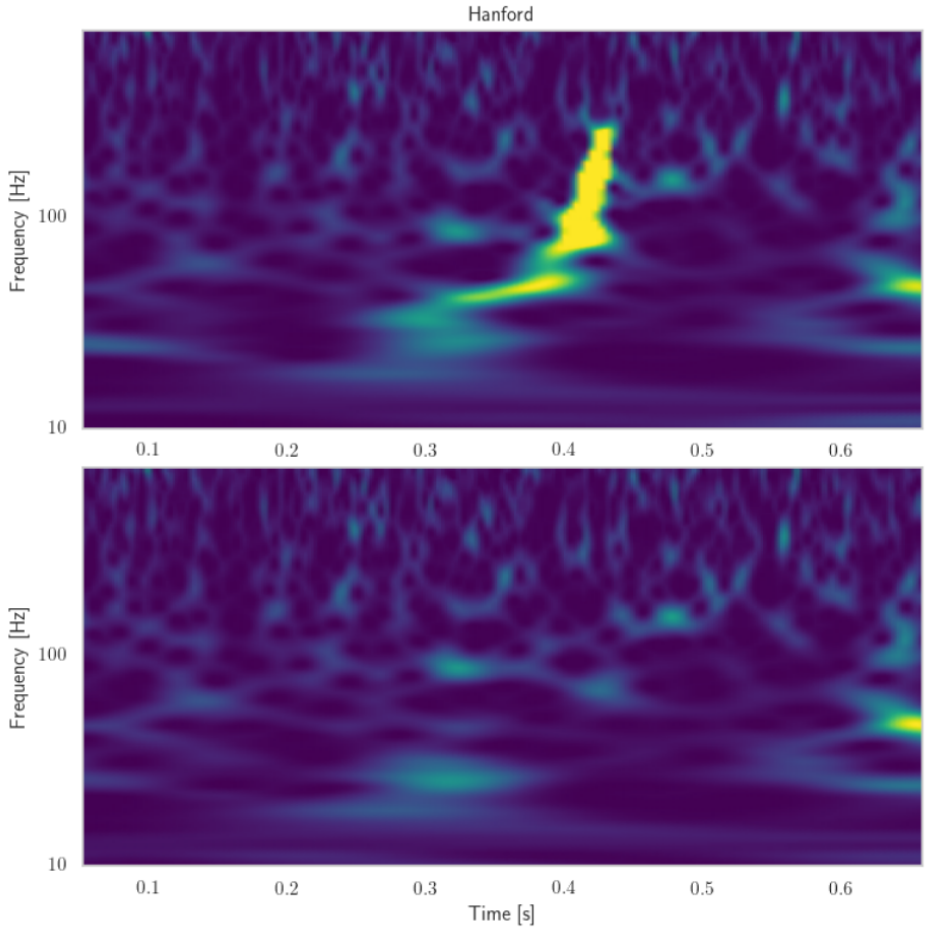

Figure 5.1: Residual data calculation. The top panel shows the time-frequency representation of LHO data for S200129. The bottom panel shows the residual data in the same detector calculated using Equation 5.3.

5.3 Details of the residual generation method

To calculate the residual we subtract the maximum likelihood CBC (max-L CBC) waveform from the data,

$$\mathbf{r}(t) = \mathbf{d}(t) - \mathbf{h}(t) \tag{5.3}$$

, where $\mathbf{r}(t)$, $\mathbf{d}(t)$, $\mathbf{h}(t)$ are respectively the residuals, detector data, and the template-based waveform. The bold-face is used to denote that these quantities are defined over multiple detectors, and t is the time segment over which the analysis is done.

Similar to waveform reconstructions, we use the maximum likelihood estimate of $\mathbf{h}(t)$ since it is the waveform that agrees best with data. I should caution, however, that algorithms like `LALInference`and `Bilby` sample the posterior distribution, not the likelihood distribution. The maximum posterior sample *estimate* from these samples is more accurate compared to the maximum likelihood *estimate*. The maximum posterior waveform sample however is the result of the inclusion of our prior knowledge, and in general, does not represent the best agreement with the data. Hence, we use the maximum likelihood estimate, keeping in mind that PE algorithms are not designed for it. Eventually, it is a compromise we strike due to the limitation of our computational power: in an ideal world, we would know both estimates to arbitrary accuracy. However, simulation studies show that the differences in these two waveform estimates are smaller than the typical amplitudes to which `BayesWave` is sensitive.

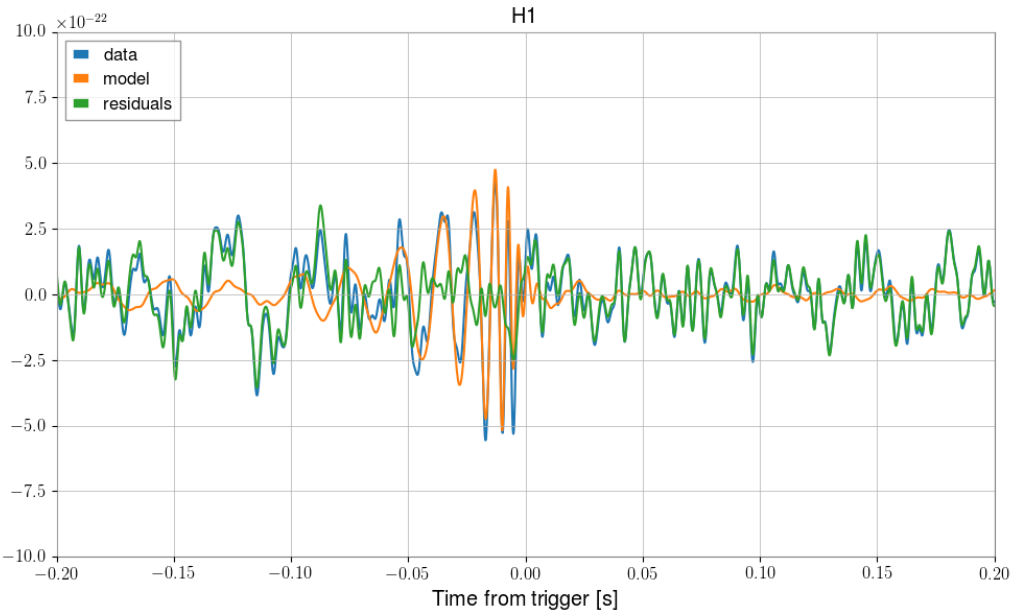

Figure 5.2: Residual calculation time-domain plot for GW200129. The plot shows the detector data (blue), template waveform (orange), and the residual (green) in the LIGO Hanford detector for the GW200129 GW event.

5.4 Analysis with `BayesWave`

We analyze the residual data with `BayesWave` and measure the 90% credible upper limit on the coherent signal-to-noise ratio (SNR_{90}). To check for the consistency of the residual SNR with surrounding detector noise, we analyze randomly selected segments in the time surrounding the event under consideration with `BayesWave` with the same configuration settings. We then similarly compute the $\mathrm{SNR}^{\mathrm{N}}_{90}$ of the noise and compare the onsource SNR_{90} with the $\mathrm{SNR}^{\mathrm{N}}_{90}$ distribution. If the residuals are consistent with the noise, we expect the SNR_{90} to be consistent with the $\mathrm{SNR}^{\mathrm{N}}_{90}$ distribution. Accordingly, our p-value for the null hypothesis that the residuals are consistent with the noise is given by:

$$p = P(\mathrm{SNR}^{\mathrm{N}}_{90} > \mathrm{SNR}_{90}). \tag{5.4}$$

The null hypothesis is that the background is at least as loud as the residual. It is thus a one-side test similar to the p-value calculation with overlaps done in the signal consistency

test. It only indicates when the residual SNR is anomalously higher than the background SNRs. The case of the residual SNR being smaller than most or all the background SNRs is not as alarming as it only indicates that the noise realization for that particular time segment happened to be quieter than the surrounding times, which is very well possible. However, it indicates a necessary increase in background runs since our p-value estimates are only correct to two decimal places.

There has been controversy regarding the use of p-values as the appropriate tool for making statements of significance or inference. Indeed, one can assert a null hypothesis that will trivially be true. However, in this context, our goal is to get an estimate of the probability that our GR-based template model is correct. We reject the null hypothesis when the p-value less than 0.05. When this happens, we investigate the event further.

The LIGO Virgo Collaboration applied tests of GR on events detected during the first (O1), second (O2), and third (O3) observing runs of LIGO and Virgo. I was responsible for designing and deploying the procedure outlined in section A.1 onto events detected in O1 and O2. The results were part of the GWTC-1 tests of GR paper. For events detected during the first half of the third observing (O3a), with the help of James Clark, a research scientist at Georgia Tech, I automated the procedural workflow. The results were part of the GWTC-2 tests of GR paper. For the events detected during the second half of the third observing run (O3b), I completely re-designed the workflow of the reconstruction and residuals analysis into a set of python libraries and scripts named *igwn-wave-compare* (iwc) whose details can be found in Appendix A. I trained and coordinated graduate students Tell Lott and Megan Arogeti, and undergraduate students John Michael Sullivan and Nadia Qutob, who deployed the iwc workflows on the LIGO computing nodes. The results from this were included in the O3b catalog and tests of GR papers.

Table 5.1: p-values of GWTC-1,2,3 events from the residuals analysis.

Run	Event	p-value
O1	GW150914	0.46
	GW151012	0.11
	GW151226	0.81
O2	GW170104	0.99
	GW170608	0.05
	GW170729	0.74
	GW170809	0.78
	GW170814	0.16
	GW170818	0.19
	GW170823	0.85
O3a	GW190408A	0.15
	GW190412A	0.3
	GW190421A	0.07
	GW190503A	0.83
	GW190512A	0.44
	GW190513A	0.7
	GW190517A	0.69
	GW190519A	0.65
	GW190521A	0.28
	GW190521B	0.35
	GW190602A	0.86
	GW190630A	0.52
	GW190706A	0.18
	GW190707A	0.25
	GW190708A	0.19

Run	Event	p-value
O3a	GW190720A	0.18
	GW190727A	0.97
	GW190728A	0.53
	GW190814A	0.84
	GW190828A	0.12
	GW190828B	0.41
	GW190910A	0.65
	GW190915A	0.09
	GW190924A	0.57
O3b	GW191109A	0.55
	GW191129A	0.6
	GW191204A	0.63
	GW191215A	0.91
	GW191216A	0.92
	GW191222A	1.0
	GW200115A	0.16
	GW200129A	0.25
	GW200202A	0.35
	GW200208A	0.97
	GW200219A	0.1
	GW200224A	0.52
	GW200225A	0.05
	GW200311B	0.93
	GW200316A	0.51

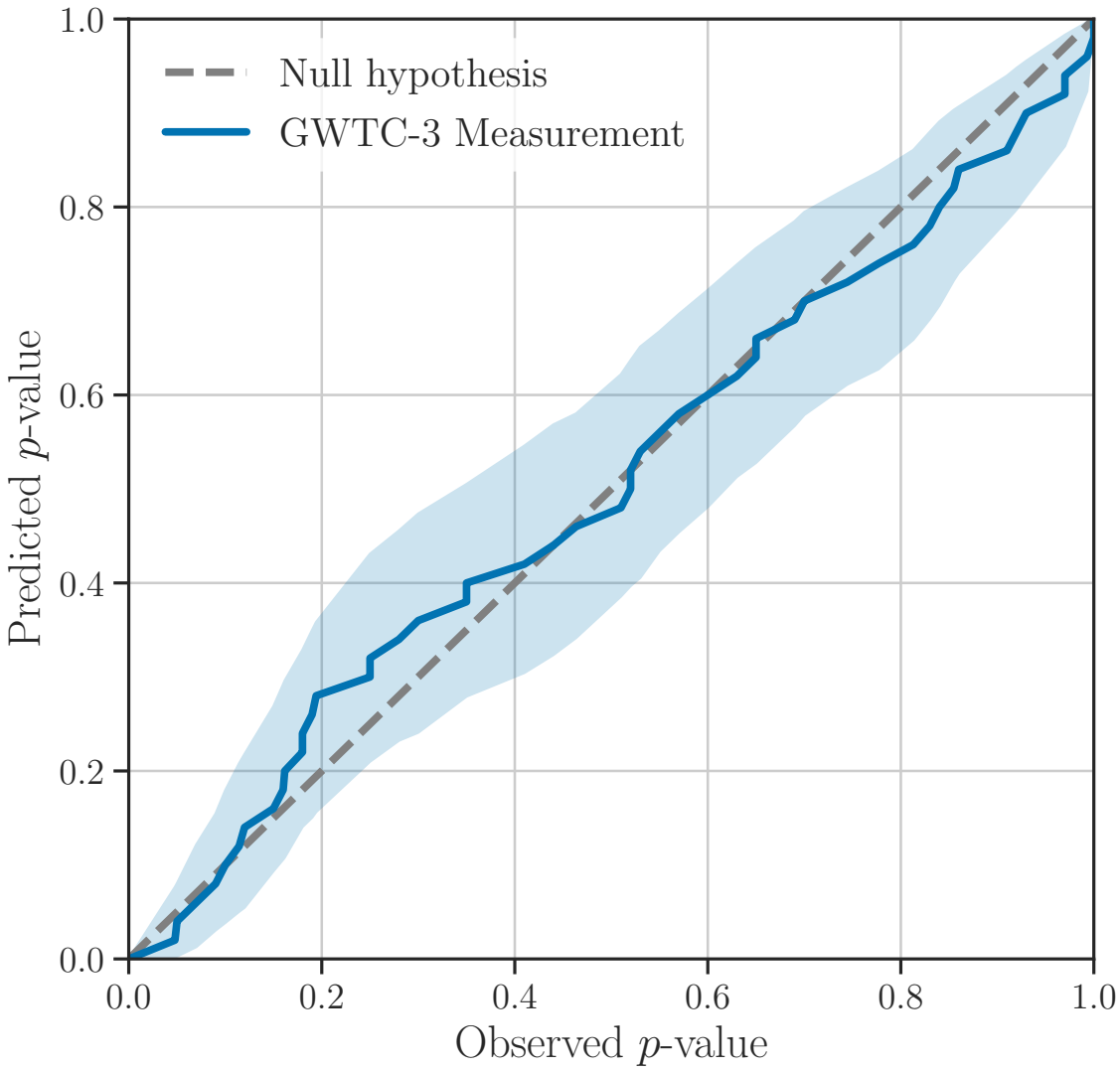

Figure 5.3: Residuals test p-values for GWTC1,2,3

5.5 Application to non-GR phenomenological waveforms

In Johnson-McDaniel et al., we applied the standard set of tests of GR described in section 5.1 onto to simulated waveforms with phenomenological deviations from GR. We consider a variety of simulated observations, both with and without deviations from GR. Specifically, we consider waveforms with the modifications used in both the parameterized tests of GW generation and in the modified dispersion tests and their GR analogs, given by the IMRPhenomPv2 waveform model. The systems we applied the tests to are ones

Table 5.2: Parameters of the waveforms considered in this [44] study (most given to three significant digits): M_z and $D_{\rm L}$ are the binary's redshifted total mass and luminosity distance, while "RA" and "dec." denote the right ascension and declination, respectively. The mass ratio is 1.22 for the (modified) EOB waveforms and 1 for all others and the polarization angle is 3.9 rad in all cases. Each non-GR parameter corresponds to a separate waveform (in the TIGER/FTA case, two different waveforms). Table from [44].

Name	GR parameters						non-GR parameters		
	M_z	$D_{\rm L}$	inclination	RA	dec.	GPS time	mod. EOB	MDR	TIGER/FTA
	$[M_\odot]$	[Mpc]	[rad]	[rad]	[rad]	[s]	a_2	$\widetilde{A}_0$	$\delta\hat{\varphi}_4$
GW150914-like (M_{72})	72.2	452	2.83	1.68	−1.27	1126259462	400	5	−13
							40	1	−2
GW170608-like (M_{20})	19.9	364	2.15	3.64	0.89	1180922494	40	10	−2

with parameters similar to GW150914 [79] and GW170608 [197], as a paradigmatic high- and ($M_T \approx 65M_\odot$) low-mass ($M_T \approx 19M_\odot$) event, respectively. Each type of deviation is described by a parameter. For the GW140914-like cases, we considered *strong* as well as *weak* deviations from GR. The weak deviations have non-GR parameter values an order of magnitude smaller than the strong deviations. For GW170608-like cases, we only considered weak deviations. Note that these non-GR waveforms are purely phenomenological in the sense that the changes are applied to the coefficients in GR approximants. They are not true non-GR waveforms inferred by numerical simulations of alternative theories of gravity. Table 5.2 summarizes the parameters of the various non-GR waveforms we use in this study. The time-domain waveform plots of these signals can be found in Appendix B. We used the "O3low" noise curves from [198] throughout this analysis.

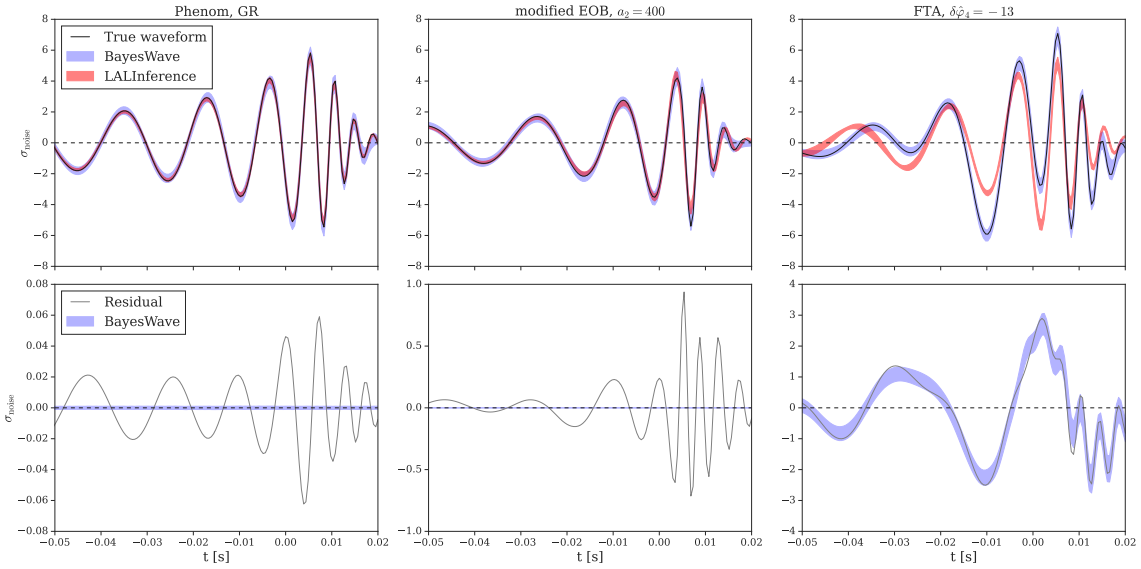

Figure 5.4: The waveform reconstruction and residuals analysis results on three cases of the GW150914-like simulated observations: the Phenom GR case and the modified EOB and FTA cases with larger GR deviations. All quantities are shown here as they would appear in the LIGO Livingston detector. The top panels show the true waveform, `BayesWave` 90% credible intervals (CI), and the `LALInference IMRPhenomPv2` 90 CI. The bottom panels show the residual data and the 90% CI obtained by analyzing it using `BayesWave`. The horizontal axis gives the time from the peak of the waveform, and vertical axis gives whitened strain. Note that the disagreement between the `LALInference` reconstruction and the simulated waveform increases from left to right consistent with the increase of the deviation of the waveform morphology from GR from left to right. This is seen clearly in the bottom panels where the average amplitude of the residual time series grows approximately by an order of magnitude in each plot. Figure from [44].

We found that all of the GW150914-like simulated observations with the larger GR deviation are identified as not consistent with GR at the 90% credible level in at least three tests. We found that the residuals test is only able to identify the TIGER and FTA simulated observations, with their very large GR violations, as deviations from GR. Even though the modified EOB and massive graviton simulated observations also have significant GR violations that are easily picked up by some of the other tests, the distribution of residual SNRs is almost identical to that for the GR simulated observations. This is because the GR analysis can recover most of the SNR in those cases. I illustrated the residuals and their BayesWave recovery in a few cases in the bottom panels of Figure 5.4, which show

the residual detector data in the LIGO Livingston detector and the recovered 90% credible interval with BayesWave. This illustrates that while `BayesWave` can recover the residual signal very well when it is relatively significant, as for the FTA case, it does not find any coherent signal in the residual for the GR and modified EOB cases with their quite small and relatively small residuals, respectively.

The comparison of reconstructions is more sensitive, finding a distribution of overlaps that is disjoint from the one for the GR simulated observations for the modified EOB case, and a clear shift to larger mismatches for the massive graviton case, as well as picking up the very large TIGER and FTA GR violations. This can be seen qualitatively in the top panels of Figure 5.4, where the difference between the `BayesWave` and `LALInference` reconstructions increases from left to right with increasing size of the GR deviation. The reconstruction is also able to recover the most SNR of any analysis for the modified EOB case. However, it only recovers about as much SNR as the GR analysis for the massive graviton simulated observation, likely because the dispersion spreads out the waveform, and the reconstructions do better at recovering short waveforms - the modified EOB, TIGER, and FTA waveforms are all significantly shorter than their GR counterparts.

We found the residuals test to be insensitive to all these smaller modifications of GR, returning SNR distributions that are almost identical to those for the GR simulated observations, likely because the GR analysis recovers almost all of the SNR. The reconstruction comparison finds shifts to larger mismatches for the modified EOB, TIGER, and FTA cases, compared to the GR cases, though not for the massive graviton case. However, there is still considerable overlap of the posteriors in the TIGER and FTA cases. The largest shift is seen for the modified EOB case, and even there the posteriors have some overlap, unlike the disjoint posteriors found in the case with the larger GR deviation.

The BayesWave analyses are also not as well suited to these more spread-out signals as to the shorter GW150914-like signals considered previously.

The comparison of unmodeled and GR reconstructions appears to be more effective at

identifying deviations from GR than the residuals test: The distribution of mismatches between the two reconstructions is well separated from the distribution for the GR waveform in several cases where the residuals test does not identify any deviation from GR, notably for the GW150914-like modified EOB waveform with the larger GR deviation. However, in our analysis, we are only comparing the mismatches between reconstructions to a single GR case and with no noise. The expected distribution of mismatches in the GR case would likely broaden considerably when considering a larger range of GR waveforms and detector noise, considerably weakening these results. Nevertheless, it is likely worth pursuing the reconstruction comparison as a test of GR for high-mass binary black hole signals. It will, however, not apply to low-mass signals, like the GW170608-like cases we consider, where the power is spread out over about a second or more, making it difficult for the unmodeled reconstructions to recover the waveform accurately.

5.6 Conclusions

In this chapter, I described the various tests of GR used in LIGO and Virgo analysis, especially the residuals test, and applied it to GW observations. I described the results of applying the residuals test to non-GR waveforms and found that it is only sensitive to the strongest of deviations. Since it is based on detecting deviations several times louder than the detector noise, it cannot pick up deviations over a single event. Possible future work includes designing a strategy to combine or "stack" the residuals data such that the sensitivity to any potential deviations in the models accumulates over multiple defections.

CHAPTER 6
IMPROVING DETECTOR DATA QUALITY

LIGO and Virgo are highly sensitive instruments designed to measure strains of the order of 10^{-21}. This sensitivity also causes the detectors to be vulnerable to terrestrial noise sources. At any given time, the noise in the detectors can be assumed to be stationary and Gaussian with some non-stationarity over longer timescales. However, events such as human activity, geological events, and feedback in the instrument electronics can give rise to transient noise events, or glitches. A majority of these glitches can be mitigated by identifying the coupling mechanism between auxiliary channels and the GW readout channel and subtracting the resulting amplitude fluctuation.

In some cases, this coupling cannot be identified due to the complexity of the detector control system setup, and glitches are not subtracted out of the data. When a glitch is close (< 2 seconds) to a GW event, it can potentially corrupt or bias PE analyses. Hence, glitches need to be subtracted out of the detector data. In this chapter, I discuss the impacts of glitches on PE, glitch classes, tools used in deglitching data and its challenges, and the improvements in PE.

6.1 Glitches and their causes

Ground-based GW detectors are highly sophisticated instruments with complex control systems, the detectors vulnerable to different noise sources at various frequencies: below (< 10 Hz), Newtonian noise dominates, while above (> 1000 Hz), quantum shot noise dominates. The detectors are most sensitive to stellar-mass CBC events range between 10 Hz to 1000 Hz as shown in Figure 2.3. the In addition to the GW readout photodetector, each detector site also has auxiliary data collection channels which record the time-series data of the environment and the detector feedback system. For example, seismometers, magne-

tometers, anemometers.

Glitches are noise transients due to disturbances in the control system that stabilize the test mass mirrors in the detector. The origin of these perturbations may be terrestrial such as human activity, geological or climatic events, or they could be internal to the control system.

If we assume the interaction between an auxiliary channel, x and the GW readout channel, h, is linear, we can calculate the linear transfer function, T^{XH} [199]

$$T_k^{\mathrm{XH}} = \frac{P_k^{\mathrm{XH}}}{P_k^{\mathrm{XX}}} \tag{6.1}$$

where $P_k^{\mathrm{XH}} \equiv \overline{\widetilde{x}_k \widetilde{h}_k^*}$ is the cross-power spectral density of h and x, and $P_k^{\mathrm{XX}} \equiv \overline{\widetilde{x}_k \widetilde{x}_k^*}$ is the power spectral density of x and h. The overhead bar represents the ensemble average (Welch's method of PSD estimation), the tilde represents the quantities in the frequency domain and the subscript k denotes the value of signals in the k^{th} frequency bin.

Assuming x is a witness to the same glitch as was seen in h, we can calculate x', the transformation of the glitch in from the x channel into the h channel as:

$$\widetilde{x}'_k = T^{\mathrm{XH}} \widetilde{x}_k \tag{6.2}$$

Then the deglitched data is given using

$$\widetilde{h}'_k = \widetilde{h}_k - \widetilde{x}'_k \tag{6.3}$$

where h' is the deglitched data. A witness channel is an auxiliary channel that experiences a glitch coincident with a glitch in the GW channel.

6.2 GW170817

The above procedure is possible only in cases where we know that such a relationship exists, and it is linear. This is often not the case. For example, in the case of GW170817 [200], the first BNS detection, a saturation glitch was coincident with the GW signal in the LIGO Livingston Observatory (LLO).

The glitch in LLO was caused by the saturation in the digital to analog converter in the feedback system for the test masses; its cause was not found, and it was not possible to subtract the glitch time-series from the data using transfer functions. In Figure 6.1, we see the morphology of the GW170817 signal, which tracks the thin bright set of pixels from 60 Hz to 200 Hz across 10 seconds, and the glitch, which is the large bright blob between 40 Hz and 500 Hz and between -2 s to 1 s from the detected time of the merger of the BNS. The signal and the glitch are disjoint in their morphologies. Specifically, if they are both to be modeled by wavelets, the probability distributions of the quality factors of their respective will have wavelets have minimal overlap.

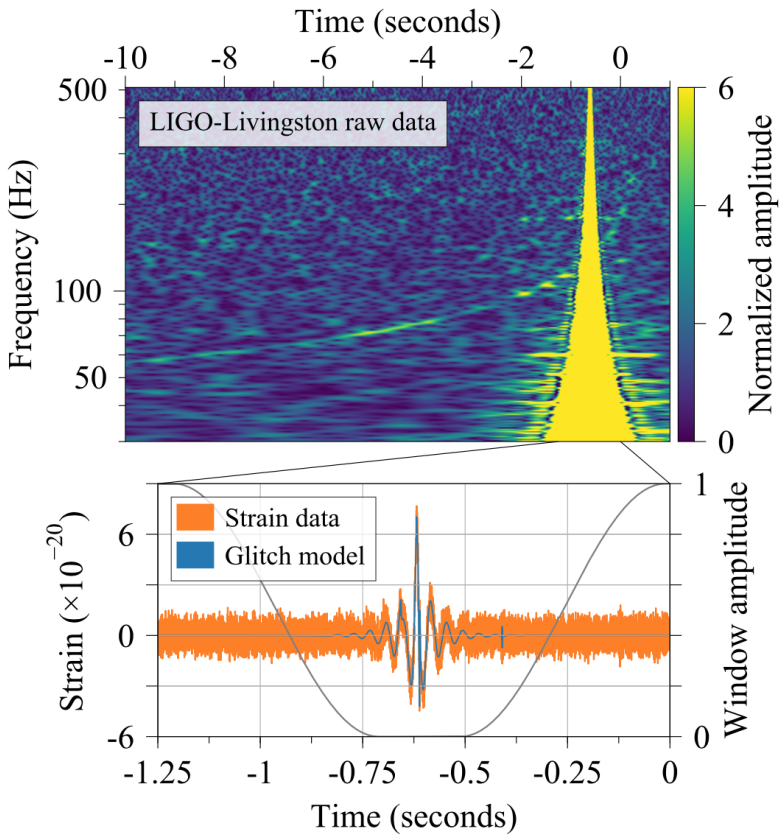

Figure 6.1: The time-frequency spectrogram of the LIGO-Livingston data during GW170817 (top panel). The panel shows the thin band of pixels progressing in frequency (y-axis) from ~ 50 Hz to ~ 200 Hz as time (from coalescence) increases from -10 s to 0 s. The saturation glitch is seen at ~ -1 s covering the entire frequency space shown in the plot. The bottom panel shows a time-domain zoomed-in version of the detector data (orange) and the glitch model (blue) which was subtracted from the data to give glitched "cleaned" data. The cleaned data was used by downstream analyses. Figure from [201].

The LIGO Virgo Collaboration exploited this fact and analyzed the offending segment with `BayesWave` to reconstruct the glitch and placed limits on the wavelet prior quality factor such that the GW signal in the data was not reconstructed by the glitch model. They subtracted the `BayesWave` glitch model from the data to obtain deglitched data which was used by downstream analyses.

6.3 BBH systems in GWTC-{1,2,3}

GW signals from BBH systems are more well-localized in time and spread in frequencies and their morphologies have considerable overlap with glitches some of the commonly occurring glitches. Of the 90 GW events detected so far, 16 were coincident with noise glitches for which `BayesWave` was used to deglitch the data. Figure 6.2 shows the time-frequency representation of a GW150914-like GW signal coincident with a Blip glitch (we discuss Blip classes in section 6.4). In these cases, the task of deglitching is challenging as the data is a superposition of Gaussian noise, transient noise glitch, and astrophysical signal. The `BayesWave` glitch model is unable to distinguish between the signal and glitch parts since it reconstructs any non-Gaussianities by design, be it due to a noise glitch or an astrophysical signal.

Here, I describe the `BayesWaveSignal+Glitch` model which simultaneously fits the signal and glitch parts of the data. The degeneracy in the morphology space is resolved by including at least two GW detectors in the analysis. The signal part of the model, therefore, fits wavelets on parts of the data that are coherent detectors while the glitch model fits the incoherent excess power. The initial implementation of `BayesWave` did not contain the `Signal+Glitch` model, and it is a recent development as described in [45]. Before we delve into its details, however, it is important to introduce the most frequent glitch morphologies.

6.4 Glitch classes

We classify glitches according to their appearance in their spectrogram. The various glitch classes are named based on the categorization by the Gravity spy project [202], a citizen-science project that uses human input to visually categorize glitches using their spectrogram images. Gravity spy uses a machine learning (convolutional neural networks) back-end to train and apply this categorization to larger datasets. Here, we describe the most common

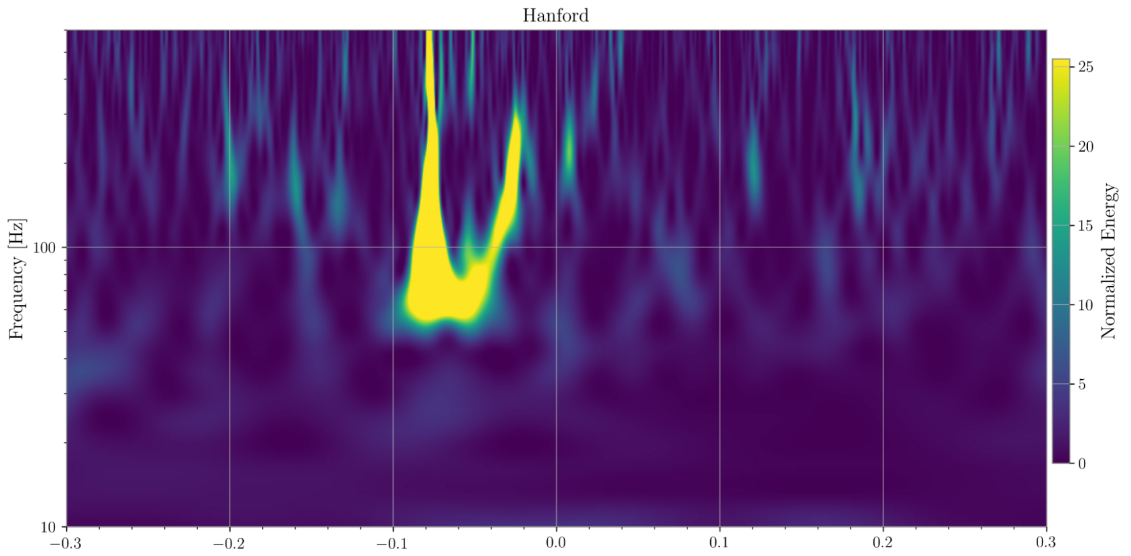

Figure 6.2: Spectrogram of a non-spinning BBH GW signal near a Blip glitch.

glitch classes observed in LIGO and Virgo data (see Figure 6.3):

1. Blip: Blip glitches are the simplest glitch-type as far as deglitching is concerned. They are approximately 10 ms long, their frequency band ranges from 20 to 1000 Hz, and they are typically one to a few cycles long. Their causal mechanism is a mystery. Studies such as [203] find some correlation with auxiliary or environmental detector channels, but these do not account for a majority of the glitches. In a time-frequency spectrogram, they have a tear-drop shape as shown in Figure 6.3. They have been observed in LLO, LHO, and Virgo.

2. Scattering: Scattered light or "Scattering" glitches occur due to the scattering of the light in the detector vacuum cavity. They can be 1 to a few seconds long, their frequency band ranges from 8 to 100 Hz, and they typically $\mathcal{O}(100)$ cycles long. They have a characteristic arch-like appearance in the time-frequency spectrogram as shown in Figure 6.3. There is usually one primary arch below 10 Hz and the rest of the arches are harmonics of this arch. Their origins are tied to the low-frequency motion of the test-mass mirrors. The higher harmonic arches resemble the inspiral part of BBH signals, particularly, low-mass ($< 20M_{\odot}$) BBH systems. They bias estimates such as the chirp mass, mass ratio, inclination, distance, etc.

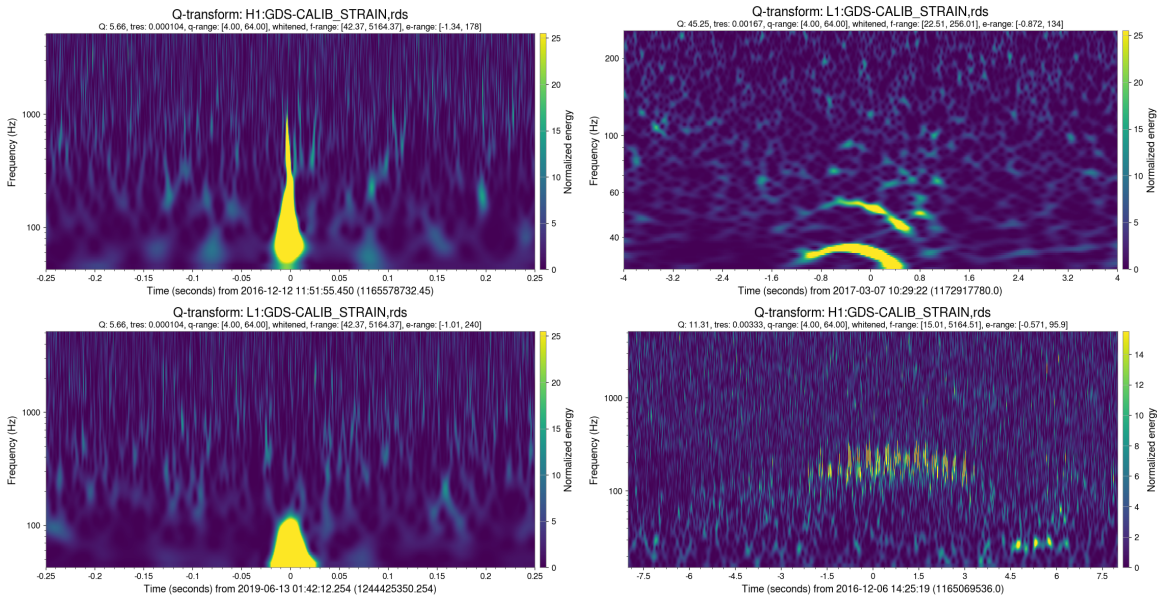

Figure 6.3: Time-frequency heat maps of various glitch classes discussed in section 6.4. Figure shows (in clockwise order from the top left) Blip, Scattering, Mountain, and Tomte glitches. Plots made using ligo-ldvw.

3. Tomte: Tomte glitches are similar to Blip glitches but are more spread out in duration (100 ms) and their frequency range is from 20 Hz to 256 Hz. Little is known about their origins but some correlations have been observed by gravity spy with adjustments of the electrostatic actuator circuits [204]. Similar to Blip glitches, they mimic the merger part of GWs emitted by high mass range systems and affect PE.

4. Mountain: Mountains are long-duration (>16 s) high frequency ($\gtrapprox$ 100 Hz) glitches, and are so named because of their appearance in the time-frequency plot (bottom right panel of Figure 6.3) They have been observed in LLO and LHO. Their origins are unknown but they hamper PE of long duration signals such as low mass BBHs or BNSs. For shorter duration signals, they are reconstructed by `BayesLine` as spectral lines in the PSD and merely reduce the signal SNR as opposed to biasing the source inference.

6.5 The `Signal+Glitch` model

The initial implementation of `BayesWave` contains separate signal and glitch models, which run in series, each with their own RJMCMC chain. The detector data was modeled as

$$\mathbf{s} = \mathbf{m} + \mathbf{n_G}, \tag{6.4}$$

where $\mathbf{n_G}$ is the stationary Gaussian detector noise, and $\mathbf{m}$ is the model waveform, either signal or glitch. Recall from section 3.7 that signal and glitch waveforms are both given by the summation of wavelets but the signal model projects a common set of wavelets onto the detector network ($\mathbf{m} = \mathbf{R} \star h$), where and h is obtained by summing over wavelets given by Equation 3.12, $\mathbf{R}$ is the detector response of the detectors to the GW signals (see Equation 2.16, Equation 2.17), while the glitch model uses independent wavelets for each detector ($\mathbf{m} = \mathbf{g}$), where $\mathbf{g}$ is given by the summation in Equation 3.12, one for each detector.

The independent signal and glitch models are useful in classifying candidate events as either astrophysical signals or transient glitches using the signal-to-noise Bayes Factor (Equation 3.5). For instance, it is used in works such as [205, 206] which describe the background distribution of high-amplitude events occurring in detectors that are categorized as candidate GW events by searches but are later found to be terrestrial glitches by `BayesWave`.

The `Signal+Glitch` model, as described in [45], simultaneously fits signal and glitch wavelets to the detector data:

$$\mathbf{s} = \mathbf{R} \star h + \mathbf{g} + \mathbf{n_G} \tag{6.5}$$

Due to the definition of the likelihood and the prior penalties we impose on the wavelet count and parameters, the signal wavelets reconstruct parts of the data that are coherent

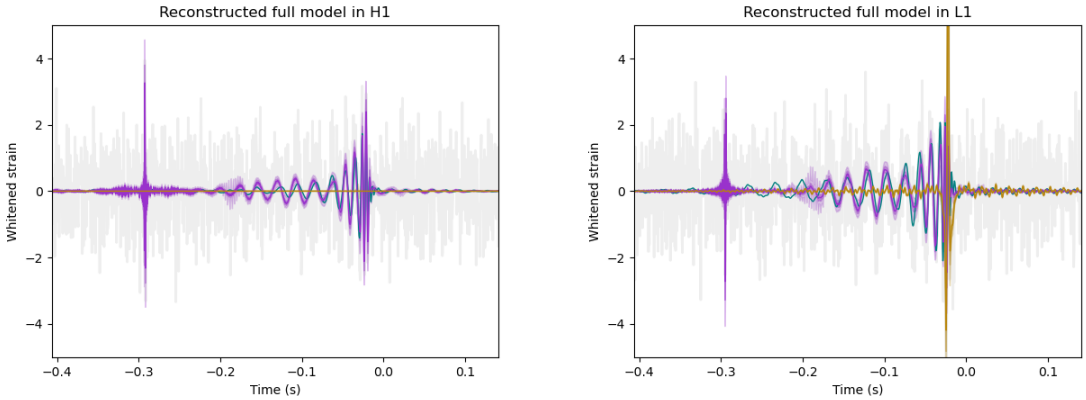

Figure 6.4: `BayesWave Signal+Glitch` analysis on GW150914-like injection near a Blip glitch in LIGO Livingston. The plot shows quantities in the LIGO Hanford (left) and LIGO Livingston (right) detector. The panels show the signal model (orchid), glitch model (gold), injection (teal), and the detector data (gray).

across detectors, while the glitch wavelets fit the incoherent power since they are independent for each detector. Figure 6.4 shows the time domain plot of a `BayesWave Signal+Glitch`model analysis on an injection of a non-spinning BBH whose masses are similar to GW150914. The injection is applied to real data containing a Blip glitch. The glitch is in the LLO data, while the LHO data is quiet. The glitch model (gold), reconstructs the glitch in the LHO data while the signal model (orchid), reconstructs the GW in both LHO and LLO.

There are possible cases where the signal and glitch model "cross" i.e., the signal model fits the glitch power and vice versa. This is usually due to a noise realization that causes the signal model to settle in a region of the sky such that the wavelets, though coherent, have a high SNR in just one detector. This is shown in Figure 6.5 where the signal model fits the Blip glitch in LHO and assumes a sky position where the same wavelets are much quieter in LLO, whereas the glitch model reconstructs part of the GW signal in the LLO data.

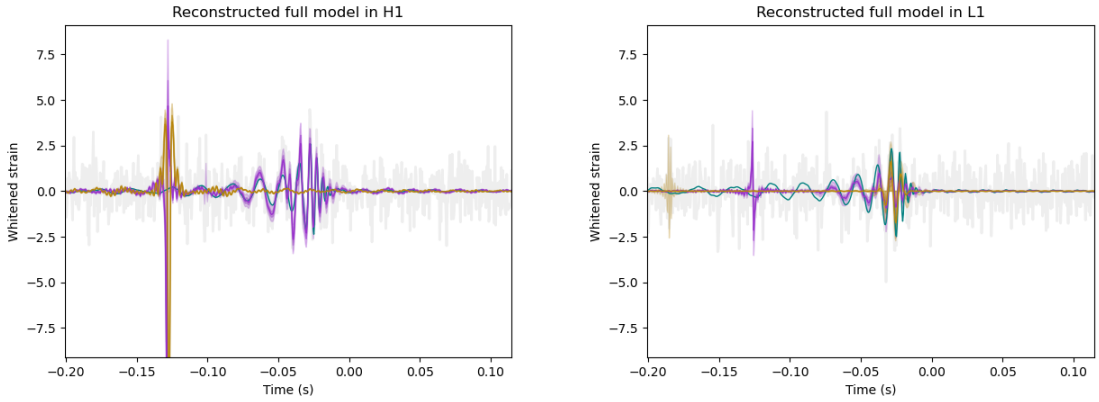

Figure 6.5: `BayesWave Signal+Glitch` analysis on GW150914-like injection near a Blip glitch in LIGO Hanford. Similar to Figure 6.4 but showing an unfavorable outcome of the signal model incorrectly reconstructing the glitch power in LIGO Hanford.

6.6 Improvements to the `Signal+Glitch` model

The deglitching effort presented in this thesis is aimed at building a set expanding the use of the `Signal+Glitch`model for future GW detections coincident with glitches. The `Signal+Glitch` model implementation described in [45] has the limitation that identical copies of the set of configurable priors to the intrinsic parameters of the wavelets, such as quality, SNR, dimension, etc., are applied to both the signal and glitch model. In other words, the package allows for priors on the models but does not provide the ability to use different sets for the signal and glitch wavelets, and is therefore only helpful in deglitching cases where the signal and glitch lengths are comparable. In the following section, I describe how I separate the two prior sets such that the models are tuned to the better-suited parts of the parameter space. This is to done to discourage the models from settling into "wrong" regions of the parameter space as shown in Figure 6.5. This work builds upon the initial changes implemented by Tyson Littenberg in the BayesWave C code to separate the prior sets.

6.6.1 Q priors

The quality factor (Q) is one of the parameters of a wavelet. It can be written in terms of the central frequency f_0 and damping time of the wavelet (tau) as $Q = 2\pi f_0 \tau$. Up to a constant, the quality factor is equal to the number of cycles in a wavelet. `BayesWave` is most sensitive to GW signals from BBH systems in the total mass range, $\mathrm{M}_T \gtrapprox 20 M_\odot$. These signals are typically shorter than a second and their frequency range goes from 20 Hz to 500 Hz. Consequently, the wavelets required to model these signals do not need quality factors greater than 40. However, longer glitch classes cases such as Scattering, and Whistle glitches need a larger number of cycles. I introduced run-time configuration options that allow for separate ranges of the quality factors for the signal and glitch part of the `Signal+Glitch` model.

6.6.2 Dimensionality priors

Recall that `BayesWave` is a trans-dimensional algorithm that can add or remove wavelets based on the increase to fit. The dimensionality prior places a limit on the number of wavelets that can be added by the waveform models. The default is 100 for both the signal and the glitch models. Similar to Q priors, I introduced run-time configuration options that allow for separate ranges on the number of wavelets for each of the two parts of the `Signal+Glitch` model. BBH signals can typically be reconstructed within 20 wavelets while longer glitches like Mountains require as many as 200 wavelets.

6.6.3 Window priors

BBH signals typically encountered in LIGO and Virgo are less than a second long. However, we use an analysis segment of a minimum of 4 seconds since frequency resolution is directly proportional to the length of the data, and crude resolution in frequency gives us poor estimates of the PSD and the waveform spectra. To limit the focus of `BayesWave` waveform models on the < 1 second of relevant data, they are restricted to fit wavelets in

a time window typically one-fourth as long as the analysis segment, centered around the trigger time. In the absence of this restriction, `BayesWave` reconstructs all features within the analysis segment that increase the likelihood, including artifacts of edge effects. This dilutes the attention that we require from `BayesWave` to focus on a particular subset of the analysis segment.

Previously, the time-window parameter was common to the signal and glitch parts of the `Signal+Glitch` model. However, to analyze cases where the characteristic durations of the GW signal and glitch are different, I introduced run-time options that allow independent placement of windows for the signal and glitch parts of the model.

6.7 Results of the deglitching process

In this section, I present the results of applying the `Signal+Glitch` model on GW injections applied to glitchy data. The injections are non-spinning BBH coalescence system with masses 36 $M_\odot$ and 29 $M_\odot$, similar to GW150914. The sky location, inclination, and distance are set such that the SNR is about 15, and we use the `IMRPhenomPv2` approximant to generate the waveform. The detector network consists of two detectors: LHO and LLO and we consider data where the data is glitchy in just one detector.

We also analyze the simulated observations with template-based PE using `Bilby` before and after deglitching and compare the performance and report the improvements.

6.7.1 Blips

Due to their relatively simple morphology, Blip glitches coincident with BBH signals can be reconstructed and deglitched with the default `BayesWave Signal+Glitch` model i.e., separate priors for the signal and glitch models are not required.

Figure 6.4 shows the time domain reconstruction of the signal and glitch models. We can see that the glitch power has been isolated by the glitch model. Figure 6.6 shows the spectrograms of the data before and after deglitching. The top panel shows the Blip as

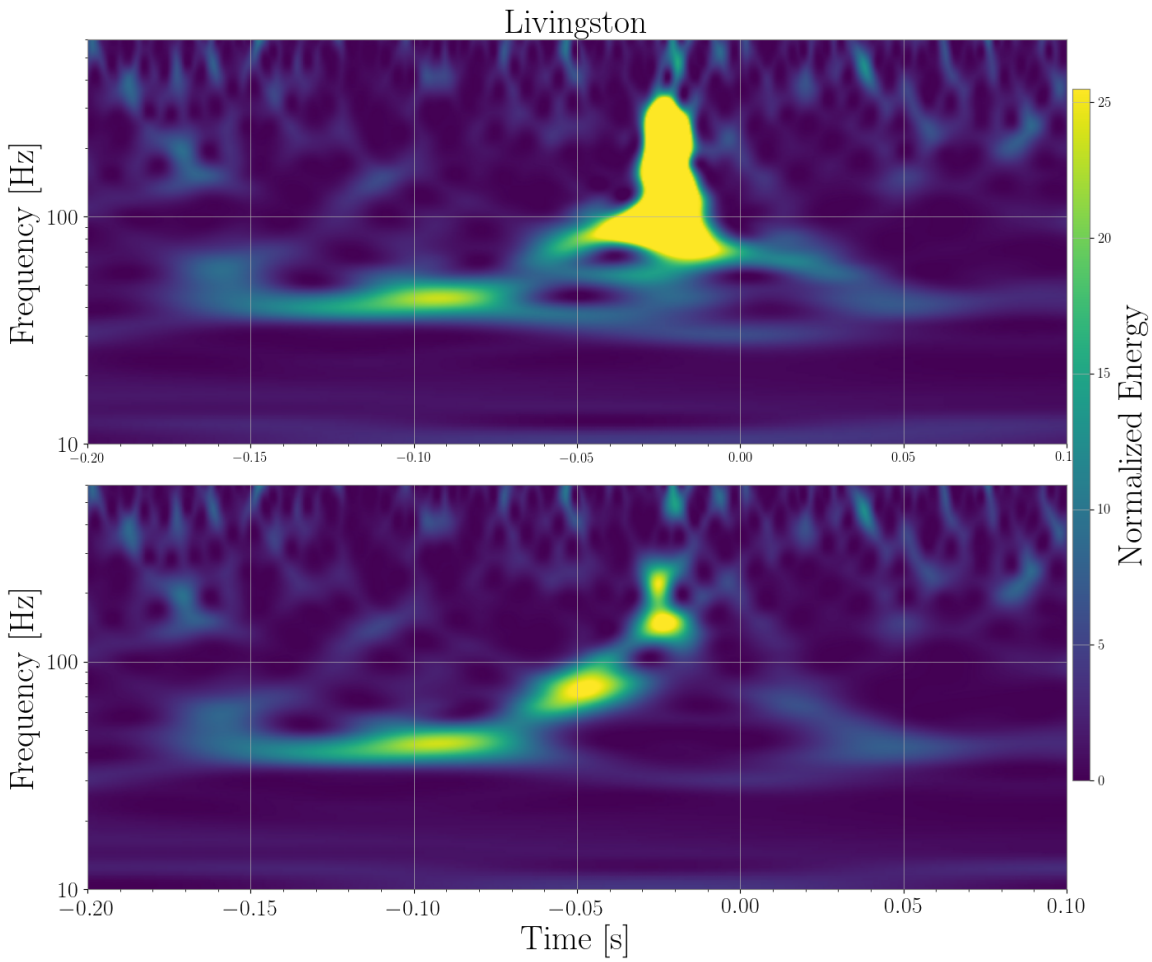

Figure 6.6: Time-frequency heat map depicting glitch cleaning for the Blip glitch. The top panel shows the LIGO Livingston data containing the Blip glitch plus the GW150914-like injection. The bottom panel shows the glitch-subtracted data with the GW150914-like injection.

asymmetric teardrop shape from -0.30 s to -0.05 s and the BBH signal as a chirp starting at the center of the glitch and increasing in frequency till about -0.02 seconds.

Figure 6.7 shows how the Blip biases the PE estimates of select parameters. Specifically, since the Blip occurs resembles the merger part of the signal, `Bilby` recovers an incorrect distribution of parameters that either exclude the true value at the 90% credible level or have multi-modal peaks that are not centered around the true value.

Once the glitch is subtracted from the data, the recovered parameter distributions include the true parameter values.

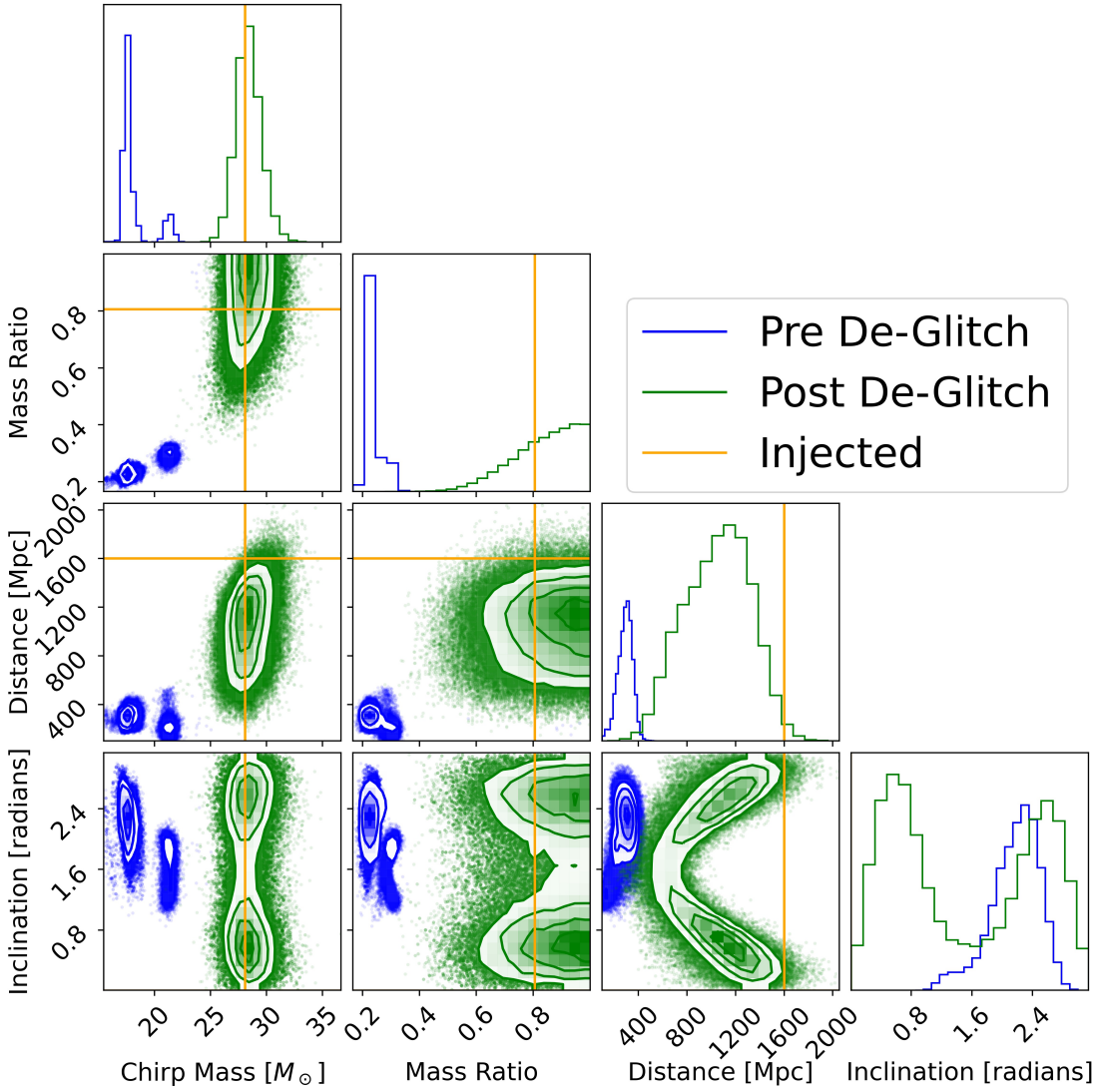

Figure 6.7: `Bilby` PE corner plot for the Blip glitch case. The plot shows a clear bias in the chirp mass ($\mathcal{M}$) and the mass ratio (q) pre deglitching (green) which is fixed after deglitching (blue).

6.7.2 Scattering

Figure 6.8 shows the `BayesWave` deglitching run where it reconstructs a Scattering glitch in LLO. The glitch is much longer in duration than the GW signal. Hence for this particular case, we use a different set of run configurations from the earlier Blip glitch case. I used a longer segment length of 8 seconds, instead of the usual 4 seconds. I also used the modified

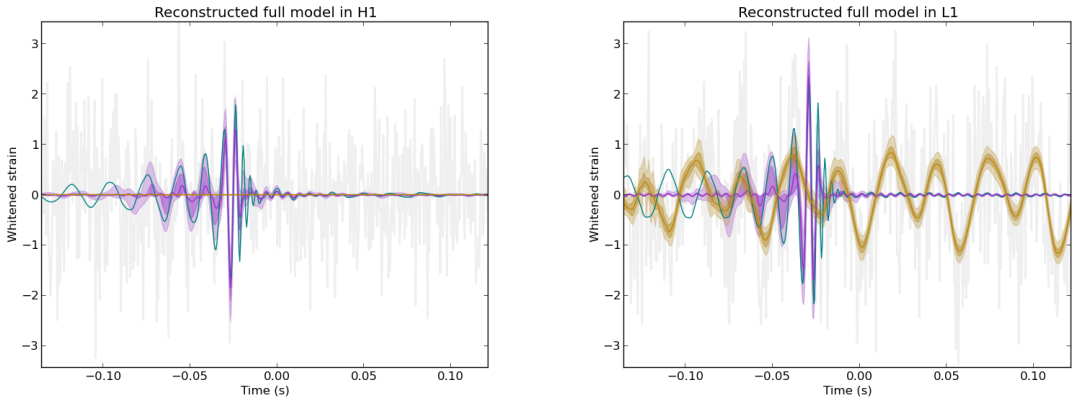

Figure 6.8: The analog of Figure 6.4 for the Scattering glitch. The glitch (reconstructed in gold) is in LIGO Livingston and is of a much longer timescale than the signal.

priors described in section 6.6. Specifically, I limit the maximum signal quality factor to 40 and set the maximum glitch quality factor to 160. I also set the glitch window to 2 seconds instead of the usual 1 second centered around the middle of the segment.

Figure 6.9 shows the spectrogram of the LLO data pre and post deglitching. The arches are evident in the top panel from -1.5 s to 0.5 s. The injected signal is the chirp-like, almost vertical series of pixels at around 0 s. The bottom panel shows just the BBH signal and the removal of a significant portion of the glitch, although some glitch power remains at the lower frequencies.

The PE results on Scattering glitches show mild biasing in the mass ratio (q), although the effect is not as profound as for the Blip case (Figure 6.10).

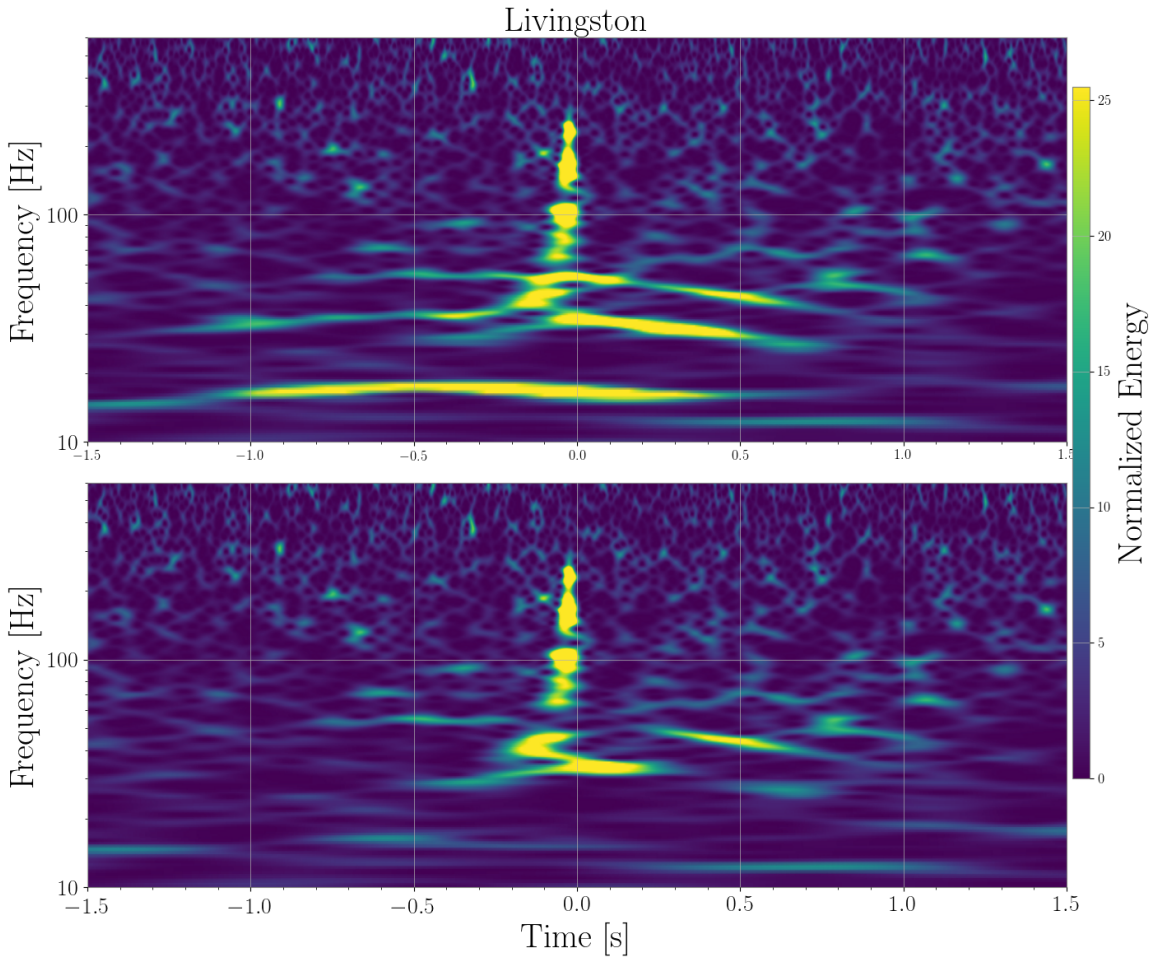

Figure 6.9: The analog of Figure 6.6 for the Scattering glitch. `BayesWave` can subtract most of the glitch power with some small left-over power at ~ 60 Hz.

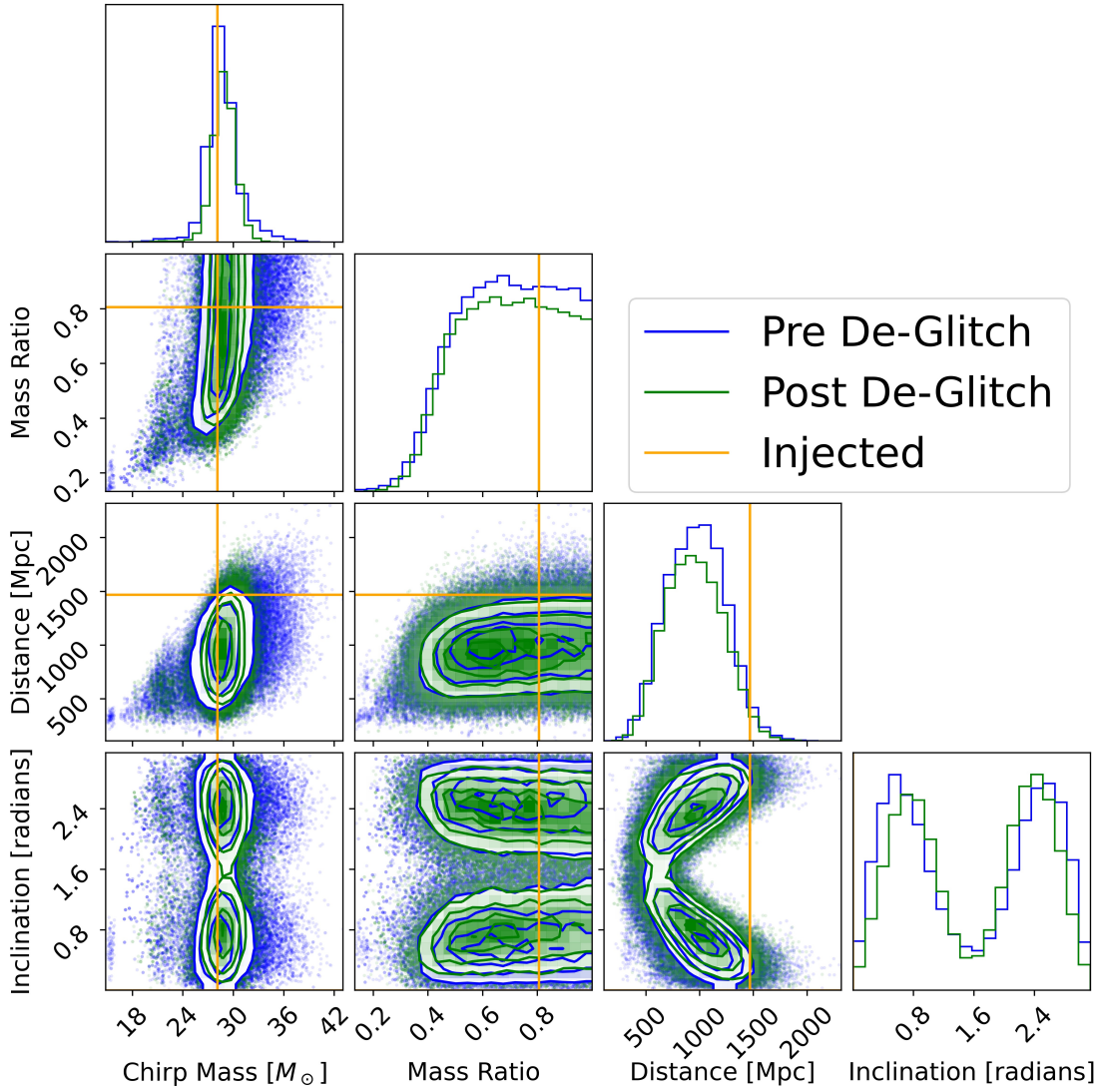

Figure 6.10: The analog of Figure 6.7 for the Scattering case. The plot shows mild biasing in the mass ratio which is fixed by the `BayesWave` deglitching.

6.7.3 Tomte

Figure 6.11 shows the deglitching process applied to the Tomte glitch in LLO. Similar to the Blip case, I used the default priors and use the standard `BayesWave` configuration to do the analysis. `BayesWave` separates the signal and glitch model. This is also seen in the spectrogram in Figure 6.12 where almost all of the glitch power is removed from the data.

The PE analysis reveals that Tomte glitches have a major impact on parameter distri-

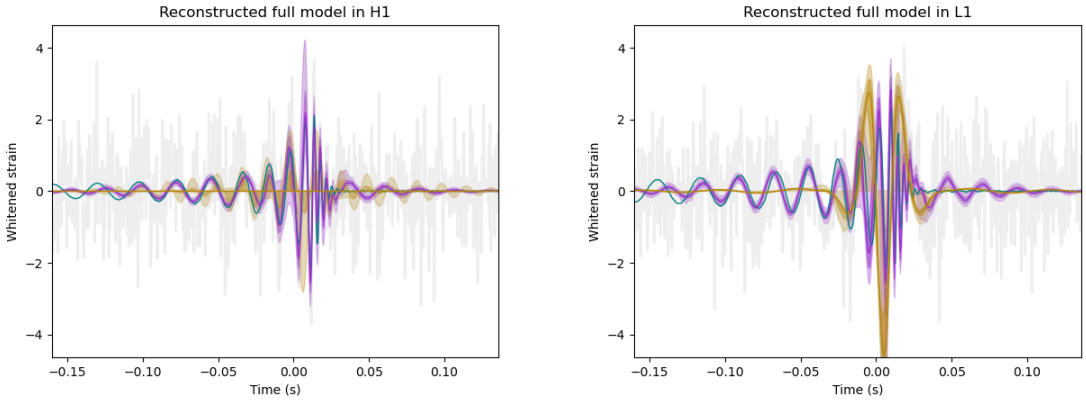

Figure 6.11: The analog of Figure 6.4 for the Tomte glitch. The glitch (reconstructed in gold) is in LIGO Livingston. The plot shows mild mixing of the signal and glitch models, but the glitch model reconstructs the majority of the Tomte glitch as shown in Figure 6.12.

butions as shown in Figure 6.13, while the deglitching process helps recover parameter distributions consistent with the true value.

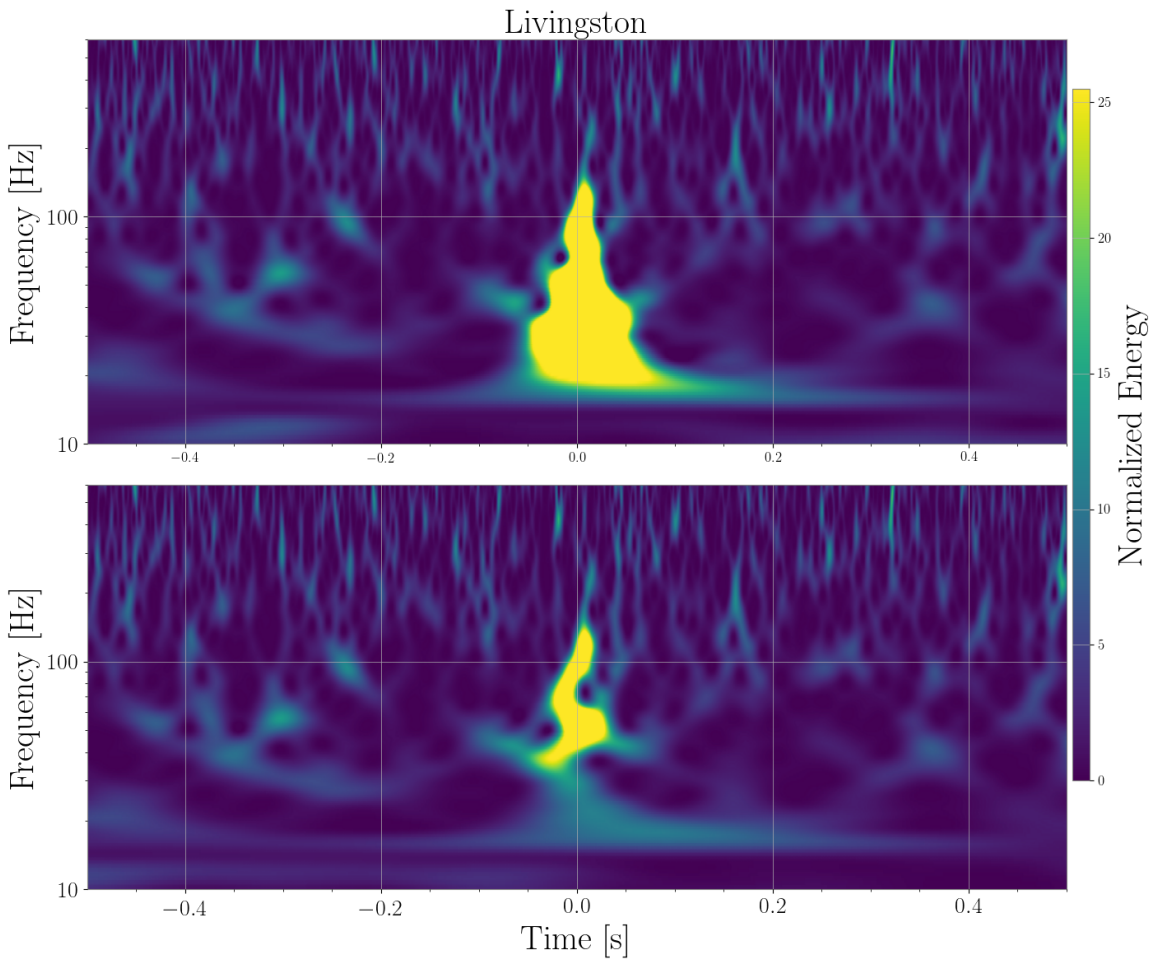

Figure 6.12: The analog of Figure 6.6 for the Tomte glitch. `BayesWave` is able to subtract most of the glitch power with some small left-over power at < 30 Hz.

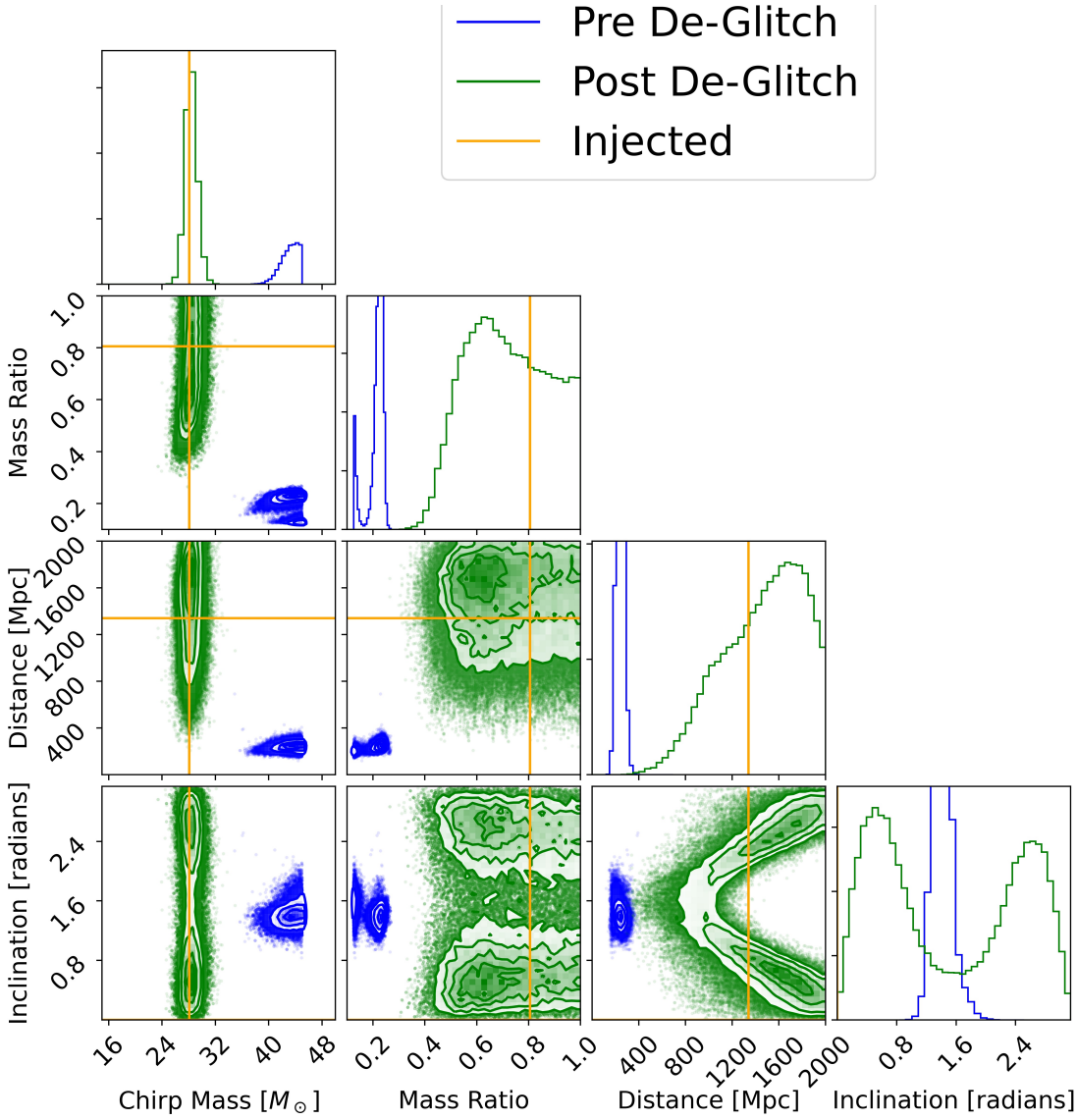

Figure 6.13: The analog of Figure 6.7 for the Tomte case. The plot strong bias in the chirp mass ($\mathcal{M}$) and the mass ratio (q) pre deglitching (green) which is fixed after deglitching (blue).

6.7.4 Mountain glitches

Due to the large time and frequency volume (sampling rate of 2048 Hz and duration of 32 seconds) required to reconstruct Mountain glitches, the run time of a `BayesWave` analysis can take up to weeks. Due to technical difficulties of running our analyses on the LIGO computing clusters, I could not complete the runs for Mountain glitches. Here, I present

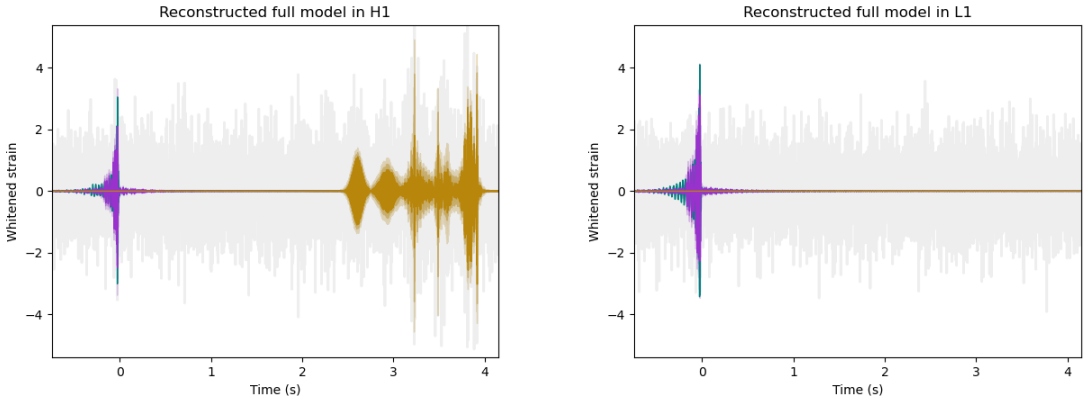

Figure 6.14: The analog of Figure 6.4 for the Mountain glitch. The glitch (reconstructed in gold) is in LIGO Hanford. The plot shows successful modeling of the signal and glitch powers by the respective models.

some preliminary results.

6.8 Conclusions

In this chapter, I extended the `BayesWave Signal+Glitch` model to accommodate wide-ranging signal and glitch morphologies by decoupling their priors. I also characterize the effects of frequently occurring LIGO and Virgo noise glitches on PE and show improvements due to the deglitching method. With changing detector sensitivity and characteristics, the relative frequency of occurrences of these glitch classes may change. Nevertheless, the flexibility of this method allows it to be applicable to, in principle, any new glitch, and signal morphology.

To make this process relatively automated, code development work is needed. The code should roughly characterize the glitch and signal features based on, for example, the spectrogram, to crudely determine the configuration required to launch a `BayesWave` deglitching job.

CHAPTER 7
SEARCHING FOR POST-MERGER GW SIGNALS FROM BNS COALESCENCES

In this chapter, we discuss methods to detect and characterize the post-merger signal from binary neutron star coalescences. Recall from chapter 2, the four possible remnant scenarios for BNS mergers are: instantaneous collapse into a BH, hyper massive NS (HMNS), supramassive NS (SMNS), a stable remnant NS [108]. The exact nature of the post-merger remnant of GW170817 is still unknown. No GW post-merger signal was detected in GW170817 [106, 107]. Various other works such as [207, 208, 209] have constrained the remnant mass to either the SMNS or HMNS categories using a GW or EM observations or a combination of both. However, the inferences are very method-dependent and there is no consensus amongst the broader astronomy community about whether the remnant was a black hole or a neutron star.

From the perspective of post-merger GW searches, various studies of the HMNS scenario have shown short-lived (< 1 s) emissions that peak in the $1 - 4$ kHz region as shown in Fig Figure 7.1 [12, 13, 14]. These are caused by transient non-axis symmetric deformations and quadrupolar deformations. The exact morphology of this signal is crucially dependent on the EOS. However, due to the complexity of the dynamics in the presence of matter, no analytical models give us accurate templates. Numerical simulations could take into account these complexities, but these are computationally expensive (run times of numerous weeks on 100s of cores), and it is difficult to account for an exhaustive list of possibilities since the number of EOS models are in-principle, infinite. `BayesWave` allows us to search for unmodeled features without the need of modeling them apriori.

Since the remnant NS is expected to be more massive and its core denser than that of either of the component masses, the post-merger signal allows us to learn properties of EOS

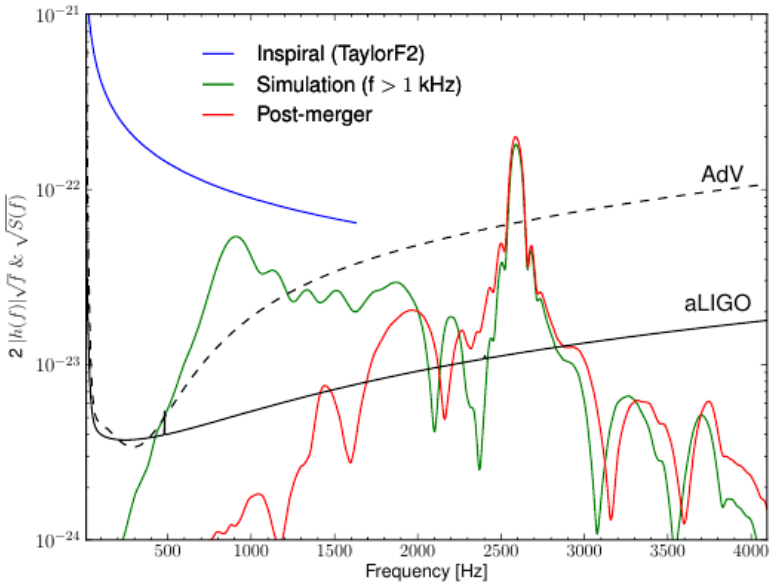

Figure 7.1: Amplitude spectra of the post-merger waveform from the coalescence of two non-spinning NSs with masses $1.35M_{\odot}$ at a separation of 20 Mpc oriented optimally and using the DD2 EOS [210, 211]. The plot shows the spectrum of the post-Newtonian approximation (blue), the full simulation (green), the post-merger part alone of the simulation (red), and the Advanced LIGO and Virgo sensitivities (black solid and dashed curves). Figure from [46]

in regions of the parameter space that is not possible from the inspiral phase [109, 110]. Chatziioannou et al [46] use the `BayesWave` waveform to place constraints on physical quantities such as the peak frequency f_{peak}, radius of the remnant, energy emitted in the post merger GW burst and the amplitude of the strain. Their study used BNS simulated waveforms from [212, 213, 214, 215] for three EOS models: NL3 for stiff [210, 216], DD2 for moderate [210, 211] and SFHO for soft [217]. The waveforms were injected into simulated noise at the Advanced LIGO and Advanced Virgo design sensitivities [3, 6].

Peak frequency

A discussed in as [12, 13, 14] the short lived remnant NS emits GW radiation that peaks in the $1-4$ kHz frequency range. The exact value of the peak frequency f_{peak} is dicatated by the EOS. The f_{peak} measurement can be done by directly computing the peak frequency of the signal spectrum offered by `BayesWave`. `BayesWave` outputs a posterior sample of

waveforms, by finding the $f_{\rm peak}$ values for these samples, we can on the signal reconstruction into posteriors on $\rm f_{peak}$.

Radius

[46] and [212] observed a correlation between $\rm f_{peak}$ and the radius of a $1.6M_\odot$ NS ($\rm R_{1.6}$) formed from the merger of two non-spinning NSs of mass $1.35M_\odot$ each which is independent of the EOS. Using this correlation and the posteriors on $\rm f_{peak}$ we can find the posteriors on $\rm R_{1.6}$ which can then help directly place constraints on the EOS.

Energy and Amplitude

The posteriors of the signal reconstruction offer constraints on the waveform amplitude spectrum. This amplitude spectrum along with physical parameters of the source such as the distance, sky location, orientation, obtained from the pre-merger analysis, can be used to measure the energy emitted in the post-merger GW.

$$\frac{\mathrm{d}E_{\rm GW}}{\mathrm{d}f} = \frac{4}{5}\pi^2 D^2 f^2 |\widetilde{h}_\iota(f)|^2. \tag{7.1}$$

where D is the luminosity distance to the source, f is the frequency, and $|\widetilde{h}_\iota(f)|$ is the amplitude spectrum of the incident signal from a BNS with an orbital plane that is oriented at angle ι with respect to the line of sight.

The methods presented in this section were used in placing upper limits on the amplitude and energy spectra of the GW170817 post-merger waveform [106, 107].

7.1 S190425z

I applied the same methods applied to the GW170817 post-merger analysis [106] to GW190425z [218]. GW190425z was a relatively distant BNS event and we found no evidence of a statistically significant signal, with a (natural) log Bayes factor of 0.41 ± 1.13 in favor of

stationary Gaussian noise compared to the signal model. Following [106], I obtained 90% credible upper limits on the strain amplitude spectral density and the energy spectral density of 1.1 x 10^{-22} $Hz^{-1/2}$ and $0.11 M_{\odot} c^2$ Hz^{-1} for a frequency of 2.5 kHz. (See Figure 7.2)

7.2 Characterizing post-merger detection performance of `BayesWave` and `Bilby`

In Easter et al., [47] we performed a bench-marking and comparison study of two waveform reconstruction methods: `BayesWave` and `Bilby` [154] in which the latter an ad-hoc phenomenological template-based approach. Unlike `BayesWave`, which uses a variable number of wavelets as per need, the `Bilby` waveform is fixed dimensional and is described by three exponentially damped sinusoids with a linear frequency drift (similar to chirplets). Each sinusoid is given by:

$$h_{j,+}(\vec{\theta}, t) = H w_j \exp\left[\frac{-t}{T_j}\right] \cos 2\pi f_j t(1 + \alpha_j t) + \psi_j, \tag{7.2}$$

where $\vec{\theta} = \{H, w_, T_j, f_j, \alpha_j, \psi_j\}$, $j = \{0, 1, 2\}$, H is the amplitude scaling factor, w_j is the relative scaling factor such that $\sum_{j=1}^{3} w_j = 1$. f_j is the central frequency of the sinusoid, T_j is the damping time, α_j is the frequency drift term and ψ_j is the initial phase. The subscript + on the left hand side denotes the plus polarization. The cross polarization ($h_{j,\times}$) is obtained by applying a phase shift of $\pi/2$ to $h_{j,+}$. The strain is given by

$$h(\vec{\theta}, t) = \sum_{j=0}^{2} h_{j,+}(\vec{\theta}, t) - h_{j,\times}(\vec{\theta}, t) \tag{7.3}$$

Note that this model differs from the chirplet model in two important respects: (i) the damping exponential is linear, and not the square of time, and (ii) the dimensionality of the model is fixed.

We performed injections into simulated observations with network SNR varying from 1 to 50 using the Advanced LIGO [3] and Advanced Virgo sensitivities [6]. Easter did injections of various equation of state models and found that the `Bilby` model can confidently

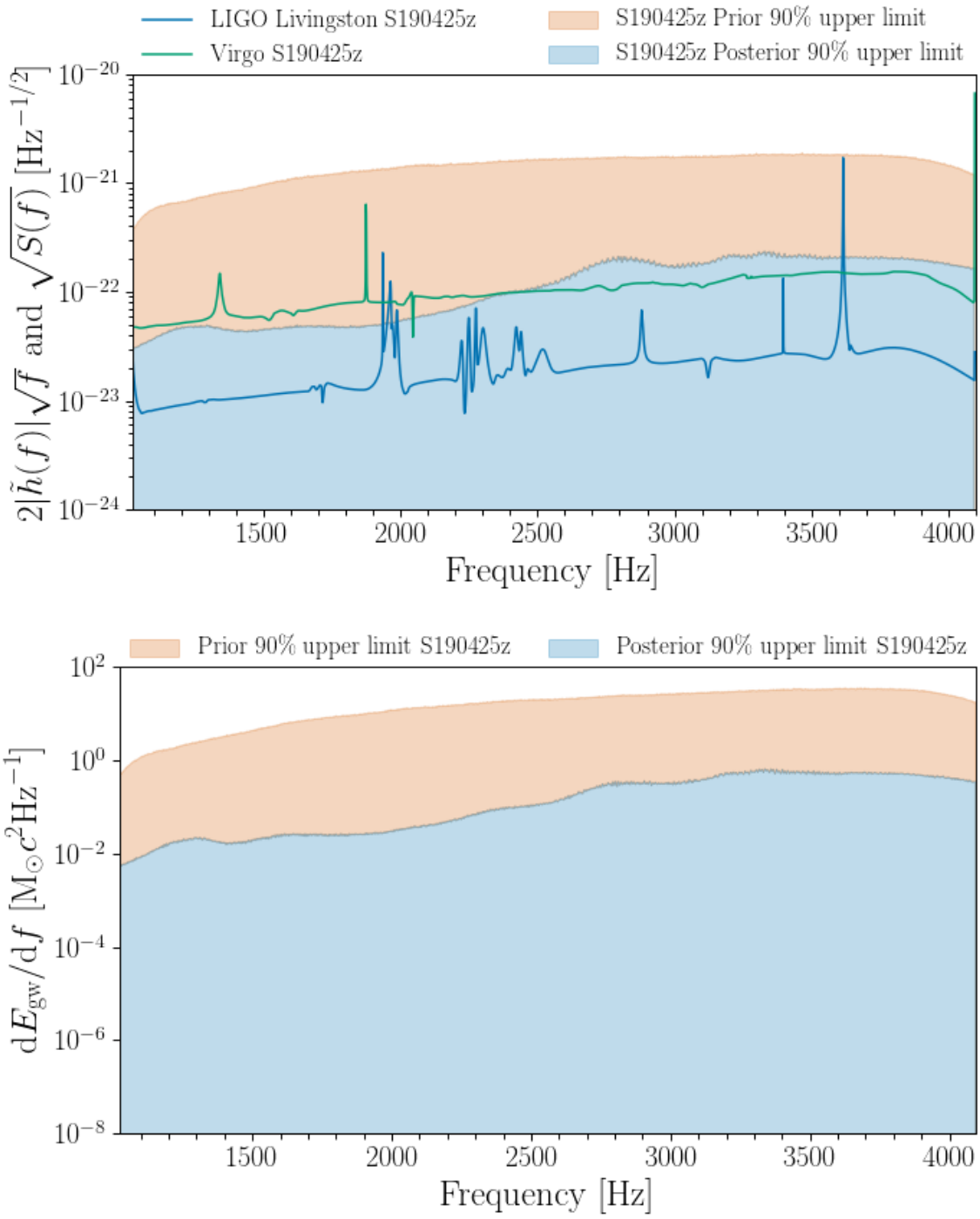

Figure 7.2: Upper limits on the strain amplitude (top), and the total radiated energy spectrum (bottom). The energy spectrum is calculated using Equation 7.1 by combining the distance and inclination angle posterior samples from the inspiral PE analysis with the strain amplitude upper limits from the `BayesWave` analysis. The orange areas show the prior while the blue areas are the inferred posterior. The top panel also shows the ASDs of LIGO Livingston (green) and Virgo (blue) for comparison. Figure from [218].

report post-merger detections of SNR > 7 with a signal to noise Bayes Factor threshold of 3000. The `Bilby` model was also able to constrain the frequency of the peak emission ($f_{\rm peak}$) to within a percent for SNR > 15.

I performed the analysis with `BayesWave` for one particular equation of state: SLy-M1.350-Λ390 [219] which we select due to the compatibility of the tidal parameters inferred from GW170817 [106, 107]. We found that compared to the ad-hoc model described above, `BayesWave` can obtain better constraints on $f_{\rm peak}$ for SNRs lower than 15 as shown in Figure 7.3. This is expected due to the inherent flexibility in the number of dimensions that `BayesWave` provides. All in all, this study successfully added a new method in our toolbox to detect post-merger BNS signals when we arrive at higher sensitivities. Further details can be found in [47].

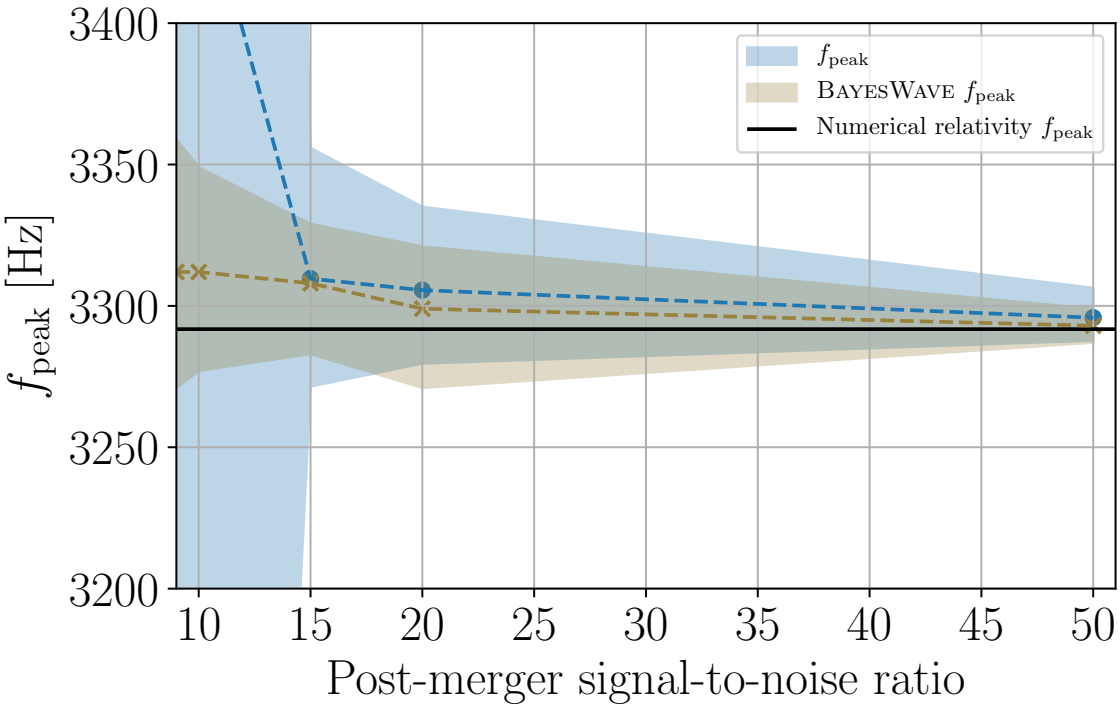

Figure 7.3: Comparison of f_{peak} recovery by `BayesWave` (beige) and `Bilby` (blue) as a function of the post-merger SNR. The plot shows that `BayesWave` is able reconstruct the f_{peak} posteriors faithfully at post-merger SNR > 10, while the posterior from `Bilby` is wider at lower SNRs due to the rigidity of the model. Figure from [47].

7.3 Stacking Observations

Past works such as [136, 220] explore the possibility of detecting a post-merger GW signal by taking into factors such as account detector sensitivities, estimates of BNS populations, estimates of signal spectra using various EOS models. Yang et al's result [220] seem to indicate that we may not have a good chance of detecting a post-merger GW signal with current LIGO/Virgo detectors or even with future ground-based detectors with much better sensitivities such as Einstein Telescope, Cosmic Explorer. Torres-Rivas et al's [136] results indicate sensitivities 2-3 times better than Advanced LIGO design sensitivity would put us in a position to extract dominant frequency components from BNS events similar to GW170817.

Hence, there is a need to be able to *stack* results from multiple observations to improve detection probability. Kalmus et al [221] first approached this in the gravitational wave context, for a related source: the repeated bursts of GW emission which may occur during flaring activity in Soft gamma-repeaters (believed to be magnetars undergoing violent reconfigurations of incredibly intense and twisted magnetic fields). They combined multiple observations by stacking the time frequency tiles of the data near soft GRBs. They proposed two methods of stacking the time-frequency tiles from multiple events and then feeding them to a burst search pipeline. Other methods include stacking the posterior probabilities for quantities such as $R_{1.6}$, f_{peak}, or stacking evidences for various models.

7.3.1 Stacking evidences

To stack multiple non-detections, we need a statistic that could be assigned to a set using estimates from the individual analyses. The primary statistic we use to determine post-merger detection is the signal-to-noise Bayes factor, i.e., the ratio of the evidences of the two models. The evidence is calculated using Equation 3.4. Up to a normalizing factor, evidence is a probability estimate for a model. Given multiple independent non-detections,

it stands to reason that multiplying these quantities should result in combined evidence.

We begin with this principle. Given a signal model M_s, the evidence for the i$^{\text{th}}$ detection is given by

$$p(\mathbf{d}_i|M_s) = \int p(\mathbf{h}_i|M_s)p(\mathbf{d}_i|\mathbf{h}_i, M_s)d\mathbf{h}_i \tag{7.4}$$

where $\mathbf{d}_i$ and $\mathbf{h}_i$ are respectively the data and signal waveform for the i$^{\text{th}}$ detection.

The joint-evidence for N post-merger candidates is then the product of all the $p(\mathbf{d}_i|M_s)$

$$p(\mathbf{d}_1, \mathbf{d}_2, .., \mathbf{d}_N|M_s) = \prod_{i=1}^{N} p(\mathbf{d}_i|M_s) \tag{7.5}$$

which reduces to

$$p(\mathbf{d}_1, \mathbf{d}_2, .., \mathbf{d}_N|M_s) = \int .. \int \prod_{i=1}^{N} p(\mathbf{h}_i|Ms) \prod_{i=1}^{N} p(\mathbf{d}_i|\mathbf{h}_i, M_s) \prod_{i=1}^{N} d\mathbf{h}_i \tag{7.6}$$

The issue, however, is that these, in reality, are not independent probabilities. The first product term under the integrand on the right-hand side is the prior on the signal model. This prior is common for all observations, and as such, Equation 7.6 over-counts the prior in its estimate. We need to develop a procedure such that $p(\mathbf{h}_1, \mathbf{h}_2, ..\mathbf{h}_N)$ does not over-count this information.

This is still work-in-progress and is left as a future project.

7.3.2 Stacking time-frequency tiles

We implement a variation of the method outlined in Kalmus et al., where we stack the time-frequency tiles of individual observations by aligning them by the coalescence time. The assumption here is that there is one true NS equation of state which will imprint itself on a BNS post-merger. Given the fact that neutron star masses lie in a narrow range of masses (1.2 $M_\odot$ to 2.1 $M_\odot$, the post-merger signal across observations would be similar in morphology. Additionally, since time-frequency tiles stacking is a stacking of power, not amplitude, there is no chance of interference. The noise across detections would "even

out" leaving a bright spot of tiles showing the tiles of combined signals. This stacked set of time-frequency tiles would then be analyzed by higher-energy cluster-finding algorithms such as Omicron [222].

We test this method using injections of a NR simulation by Baueswein et al which assumes as DD2 EOS [215] using component masses (m_1, m_2) = $(1.37M_\odot, 1.37M_\odot)$. We perform the 100 injections with uniformly varying sky location and orientation parameters into simulated noise with A+ sensitivity. We perform three such sets of simulations with luminosity distances (D_L) set to 20 Mpc, 40 Mpc (), and 80 Mpc. Note that the GW170817 event was from a BNS pair at approximately 40 Mpc from the earth. The post-merger signal for this waveform peaks at ≈ 2.5 kHz. as shown in Figure 7.4 which shows the injected signal (teal) and the recovered `BayesWave` waveform (orchid curves).

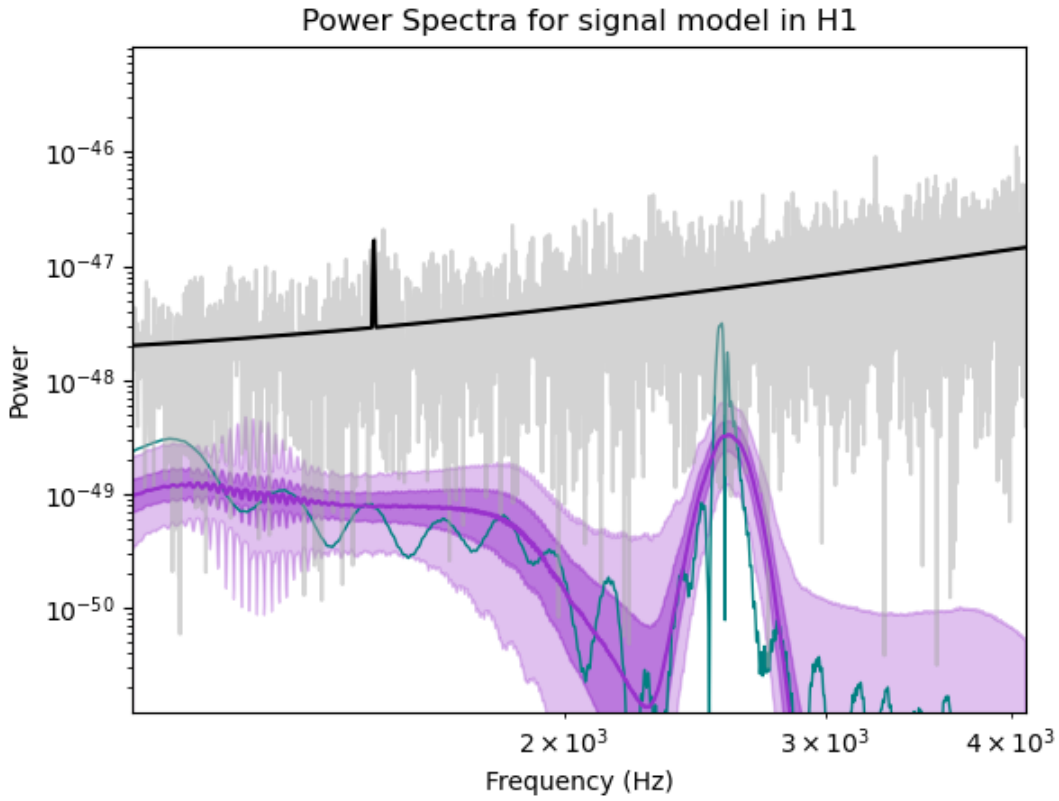

Figure 7.4: `BayesWave` signal waveform spectrum on an injection of the DD2 waveform [215] with $(m_1, m_2) = (1.37M_\odot, 1.37M_\odot)$ placed at 20 Mpc. The plot shows the injection (teal) which sharply peaks at ≈ 2.5 kHz, the `BayesWave` median (orchid) and credible intervals, simulated LIGO Hanford detector data (gray) and the detector PSD.

We show in the result of stacking 1, 3 and 10 time-frequency tiles for each of the three distances in Figure 7.5. For the D_L=20 Mpc case, we can see that stacking the tiles gives shows a bright set of pixels at 2.5 kHz starting at 3 stackings and this becomes pronounced at 10 stackings. In the D_L=40 Mpc case, this effect is less evident at three stackings but a bright spot can be seen in the right-most figure where 10 injections are stacked. For the D_L=80 Mpc case, stacking does not seem to show any visible effect.

7.4 Conclusions

In this chapter, I discussed the methods and results of searching for post-merger GWs from BNS mergers. We did not detect any post-merger counterparts in the LIGO and Virgo BNS

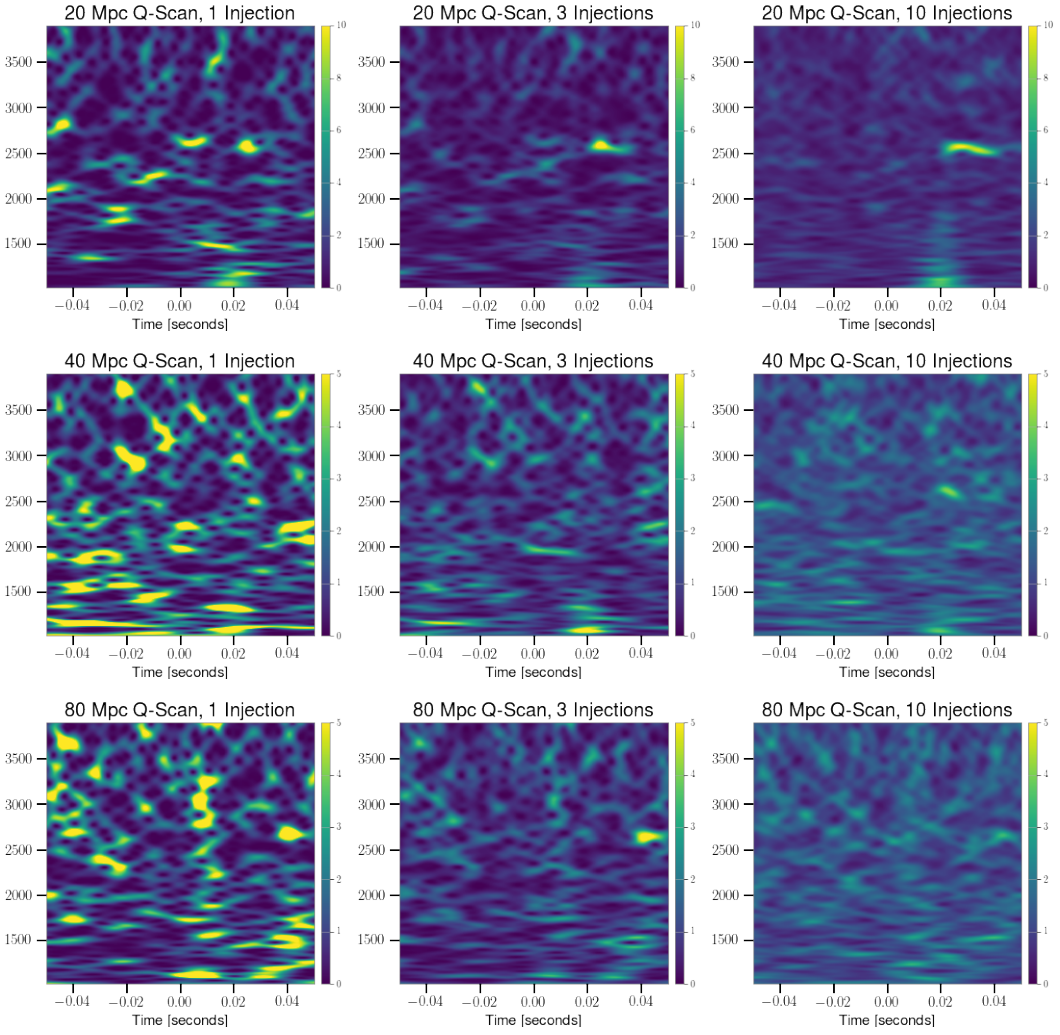

Figure 7.5: Results of stacking the time-frequency spectrograms of the whitened LIGO Livingston data containing the DD2 [215] injections at 20 Mpc (top), 40 Mpc (middle), and 80 Mpc (bottom). The left, center, and right columns respectively show the result of stacking 1, 3, and 10 time-frequency maps.

events GW170817 and GW190425, but the amplitude and energy upper limits allowed provided sensitivity improvements required to be able to detect these signals. I discussed two potential methods of "stacking" multiple observations which would allow the detection confidence to accumulate: evidence stacking, and time-frequency tile stacking.

Future methods include coherently adding data of multiple detectors for a given BNS event before performing the time-frequency stacking.

CHAPTER 8
CONCLUSIONS AND OUTLOOK

With 90 GW event detections so far, the field of GW astronomy has become mainstream. The astrophysical interpretation was made possible by sophisticated modeling of both source and detector noise. In this thesis, I developed and applied methods based on a model-independent approach to check for biases due to un-modeled astrophysical or terrestrial effects. `BayesWave` is a wavelet-based algorithm that is sensitive to a wide range of signal and glitch morphologies. We leveraged this flexibility to improve both detection confidence and data quality.

In chapter 2 I gave a brief history of GR and discussed some of its predictions including GWs, their theoretical foundations, and detectable effects. Next, I described how GWs be detected in laser interferometric detectors such as LIGO, Virgo, KAGRA, and other future-generation detectors. I then listed the various sources of GWs that are predicted by the literature and narrowed our focus to the most promising sources as of yet: compact binary coalescences. Finally, I reviewed the developments that led to reconstructing GW signal waveforms, including template-based and model-independent wavelet-based methods.

In chapter 3 I discussed in detail the mathematical and statistical tools used in inferring the properties of the source from detector data. I began by describing how Bayesian statistics are applied within the context of GW source inference. Specifically, I introduced how quantities such as the likelihood, prior, posterior, and evidence, can contribute to making quantitative statements about the properties of the signal and its source. I showed how these quantities are calculated by matching the data with signal reconstructions given by waveform models by applying signal processing concepts. I then gave an overview of the various physical parameters of the source, such as the masses, spins, and extrinsic angles that affect the GW waveform. Next, I described how GWs can be expressed as a summa-

tion of spin-weighed spherical harmonic modes, and how detecting non-dominant modes can help in improving source inference. I explained the challenges in sampling multi-dimensional parameter spaces and clever solutions to tackling the problem with stochastic Monte-Carlo-based samplers such as MCMC and nested sampling. I introduced sampling algorithm software packages such as `LALInference`, `Bilby` and `RIFT` that are used in offline parameter estimation analysis. I then described the details of the wavelet-based `BayesWave` algorithm and gave an overview of its various use cases as have been applied in this thesis.

In chapter 4 I described how various template models, or approximants, capture physical complexities such as spins, precession, and higher-order spherical harmonic modes. I stated the importance of model-independent tests of the signal waveforms inferred using these templates and dove into the technical details of the signal waveform consistency test. I described how to quantify the agreement between a pair of signal waveforms via the overlap, and how the overlap between the `BayesWave` and template waveform varies as a function of the SNR and total mass (M_T) of the binary. I also described a signal consistency to compare detection overlap values with a background distribution simulated observations. The output of the test is a p-value estimate of the null hypothesis that the model reconstructions are consistent with background expectations. I showed how reconstruction comparisons can be used to characterize the higher order mode content in two specific GW events: GW170729 and GW190412 which had a high probability of containing higher order mode signatures. Lastly, I discussed a novel use of model-independent reconstructions to infer the spin of the remnant of a BBH merger without the use of GR templates.

Continuing on the tests of source inference, I described the standard tests of GR in chapter 5. I listed the various methods that are used to quantify departures from GR, and how they are related to one another. In particular, I described the residuals test, where we subtract the best-fit template waveform obtained from the data and compare the results

with surrounding detector noise. I then reported the results of the residuals test applied to LIGO and Virgo GW observations and calculated the p-values for the null hypothesis that detections are consistent with noise. Finally, I applied the residuals test and the signal waveform consistency test to simulated observations of non-GR waveforms. I found that that the residuals test is sensitive to only the strongest deviations from GR which cause the signal morphology to be significantly different from a GR CBC waveform. It is not sensitive to weaker deviations in which GR-templates can reconstruct the majority of the SNR. On the other hand, I found that the signal consistency test is a promising method for detecting medium to strong GR deviations in short (< 1 second) GW signals.

In chapter 6 I addressed the problem of transient noise events, called *glitches*, and how they negatively impact source inference. I discussed past events where astrophysical signals were coincident with a glitch, and how the `BayesWave Signal+Glitch` model was used to "clean" the detector data. I built upon that work and extended the `Signal+Glitch` model to accommodate glitch classes with varying durations and frequencies. I showed the performance of the glitch-cleaning done by `BayesWave` on a simulated set of GW signals added to detector glitches. I studied the effect of the glitch-cleaning on source inference by running PE on both the pre and post-glitch-cleaned detector data and looking at the improvement. Finally, I pointed to future work to automate the process of glitch cleaning by having a suite of software packages pull information about GW detections that need glitch cleaning, having them set the appropriate configurations based on glitch-type, before deploying `BayesWave` jobs to perform the task of deglitching.

Finally, in chapter 7 I described the theoretical background of post-merger GW signals from BNS coalescences and the prospect of detecting them using `BayesWave`. I discussed the results of applying the analysis to the two LIGO and Virgo BNS observations GW170817 and GW190425. We did not detect a post-merger signal, but the upper limits provided sensitivity improvements required to be able to detect one. I also reported results from a simulation study to characterize the reconstruction performance of `BayesWave` on

loud post-merger signals. I then briefly discussed two methods of stacking multiple post-merger non-detections to gain quantitative insight that isn't possible from individual BNS observations.

The work presented in this thesis strengthens the validity of our observations and shows ways to tackle possible outliers. `BayesWave` is a powerful algorithm that lets us accomplish a wide range of tasks. As we march toward a promising future filled with potentially thousands of GW detections, and thousands of more noise sources, model-independent methods will help tackle any surprises the universe, and the detectors have in store for us.

Appendices

APPENDIX A
CODE INFRASTRUCTURE FOR DOING RECONSTRUCTION COMPARISONS AND RESIDUALS ANALYSIS

A.1 Initial (manual) deployment of workflows

LIGO and Virgo detected their first 3 GW observations in 2015 during O1. By the end of O2, there were a total of 11 detections and I was responsible for the reconstruction and residuals analysis for the first GW transient catalog (GWTC-1). The scientific product of the residuals analysis was a set of p-values obtained by comparing the onsource SNR with the offsource background. The signal consistency test analyses presented in the detection papers till that point only showed visual comparisons of the wavelet and template reconstructions. It did not have an offsource component.

I manually deployed individual `BayesWave` analyes using the `bayeswave_pipe` software package that generated sequential workflows. There were a series of pre-processing steps such as gathering the input PE samples, setting up the run configurations, gathering the PSDs etc., and a series of post-processing steps such as running scripts to compute the overlap, or the residual SNR etc., which were repetitive for all the events. At the time, I performed these series of steps manually since the number of events was manageable.

In O3a, we had 39 total detections out of which 24 were used in both the analyses. Visually depicting 24 waveform comparison plots for the signal consistency was not feasible. I had by that time, developed the procedure described in section 4.4 and published it in [43]. This procedure also used injections into the background and also gave us a set of p-values. During the analysis stage of GWTC-2, two things were clear:

1. The signal consistency test and residuals analysis had a very similar structure. Every event had one onsource run and a large number of background runs.

2. Deploying the workflows "by hand" was no longer feasible due to the sheer number of events. We needed an software library that could ingest a set of inputs and automatically deploy the the whole workflow for every event.

However, due to time constraints, it was not possible to develop this library at that time. After the GWTC-2 was published, in anticipation of a large number of events from O3b which would be part of GWTC-3, I developed two libraries, `igwn-wave-compare` and `igwn-wave-compare-pipe`. The "igwn" here is to signify lower-case of the the International Gravitational-Wave Network (IGWN) [223]; "wave-compare" is to signify that it deals with waveforms and comparisons, and the "pipe" is to signify that it's a workflow deployment package. `igwn-wave-compare` contains python scripts and libraries that do the scientific calculations and plotting i.e., computing overlaps, residuals, SNRs, making plots similar to Figure 4.1 etc. `igwn-wave-compare-pipe` handles the automation side of things i.e., generating background times, setting up run configurations, and deploying the workflows on the condor [224], the job management software used by LIGO. It has been developed on a fork of the `bayeswave_pipe` code and is deployed using the `iwc_pipe` script.

`iwc_pipe` allows the deployment of the following workflows using command line flags to enable them which we list below. We also note that the scripts listed in brackets in the items are from the `igwn-wave-compare` library.

1. Onsource reconstruction: this runs a `BayesWave` workflow on the onsource data, generates time-domain template waveforms (script: `reclal.py`) from PE samples given by any of `LALInference`, `Bilby`, or `RIFT`, and compares the template and `BayesWave` reconstructions (script: `bw_li_inj.py`).

2. Onsource residual: this generates the residual data (script: `residuals.py`), and deploys a `BayesWave` workflow on the residual data.

3. Offsource injections: this takes random draws from the PE samples, selects analyze-

able random times (details below) around the event time, runs up `BayesWave` runs on these injections, and computes the overlap between `BayesWave` and injected waveforms (script: `bw_li_inj.py`).

4. Offsource background: selects analyzeable random times (details below) around the event time, runs `BayesWave` on these background times.

In the above four options, (1) and (3) are parts of the signal consistency test. If both these flags are enabled, the worflow compares the onsource overlap with the off-source overlaps, and calculates the p-values and generates useful histogram plots (script: `catalog.py`). Similarly, (2) and (4) are parts of the residuals analysis. When both these flags are enabled, the workflow comapres the onsource SNR with the offsource SNRs and calculates the p-values and generates histogram plots: (script: `testgr.py`). Figure A.1 shows a higher-level cartoon of the `iwc` workflow.

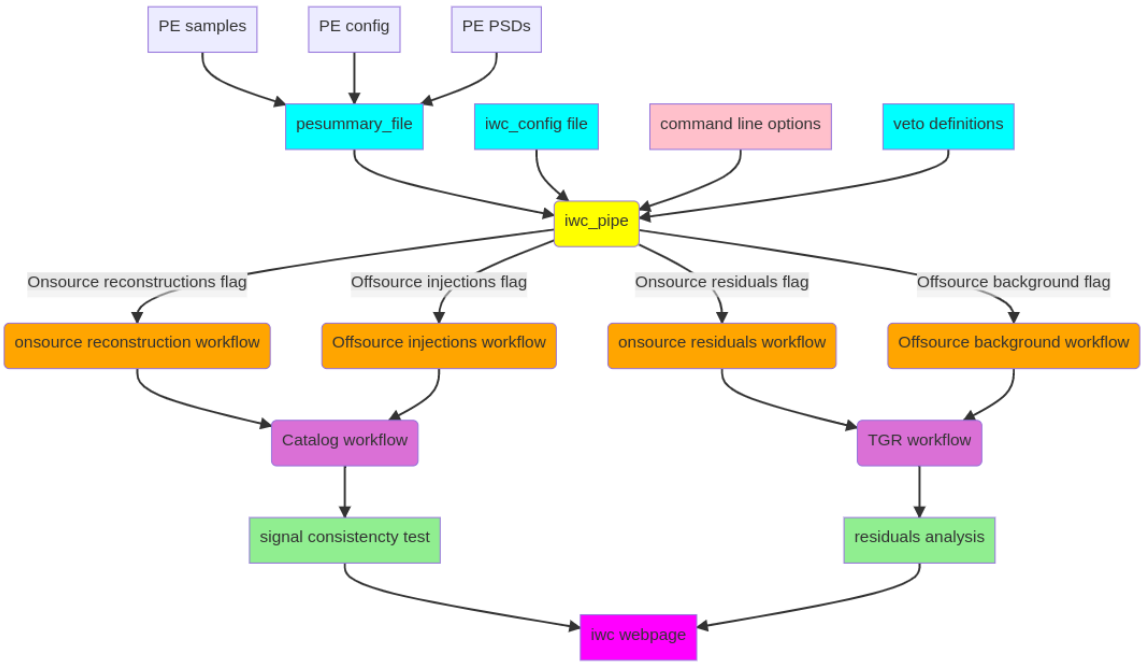

Figure A.1: Workflow of `igwn-wave-compare`

At the end of the workflow, it generates a web-page summarizing the important plots and quantities as shown in Figure A.2

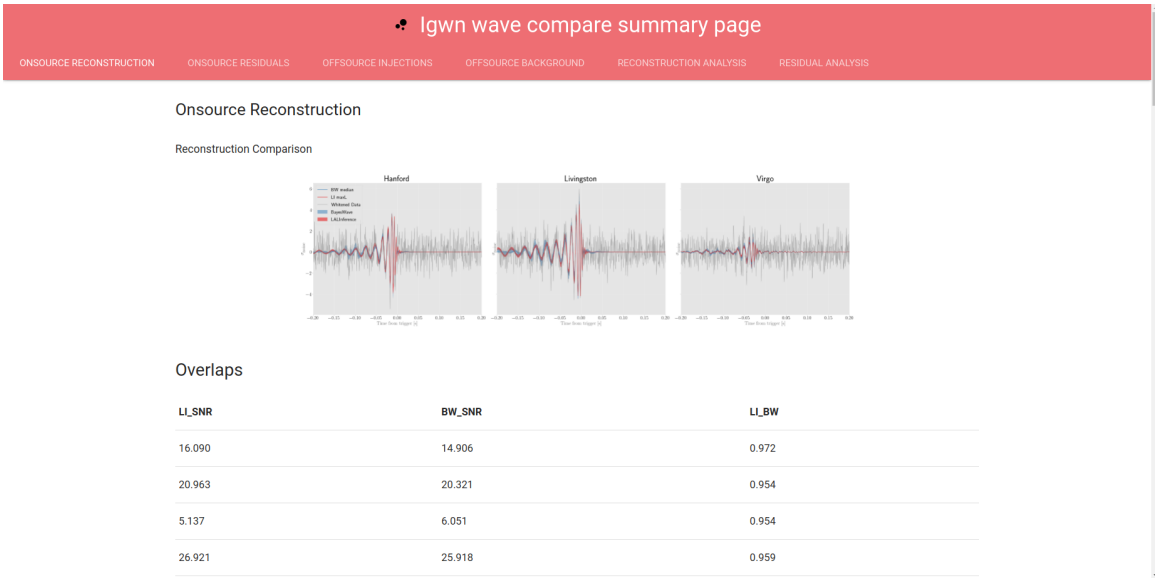

Figure A.2: Screenshot of of `iwc` webpage for the event GW200129

`iwc_pipe` does the following:

1. Takes as input the PE samples, PE coniguration file and PSDs used by PE. There are variations in formats the user can choose from.

2. Takes as input a `iwc`-specific config file that has information such as the number of background runs, maximum segment length (details below) and other `BayesWave` command line options.

3. Takes as input command line flags which turn on various sub-workflows described above.

4. Check for reassignment of the time-frequency configuration options.

5. In case of any offsource runs, generate random offsource times (described in section A.4)

6. Setup the workflow files and submit to the condor job management system.

A.2 Details of residual storage

The detector data are sampled and stored in so-called *frame files* which is a binary file format proprietary to LIGO. These are sampled at 16384 Hz. Template-based and `BayesWave` analyses typically use a maximum sampling rate of 4096 Hz. Hence, $\mathbf{h}(t)$ is up-sampled to 16384z and subtracted from the data. This residual data stream is then dumped into frame files with the same file format and then passed to `BayesWave`. We do this, instead of storing the data into an ASCII text file, is due to

LALSuite library routines that `BayesWave` uses to read data. The routines perform a few pre-processing operations before passing the dataset to `BayesWave`. Also, since the background detector data is also stored in frame files, this ensures both the onsource and background data undergo the exact same treatment.

A.3 Setting up the `BayesWave` time-frequency volume

For all the `BayesWave` analyses deployed for the signal consistency and residual tests, we wish to use same sampling rate and segment length as the template-based PE run. This is to ensure that our analyses use the same data and conditioning as the PE analysis. However, this is not always possible as `BayesWave` is limited in its ability to sample large time-frequency volumes, and in most cases, going beyond a certain segment length and sampling rate is not worth the increase in analysis run-time. In cases where the PE time-frequency configuration exceeds our limits, we default to the max values of 8 seconds and 2048 Hz respectively for the segment length and sampling rate. This is configurable in the `iwc` config file

`BayesWave` produces a sample of points in the parameter space of wavelets. Each point corresponds to a waveform and each waveform has a network SNR. These samples therefore give us a probability distribution on the network SNR. The median SNR is a stable estimate of the loudness of the data and is an appropriate figure of merit. However,

since we wish to place an upper limit on the residual excess, we use the 90% credible upper limit.

A.4 Selection of background times

We pick 200 random times in a window of 4096 seconds surrounding the event time for the background analysis. Before we select our random times, we need to prepare a list of time segments which are "allowed", i.e., time segments for which the detector was active, does not contain glitches, or is otherwise clean of time segments which have been flagged as being inappropriate for use in analyses. Our process selecting the allowed segments is as follows:

1. For each detector, download the analyzable segments from segments.ligo.org corresponding to the analysis-ready flags under use.

2. For each detector, get the category 1, 2, 3 and 4 veto segments from the veto definition file generated by the detector characterization group. Also get the hVeto segments

3. Subtract the category 1, 2, 3, 4 and hVeto segments from the analysis ready segments from step 1.

4. Take the intersection of the segments obtained for each detector obtained in step 3. These are the segments in which we are "allowed" to do background analyses.

Once we have the allowed segments, we place random 200 analysis segments using the procedure as follows:

1. Initialize an empty list of segments L. s is the segment length of the onsource analysis.

2. Pick a random time t in a window of 4096 seconds around the trigger time.

3. Construct a segment m with ends $(t - s + 2, t + 2)$.

4. If m lies fully within the "allowed" and if m does not intersect with any segments in L, then add m to L.

5. Stop when L has 200 segments.

APPENDIX B

SIMULATED OBSERVATIONS OF NON-GR WAVEFORMS

The following plots show the simulated non-GR waveforms used in [44] and discussed in section 5.5.

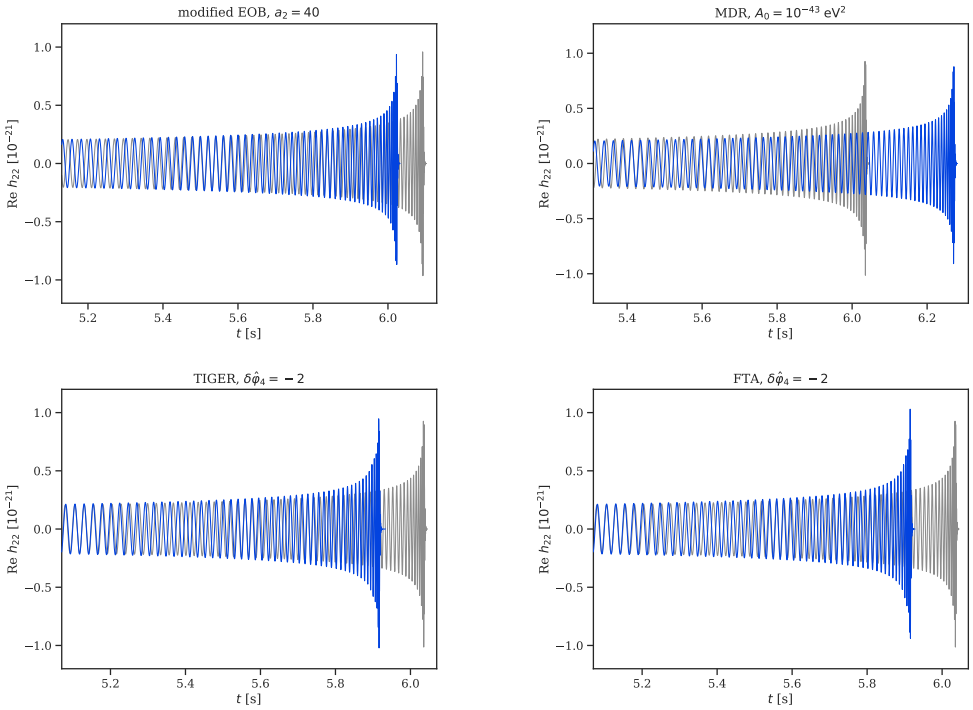

Figure B.1: . The GW170608-like waveforms in the time domain. We show the real part of the $\ell = m = 2$ spin-(-2)-weighted spherical harmonic mode of the strain, aligning the non-GR waveforms (blue) with the corresponding GR waveforms (grey) at 20 Hz, which is also the frequency at which the plots start. We show the final ~ 1 s of the signal.

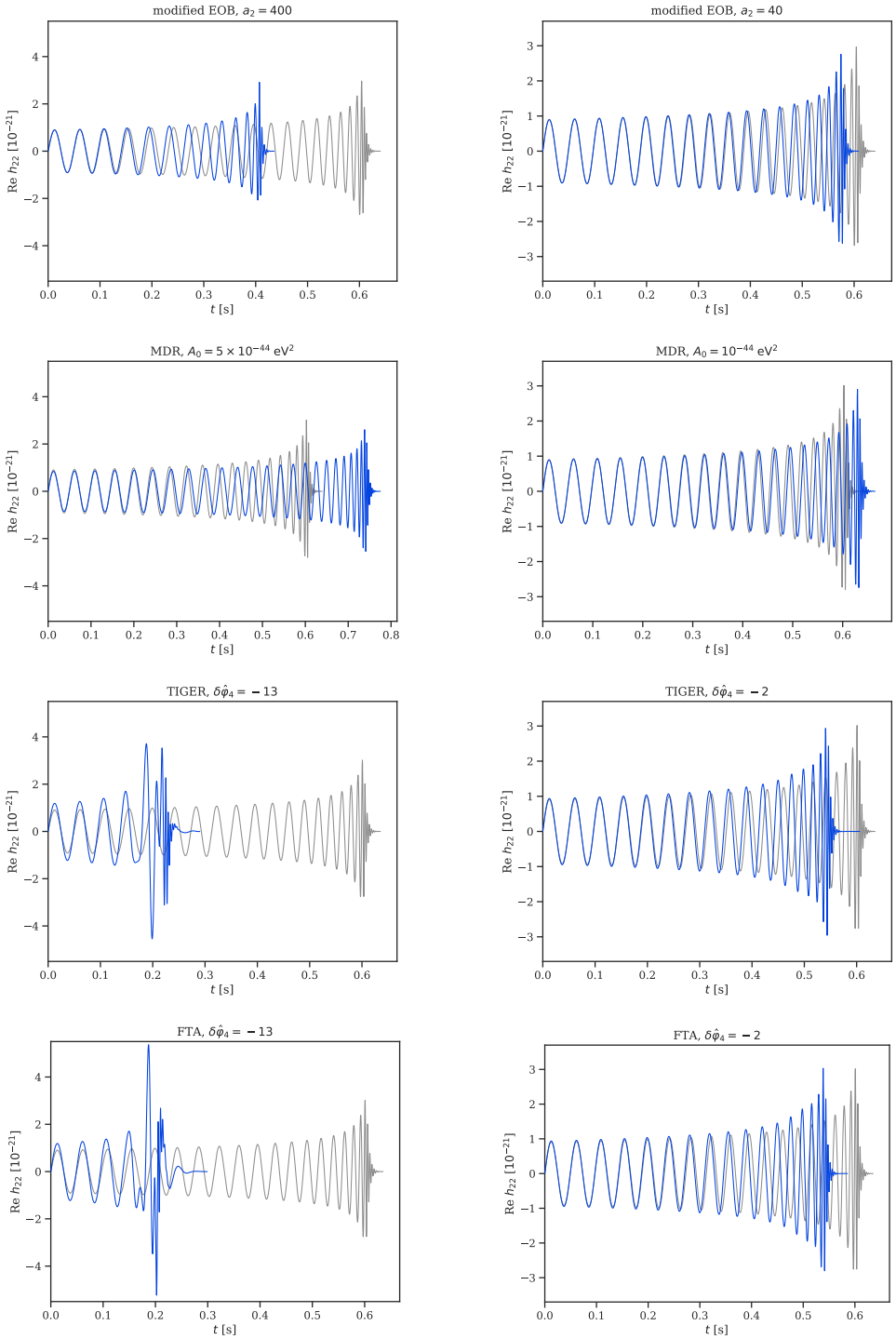

Figure B.2: The analog of Figure B.1 for the GW150914-like waveforms. The larger GR deviation is on the left, and thus those plots have a larger vertical axis range than those on the right.

REFERENCES

[1] A. Einstein, "Die grundlage der allgemeinen relativitätstheorie," *Annalen der Physik*, vol. 354, no. 7, pp. 769–822, 1916. eprint: https://onlinelibrary.wiley.com/doi/pdf/10.1002/andp.19163540702.

[2] A. Einstein, "Näherungsweise integration der feldgleichungen der gravitation," *Albert Einstein: Akademie-Vorträge: Sitzungsberichte der Preussischen Akademie der Wissenschaften 1914–1932*, pp. 99–108, 2005.

[3] J. Aasi *et al.*, "Advanced LIGO," *Class. Quant. Grav.*, vol. 32, p. 074 001, 2015. arXiv: 1411.4547 [gr-qc].

[4] B. P. Abbott, R. Abbott, T. Abbott, M. Abernathy, F. Acernese, K. Ackley, C. Adams, T. Adams, P. Addesso, R. Adhikari, *et al.*, "Observing gravitational-wave transient gw150914 with minimal assumptions," *Physical Review D*, vol. 93, no. 12, p. 122 004, 2016.

[5] B. P. Abbott *et al.*, "LIGO: The Laser interferometer gravitational-wave observatory," *Rept. Prog. Phys.*, vol. 72, p. 076 901, 2009. arXiv: 0711.3041 [gr-qc].

[6] F. Acernese *et al.*, "Advanced Virgo: a second-generation interferometric gravitational wave detector," *Class. Quant. Grav.*, vol. 32, no. 2, p. 024 001, 2015. arXiv: 1408.3978 [gr-qc].

[7] B. P. Abbott *et al.*, "GWTC-1: A Gravitational-Wave Transient Catalog of Compact Binary Mergers Observed by LIGO and Virgo during the First and Second Observing Runs," *Phys. Rev.*, vol. X9, no. 3, p. 031 040, 2019. arXiv: 1811.12907 [astro-ph.HE].

[8] R. Abbott *et al.*, "GWTC-2: Compact Binary Coalescences Observed by LIGO and Virgo During the First Half of the Third Observing Run," *Phys. Rev. X*, vol. 11, p. 021 053, 2021. arXiv: 2010.14527 [gr-qc].

[9] ——, "GWTC-3: Compact Binary Coalescences Observed by LIGO and Virgo During the Second Part of the Third Observing Run," Nov. 2021. arXiv: 2111.03606 [gr-qc].

[10] S. V. Dhurandhar and B. S. Sathyaprakash, "Choice of filters for the detection of gravitational waves from coalescing binaries. 2. Detection in colored noise," *Phys. Rev.*, vol. D49, pp. 1707–1722, 1994.

[11] L. K. Nuttall, "Characterizing transient noise in the ligo detectors," *Philosophical Transactions of the Royal Society A: Mathematical, Physical and Engineering Sciences*, vol. 376, no. 2120, p. 20 170 286, Apr. 2018.

[12] M. Shibata and K. Taniguchi, "Merger of binary neutron stars to a black hole: disk mass, short gamma-ray bursts, and quasinormal mode ringing," *Phys. Rev.*, vol. D73, p. 064 027, 2006. arXiv: astro-ph/0603145 [astro-ph].

[13] L. Baiotti, B. Giacomazzo, and L. Rezzolla, "Accurate evolutions of inspiralling neutron-star binaries: prompt and delayed collapse to black hole," *Phys. Rev.*, vol. D78, p. 084 033, 2008. arXiv: 0804.0594 [gr-qc].

[14] Z.-G. Xing, J. M. Centrella, and S. L. W. McMillan, "Gravitational radiation from coalescing binary neutron stars," *Phys. Rev.*, vol. D50, pp. 6247–6261, 1994. arXiv: gr-qc/9411029 [gr-qc].

[15] M. J. Szczepańczyk *et al.*, "Detecting and reconstructing gravitational waves from the next galactic core-collapse supernova in the advanced detector era," *Phys. Rev. D*, vol. 104, no. 10, p. 102 002, 2021. arXiv: 2104.06462 [astro-ph.HE].

[16] R. Abbott *et al.*, "All-sky search for continuous gravitational waves from isolated neutron stars in the early O3 LIGO data," *Phys. Rev. D*, vol. 104, no. 8, p. 082 004, 2021. arXiv: 2107.00600 [gr-qc].

[17] N. Christensen, "Stochastic Gravitational Wave Backgrounds," *Rept. Prog. Phys.*, vol. 82, no. 1, p. 016 903, 2019. arXiv: 1811.08797 [gr-qc].

[18] P. C. Peters, "Gravitational radiation and the motion of two point masses," *Phys. Rev.*, vol. 136, B1224–B1232, 4B Nov. 1964.

[19] P. Ajith *et al.*, "Inspiral-merger-ringdown waveforms for black-hole binaries with non-precessing spins," *Phys. Rev. Lett.*, vol. 106, p. 241 101, 2011. arXiv: 0909.2867 [gr-qc].

[20] L. Santamaria *et al.*, "Matching post-Newtonian and numerical relativity waveforms: systematic errors and a new phenomenological model for non-precessing black hole binaries," *Phys. Rev. D*, vol. 82, p. 064 016, 2010. arXiv: 1005.3306 [gr-qc].

[21] S. Husa, S. Khan, M. Hannam, M. Purrer, F. Ohme, X. J. Forteza, and A. Bohe, "Frequency-domain gravitational waves from nonprecessing black-hole binaries. i. new numerical waveforms and anatomy of the signal," *Phys. Rev. D*, vol. 93, p. 044 006, 4 Feb. 2016.

[22] Y. Pan, A. Buonanno, A. Taracchini, L. E. Kidder, A. H. Mroue, H. P. Pfeiffer, M. A. Scheel, and B. Szilagyi, "Inspiral-merger-ringdown waveforms of spinning, precessing black-hole binaries in the effective-one-body formalism," *Phys. Rev. D*, vol. 89, no. 8, p. 084 006, 2014. arXiv: 1307.6232 [gr-qc].

[23] A. Taracchini *et al.*, "Effective-one-body model for black-hole binaries with generic mass ratios and spins," *Phys. Rev.*, vol. D89, no. 6, p. 061 502, 2014. arXiv: 1311.2544 [gr-qc].

[24] A. Bohe, L. Shao, A. Taracchini, A. Buonanno, S. Babak, I. W. Harry, I. Hinder, S. Ossokine, M. Purrer, V. Raymond, T. Chu, H. Fong, P. Kumar, H. P. Pfeiffer, M. Boyle, D. A. Hemberger, L. E. Kidder, G. Lovelace, M. A. Scheel, and B. Szilagyi, "Improved effective-one-body model of spinning, nonprecessing binary black holes for the era of gravitational-wave astrophysics with advanced detectors," *Phys. Rev. D*, vol. 95, p. 044 028, 4 Feb. 2017.

[25] S. Babak, A. Taracchini, and A. Buonanno, "Validating the effective-one-body model of spinning, precessing binary black holes against numerical relativity," *Phys. Rev. D*, vol. 95, no. 2, p. 024 010, 2017. arXiv: 1607.05661 [gr-qc].

[26] L. Blanchet, B. R. Iyer, C. M. Will, and A. G. Wiseman, "Gravitational wave forms from inspiralling compact binaries to second postNewtonian order," *Class. Quant. Grav.*, vol. 13, pp. 575–584, 1996. arXiv: gr-qc/9602024 [gr-qc].

[27] T. Damour, P. Jaranowski, and G. Schaefer, "Dimensional regularization of the gravitational interaction of point masses in the ADM formalism," in *11th Marcel Grossmann Meeting on General Relativity*, Apr. 2008. arXiv: 0804.2386 [gr-qc].

[28] A. Buonanno, B. Iyer, E. Ochsner, Y. Pan, and B. S. Sathyaprakash, "Comparison of post-Newtonian templates for compact binary inspiral signals in gravitational-wave detectors," *Phys. Rev. D*, vol. 80, p. 084 043, 2009. arXiv: 0907.0700 [gr-qc].

[29] L. Blanchet, "Gravitational Radiation from Post-Newtonian Sources and Inspiralling Compact Binaries," *Living Rev. Rel.*, vol. 17, p. 2, 2014. arXiv: 1310.1528 [gr-qc].

[30] A. Buonanno and T. Damour, "Effective one-body approach to general relativistic two-body dynamics," *Phys. Rev.*, vol. D59, p. 084 006, 1999. arXiv: gr-qc/9811091 [gr-qc].

[31] A. Buonanno and T. Damour, "Transition from inspiral to plunge in binary black hole coalescences," *Phys. Rev.*, vol. D62, p. 064 015, 2000. arXiv: gr-qc/0001013 [gr-qc].

[32] T. Damour, P. Jaranowski, and G. Schaefer, "Effective one body approach to the dynamics of two spinning black holes with next-to-leading order spin-orbit coupling," *Phys. Rev.*, vol. D78, p. 024 009, 2008. arXiv: 0803.0915 [gr-qc].

[33] T. Damour and A. Nagar, "An Improved analytical description of inspiralling and coalescing black-hole binaries," *Phys. Rev.*, vol. D79, p. 081 503, 2009. arXiv: 0902.0136 [gr-qc].

[34] F. Pretorius, "Evolution of binary black hole spacetimes," *Phys. Rev. Lett.*, vol. 95, p. 121 101, 2005. arXiv: gr-qc/0507014 [gr-qc].

[35] M. Campanelli, C. O. Lousto, P. Marronetti, and Y. Zlochower, "Accurate evolutions of orbiting black-hole binaries without excision," *Phys. Rev. Lett.*, vol. 96, p. 111 101, 2006. arXiv: gr-qc/0511048 [gr-qc].

[36] J. G. Baker, J. Centrella, D.-I. Choi, M. Koppitz, and J. van Meter, "Gravitational wave extraction from an inspiraling configuration of merging black holes," *Phys. Rev. Lett.*, vol. 96, p. 111 102, 2006. arXiv: gr-qc/0511103 [gr-qc].

[37] A. H. Mroue *et al.*, "Catalog of 174 Binary Black Hole Simulations for Gravitational Wave Astronomy," *Phys. Rev. Lett.*, vol. 111, no. 24, p. 241 104, 2013. arXiv: 1304.6077 [gr-qc].

[38] S. Khan, S. Husa, M. Hannam, F. Ohme, M. Purrer, X. J. Forteza, and A. Bohe, "Frequency-domain gravitational waves from nonprecessing black-hole binaries. ii. a phenomenological model for the advanced detector era," *Phys. Rev. D*, vol. 93, p. 044 007, 4 Feb. 2016.

[39] T. Chu, H. Fong, P. Kumar, H. P. Pfeiffer, M. Boyle, D. A. Hemberger, L. E. Kidder, M. A. Scheel, and B. Szilagyi, "On the accuracy and precision of numerical waveforms: Effect of waveform extraction methodology," *Class. Quant. Grav.*, vol. 33, no. 16, p. 165 001, 2016. arXiv: 1512.06800 [gr-qc].

[40] S. Klimenko, I. Yakushin, A. Mercer, and G. Mitselmakher, "A coherent method for detection of gravitational wave bursts," *Classical and Quantum Gravity*, vol. 25, no. 11, p. 114 029, May 2008.

[41] R. Lynch, S. Vitale, R. Essick, E. Katsavounidis, and F. Robinet, "Information-theoretic approach to the gravitational-wave burst detection problem," *Phys. Rev.*, vol. D95, no. 10, p. 104 046, 2017. arXiv: 1511.05955 [gr-qc].

[42] N. J. Cornish and T. B. Littenberg, "Bayeswave: Bayesian inference for gravitational wave bursts and instrument glitches," *Classical and Quantum Gravity*, vol. 32, no. 13, p. 135 012, 2015.

[43] S. Ghonge, K. Chatziioannou, J. A. Clark, T. Littenberg, M. Millhouse, L. Cadonati, and N. Cornish, "Reconstructing gravitational wave signals from binary black hole mergers with minimal assumptions," *Phys. Rev. D*, vol. 102, no. 6, p. 064 056, 2020. arXiv: 2003.09456 [gr-qc].

[44] N. K. Johnson-McDaniel, A. Ghosh, S. Ghonge, M. Saleem, N. V. Krishnendu, and J. A. Clark, "Investigating the relation between gravitational wave tests of general relativity," Sep. 2021. arXiv: 2109.06988 [gr-qc].

[45] N. J. Cornish, T. B. Littenberg, B. Bécsy, K. Chatziioannou, J. A. Clark, S. Ghonge, and M. Millhouse, "BayesWave analysis pipeline in the era of gravitational wave observations," *Phys. Rev. D*, vol. 103, no. 4, p. 044 006, 2021. arXiv: 2011.09494 [gr-qc].

[46] K. Chatziioannou, J. A. Clark, A. Bauswein, M. Millhouse, T. B. Littenberg, and N. Cornish, "Inferring the post-merger gravitational wave emission from binary neutron star coalescences," *Phys. Rev.*, vol. D96, no. 12, p. 124 035, 2017. arXiv: 1711.00040 [gr-qc].

[47] P. J. Easter, S. Ghonge, P. D. Lasky, A. R. Casey, J. A. Clark, F. H. Vivanco, and K. Chatziioannou, "Detection and parameter estimation of binary neutron star merger remnants," *Phys. Rev. D*, vol. 102, no. 4, p. 043 011, 2020. arXiv: 2006.04396 [astro-ph.HE].

[48] K. Chatziioannou *et al.*, "On the properties of the massive binary black hole merger GW170729," 2019. arXiv: 1903.06742 [gr-qc].

[49] D. Ferguson, S. Ghonge, J. A. Clark, J. Calderon Bustillo, P. Laguna, D. Shoemaker, and J. Calderon Bustillo, "Measuring Spin of the Remnant Black Hole from Maximum Amplitude," *Phys. Rev. Lett.*, vol. 123, no. 15, p. 151 101, 2019. arXiv: 1905.03756 [gr-qc].

[50] B. P. Abbott *et al.*, "Tests of General Relativity with the Binary Black Hole Signals from the LIGO-Virgo Catalog GWTC-1," 2019. arXiv: 1903.04467 [gr-qc].

[51] R. Abbott *et al.*, "Tests of general relativity with binary black holes from the second LIGO-Virgo gravitational-wave transient catalog," *Phys. Rev. D*, vol. 103, no. 12, p. 122 002, 2021. arXiv: 2010.14529 [gr-qc].

[52] I. Newton, *Philosophiae naturalis principia mathematica*. Jussu Societatis Regiae ac typis Josephi Streater, prostant venales apud Sam, 2009, vol. 62.

[53] H. Guo, "A new paradox and the reconciliation of lorentz and galilean transformations," *Synthese*, pp. 1–30, 2021.

[54] A. Einstein, "Zur elektrodynamik bewegter korper," *Annalen der physik*, vol. 4, 1905.

[55] E. J. Post, *Formal structure of electromagnetics: general covariance and electromagnetics*. Courier Corporation, 1997.

[56] Y. Aso, Y. Michimura, K. Somiya, M. Ando, O. Miyakawa, T. Sekiguchi, D. Tatsumi, and H. Yamamoto, "Interferometer design of the KAGRA gravitational wave detector," *Phys. Rev.*, vol. D88, no. 4, p. 043 007, 2013. arXiv: 1306.6747 [gr-qc].

[57] M. Saleem *et al.*, "The Science Case for LIGO-India," May 2021. arXiv: 2105.01716 [gr-qc].

[58] K. Riles, "Gravitational Waves: Sources, Detectors and Searches," *Prog. Part. Nucl. Phys.*, vol. 68, pp. 1–54, 2013. arXiv: 1209.0667 [hep-ex].

[59] G. M. H. and, "Advanced LIGO: The next generation of gravitational wave detectors," *Classical and Quantum Gravity*, vol. 27, no. 8, p. 084 006, Apr. 2010.

[60] M. Maggiore *et al.*, "Science Case for the Einstein Telescope," *JCAP*, vol. 03, p. 050, 2020. arXiv: 1912.02622 [astro-ph.CO].

[61] M. Evans *et al.*, "A Horizon Study for Cosmic Explorer: Science, Observatories, and Community," Sep. 2021. arXiv: 2109.09882 [astro-ph.IM].

[62] M. Isi and A. J. Weinstein, "Probing gravitational wave polarizations with signals from compact binary coalescences," Oct. 2017. arXiv: 1710.03794 [gr-qc].

[63] B. P. Abbott, R. Abbott, T. Abbott, M. Abernathy, F. Acernese, K. Ackley, C. Adams, T. Adams, P. Addesso, R. Adhikari, *et al.*, "Observation of gravitational waves from a binary black hole merger," *Physical review letters*, vol. 116, no. 6, p. 061 102, 2016.

[64] B. P. Abbott, R. Abbott, T. Abbott, M. Abernathy, F. Acernese, K. Ackley, M. Adamo, C. Adams, T. Adams, P. Addesso, *et al.*, "Characterization of transient noise in advanced ligo relevant to gravitational wave signal gw150914," *Classical and Quantum Gravity*, vol. 33, no. 13, p. 134 001, 2016.

[65] J. Abadie *et al.*, "Predictions for the Rates of Compact Binary Coalescences Observable by Ground-based Gravitational-wave Detectors," *Class. Quant. Grav.*, vol. 27, p. 173 001, 2010. arXiv: 1003.2480 [astro-ph.HE].

[66] K. L. Dooley, L. S. Collaboration, *et al.*, "Status of geo 600," in *Journal of Physics: Conference Series*, IOP Publishing, vol. 610, 2015, p. 012 015.

[67] L. McCuller and L. Barsotti, "Design requirement document of the a+ filter cavity and relay optics for frequency dependent squeezing," Technical Report, Tech. Rep., 2020.

[68] M. Punturo, M. Abernathy, F. Acernese, B. Allen, N. Andersson, K. Arun, F. Barone, B. Barr, M. Barsuglia, M. Beker, *et al.*, "The einstein telescope: A third-generation gravitational wave observatory," *Classical and Quantum Gravity*, vol. 27, no. 19, p. 194 002, 2010.

[69] K. Ackley *et al.*, "Neutron Star Extreme Matter Observatory: A kilohertz-band gravitational-wave detector in the global network," *Publ. Astron. Soc. Austral.*, vol. 37, e047, 2020. arXiv: 2007.03128 [astro-ph.HE].

[70] J. Baker *et al.*, "The Laser Interferometer Space Antenna: Unveiling the Millihertz Gravitational Wave Sky," Jul. 2019. arXiv: 1907.06482 [astro-ph.IM].

[71] M. Abernathy, F. Acernese, P. Ajith, B. Allen, P. Amaro Seoane, N. Andersson, S. Aoudia, P. Astone, B. Krishnan, L. Barack, *et al.*, "Einstein gravitational wave telescope conceptual design study," 2011.

[72] D. R. Lorimer and M. Kramer, "Handbook of pulsar astronomy," *Handbook of Pulsar Astronomy*, 2012.

[73] D. Bhattacharya and E. P. J. van den Heuvel, "Formation and evolution of binary and millisecond radio pulsars," *Physics Reports*, vol. 203, no. 1-2, pp. 1–124, 1991.

[74] B. B. P. Perera *et al.*, "The International Pulsar Timing Array: Second data release," *Mon. Not. Roy. Astron. Soc.*, vol. 490, no. 4, pp. 4666–4687, 2019. arXiv: 1909.04534 [astro-ph.HE].

[75] C. J. Moore, R. H. Cole, and C. P. L. Berry, "Gravitational-wave sensitivity curves," *Class. Quant. Grav.*, vol. 32, no. 1, p. 015 014, 2015. arXiv: 1408.0740 [gr-qc].

[76] K. S. Thorne, "Gravitational waves," 1995, pp. 0160–184. arXiv: gr-qc/9506086 [gr-qc].

[77] L. S. Collaboration, V. Collaboration, *et al.*, "Gwtc-1: A gravitational-wave transient catalog of compact binary mergers observed by ligo and virgo during the first and second observing runs," *arXiv preprint arXiv:1811.12907*, 2018.

[78] J. Casares and P. G. Jonker, "Mass measurements of stellar and intermediate-mass black holes," *Space Science Reviews*, vol. 183, no. 1, pp. 223–252, Sep. 2014.

[79] B. P. Abbott, R. Abbott, T. Abbott, M. Abernathy, F. Acernese, K. Ackley, C. Adams, T. Adams, P. Addesso, R. Adhikari, *et al.*, "Properties of the binary black

hole merger gw150914," *Physical Review Letters*, vol. 116, no. 24, p. 241 102, 2016.

[80] B. P. Abbott *et al.*, "Multi-messenger Observations of a Binary Neutron Star Merger," *Astrophys. J.*, vol. 848, no. 2, p. L12, 2017. arXiv: 1710.05833 [astro-ph.HE].

[81] A. Goldstein *et al.*, "An Ordinary Short Gamma-Ray Burst with Extraordinary Implications: Fermi-GBM Detection of GRB 170817A," *Astrophys. J.*, vol. 848, no. 2, p. L14, 2017. arXiv: 1710.05446 [astro-ph.HE].

[82] V. Savchenko *et al.*, "INTEGRAL Detection of the First Prompt Gamma-Ray Signal Coincident with the Gravitational-wave Event GW170817," *Astrophys. J.*, vol. 848, no. 2, p. L15, 2017. arXiv: 1710.05449 [astro-ph.HE].

[83] R. Abbott *et al.*, "GW190521: A Binary Black Hole Merger with a Total Mass of $150M_{\odot}$," *Phys. Rev. Lett.*, vol. 125, no. 10, p. 101 102, 2020. arXiv: 2009.01075 [gr-qc].

[84] ——, "Properties and Astrophysical Implications of the 150 $M_{\odot}$ Binary Black Hole Merger GW190521," *Astrophys. J. Lett.*, vol. 900, no. 1, p. L13, 2020. arXiv: 2009.01190 [astro-ph.HE].

[85] S. E. Woosley, "Pulsational Pair-Instability Supernovae," *Astrophys. J.*, vol. 836, no. 2, p. 244, 2017. arXiv: 1608.08939 [astro-ph.HE].

[86] U. N. Di Carlo, N. Giacobbo, M. Mapelli, M. Pasquato, M. Spera, L. Wang, and F. Haardt, "Merging black holes in young star clusters," *Monthly Notices of the Royal Astronomical Society*, vol. 487, no. 2, pp. 2947–2960, 2019.

[87] D. Gerosa and E. Berti, "Are merging black holes born from stellar collapse or previous mergers?" *Phys. Rev. D*, vol. 95, no. 12, p. 124 046, 2017. arXiv: 1703.06223 [gr-qc].

[88] Y. Yang *et al.*, "Hierarchical Black Hole Mergers in Active Galactic Nuclei," *Phys. Rev. Lett.*, vol. 123, no. 18, p. 181 101, 2019. arXiv: 1906.09281 [astro-ph.HE].

[89] T. Ebisuzaki, J. Makino, T. G. Tsuru, Y. Funato, S. F. Portegies Zwart, P. Hut, S. McMillan, S. Matsushita, H. Matsumoto, and R. Kawabe, "Missing link found? – the "runaway" path to supermassive black holes," *Astrophys. J. Lett.*, vol. 562, p. L19, 2001. arXiv: astro-ph/0106252.

[90] R. Abbott *et al.*, "GW190814: Gravitational Waves from the Coalescence of a 23 Solar Mass Black Hole with a 2.6 Solar Mass Compact Object," *Astrophys. J. Lett.*, vol. 896, no. 2, p. L44, 2020. arXiv: 2006.12611 [astro-ph.HE].

[91] M. Dominik, K. Belczynski, C. Fryer, D. Holz, E. Berti, T. Bulik, I. Mandel, and R. O'Shaughnessy, "Double Compact Objects I: The Significance of the Common Envelope on Merger Rates," *Astrophys. J.*, vol. 759, p. 52, 2012. arXiv: 1202.4901 [astro-ph.HE].

[92] M. Dominik, E. Berti, R. O'Shaughnessy, I. Mandel, K. Belczynski, C. Fryer, D. E. Holz, T. Bulik, and F. Pannarale, "Double Compact Objects III: Gravitational Wave Detection Rates," *Astrophys. J.*, vol. 806, no. 2, p. 263, 2015. arXiv: 1405.7016 [astro-ph.HE].

[93] N. Giacobbo and M. Mapelli, "The progenitors of compact-object binaries: Impact of metallicity, common envelope and natal kicks," *Monthly Notices of the Royal Astronomical Society*, vol. 480, no. 2, pp. 2011–2030, 2018.

[94] M. U. Kruckow, T. M. Tauris, N. Langer, M. Kramer, and R. G. Izzard, "Progenitors of gravitational wave mergers: Binary evolution with the stellar grid-based code combine," *Monthly Notices of the Royal Astronomical Society*, vol. 481, no. 2, pp. 1908–1949, 2018.

[95] C. J. Neijssel, A. Vigna-Gómez, S. Stevenson, J. W. Barrett, S. M. Gaebel, F. S. Broekgaarden, S. E. de Mink, D. Szécsi, S. Vinciguerra, and I. Mandel, "The effect of the metallicity-specific star formation history on double compact object mergers," *Monthly Notices of the Royal Astronomical Society*, vol. 490, no. 3, pp. 3740–3759, 2019.

[96] "The population of merging compact binaries inferred using gravitational waves through GWTC-3," Nov. 2021. arXiv: 2111.03634 [astro-ph.HE].

[97] C. Vishveshwara, "Scattering of gravitational radiation by a schwarzschild black-hole," *Nature*, vol. 227, no. 5261, p. 936, 1970.

[98] C. Rover, R. Meyer, and N. Christensen, "Bayesian inference on compact binary inspiral gravitational radiation signals in interferometric data," *Classical and Quantum Gravity*, vol. 23, no. 15, p. 4895, 2006.

[99] J. Veitch and A. Vecchio, "Bayesian coherent analysis of in-spiral gravitational wave signals with a detector network," *Physical Review D*, vol. 81, no. 6, p. 062 003, 2010.

[100] E. Barausse and A. Buonanno, "An Improved effective-one-body Hamiltonian for spinning black-hole binaries," *Phys. Rev.*, vol. D81, p. 084 024, 2010. arXiv: 0912.3517 [gr-qc].

[101] S. A. Usman, A. H. Nitz, I. W. Harry, C. M. Biwer, D. A. Brown, M. Cabero, C. D. Capano, T. Dal Canton, T. Dent, S. Fairhurst, *et al.*, "The pycbc search for gravita-

tional waves from compact binary coalescence," *Classical and Quantum Gravity*, vol. 33, no. 21, p. 215 004, 2016.

[102] J. S. Read, C. Markakis, M. Shibata, K. Uryu, J. D. E. Creighton, and J. L. Friedman, "Measuring the neutron star equation of state with gravitational wave observations," *Phys. Rev.*, vol. D79, p. 124 033, 2009. arXiv: 0901.3258 [gr-qc].

[103] T. Binnington and E. Poisson, "Relativistic theory of tidal Love numbers," *Phys. Rev.*, vol. D80, p. 084 018, 2009. arXiv: 0906.1366 [gr-qc].

[104] T. Damour, A. Nagar, and L. Villain, "Measurability of the tidal polarizability of neutron stars in late-inspiral gravitational-wave signals," *Phys. Rev.*, vol. D85, p. 123 007, 2012. arXiv: 1203.4352 [gr-qc].

[105] E. E. Flanagan and T. Hinderer, "Constraining neutron star tidal Love numbers with gravitational wave detectors," *Phys. Rev.*, vol. D77, p. 021 502, 2008. arXiv: 0709.1915 [astro-ph].

[106] B. P. Abbott *et al.*, "Properties of the binary neutron star merger GW170817," *Phys. Rev.*, vol. X9, no. 1, p. 011 001, 2019. arXiv: 1805.11579 [gr-qc].

[107] ——, "GW170817: Measurements of neutron star radii and equation of state," *Phys. Rev. Lett.*, vol. 121, no. 16, p. 161 101, 2018. arXiv: 1805.11581 [gr-qc].

[108] D. Kasen, R. Fernandez, and B. Metzger, "Kilonova light curves from the disc wind outflows of compact object mergers," *Mon. Not. Roy. Astron. Soc.*, vol. 450, pp. 1777–1786, 2015. arXiv: 1411.3726 [astro-ph.HE].

[109] J. Clark, A. Bauswein, L. Cadonati, H. .-T. Janka, C. Pankow, and N. Stergioulas, "Prospects For High Frequency Burst Searches Following Binary Neutron Star Coalescence With Advanced Gravitational Wave Detectors," *Phys. Rev.*, vol. D90, no. 6, p. 062 004, 2014. arXiv: 1406.5444 [astro-ph.HE].

[110] S. Bose, K. Chakravarti, L. Rezzolla, B. S. Sathyaprakash, and K. Takami, "Neutron-star Radius from a Population of Binary Neutron Star Mergers," *Phys. Rev. Lett.*, vol. 120, no. 3, p. 031 102, 2018. arXiv: 1705.10850 [gr-qc].

[111] T. Bayes, "Lii. an essay towards solving a problem in the doctrine of chances. by the late rev. mr. bayes, frs communicated by mr. price, in a letter to john canton, amfr s," *Philosophical transactions of the Royal Society of London*, no. 53, pp. 370–418, 1763.

[112] E. T. Jaynes, *Probability theory: the logic of science*. Washington University St. Louis, MO, 1996.

[113] Y. Kodama, T. Odajima, E. Arima, and M. Sato, "Evaluation of power management control on the supercomputer fugaku," in *2020 IEEE International Conference on Cluster Computing (CLUSTER)*, IEEE, 2020, pp. 484–493.

[114] W. R. Gilks, S. Richardson, and D. Spiegelhalter, *Markov chain Monte Carlo in practice*. Chapman and Hall/CRC, 1995.

[115] N. Metropolis, A. W. Rosenbluth, M. N. Rosenbluth, A. H. Teller, and E. Teller, "Equation of state calculations by fast computing machines," *J. Chem. Phys.*, vol. 21, pp. 1087–1092, 1953.

[116] S. Geman and D. Geman, "Stochastic relaxation, gibbs distributions, and the bayesian restoration of images," in *Readings in computer vision*, Elsevier, 1987, pp. 564–584.

[117] C. Rover, R. Meyer, and N. Christensen, "Bayesian inference on compact binary inspiral gravitational radiation signals in interferometric data," *Class. Quant. Grav.*, vol. 23, pp. 4895–4906, 2006. arXiv: gr-qc/0602067 [gr-qc].

[118] N. Christensen and R. Meyer, "Using Markov chain Monte Carlo methods for estimating parameters with gravitational radiation data," *Phys. Rev.*, vol. D64, p. 022 001, 2001. arXiv: gr-qc/0102018 [gr-qc].

[119] C. Rover, R. Meyer, and N. Christensen, "Coherent Bayesian inference on compact binary inspirals using a network of interferometric gravitational wave detectors," *Phys. Rev.*, vol. D75, p. 062 004, 2007. arXiv: gr-qc/0609131 [gr-qc].

[120] V. Raymond, M. V. van der Sluys, I. Mandel, V. Kalogera, C. Rover, and N. Christensen, "The Effects of LIGO detector noise on a 15-dimensional Markov-chain Monte-Carlo analysis of gravitational-wave signals," *Class. Quant. Grav.*, vol. 27, p. 114 009, 2010. arXiv: 0912.3746 [gr-qc].

[121] J. Skilling *et al.*, "Nested sampling for general bayesian computation," *Bayesian analysis*, vol. 1, no. 4, pp. 833–859, 2006.

[122] J. Veitch and A. Vecchio, "Bayesian coherent analysis of in-spiral gravitational wave signals with a detector network," *Phys. Rev.*, vol. D81, p. 062 003, 2010. arXiv: 0911.3820 [astro-ph.CO].

[123] F. Feroz, M. P. Hobson, E. Cameron, and A. N. Pettitt, "Importance Nested Sampling and the MultiNest Algorithm," *Open J. Astrophys.*, vol. 2, no. 1, p. 10, 2019. arXiv: 1306.2144 [astro-ph.IM].

[124] M. van de Meent and H. P. Pfeiffer, "Intermediate mass-ratio black hole binaries: Applicability of small mass-ratio perturbation theory," *Phys. Rev. Lett.*, vol. 125, no. 18, p. 181 101, 2020. arXiv: 2006.12036 [gr-qc].

[125] K.-W. Lo and L.-M. Lin, "The spin parameter of uniformly rotating compact stars," *Astrophys. J.*, vol. 728, p. 12, 2011. arXiv: 1011.3563 [astro-ph.HE].

[126] P. Ajith *et al.*, "The NINJA-2 catalog of hybrid post-Newtonian/numerical-relativity waveforms for non-precessing black-hole binaries," *Class. Quant. Grav.*, vol. 29, p. 124 001, 2012, [Erratum: Class. Quant. Grav.30,199401(2013)]. arXiv: 1201.5319 [gr-qc].

[127] A. Nagar, T. Damour, C. Reisswig, and D. Pollney, "Energetics and phasing of nonprecessing spinning coalescing black hole binaries," *Phys. Rev.*, vol. D93, no. 4, p. 044 046, 2016. arXiv: 1506.08457 [gr-qc].

[128] P. Ajith *et al.*, "A Template bank for gravitational waveforms from coalescing binary black holes. I. Non-spinning binaries," *Phys. Rev.*, vol. D77, p. 104 017, 2008, [Erratum: Phys. Rev.D79,129901(2009)]. arXiv: 0710.2335 [gr-qc].

[129] Y. Pan, A. Buonanno, J. G. Baker, J. Centrella, B. J. Kelly, S. T. McWilliams, F. Pretorius, and J. R. van Meter, "A Data-analysis driven comparison of analytic and numerical coalescing binary waveforms: Nonspinning case," *Phys. Rev.*, vol. D77, p. 024 014, 2008. arXiv: 0704.1964 [gr-qc].

[130] P. Ajith *et al.*, "Phenomenological template family for black-hole coalescence waveforms," *Class. Quant. Grav.*, vol. 24, S689–S700, 2007. arXiv: 0704.3764 [gr-qc].

[131] M. Pürrer, "Frequency domain reduced order models for gravitational waves from aligned-spin compact binaries," *Class. Quant. Grav.*, vol. 31, no. 19, p. 195 010, 2014. arXiv: 1402.4146 [gr-qc].

[132] ——, "Frequency domain reduced order model of aligned-spin effective-one-body waveforms with generic mass-ratios and spins," *Phys. Rev.*, vol. D93, no. 6, p. 064 041, 2016. arXiv: 1512.02248 [gr-qc].

[133] P. Schmidt, M. Hannam, and S. Husa, "Towards models of gravitational waveforms from generic binaries: A simple approximate mapping between precessing and non-precessing inspiral signals," *Phys. Rev.*, vol. D86, p. 104 063, 2012. arXiv: 1207.3088 [gr-qc].

[134] K. C. B. New, "Gravitational waves from gravitational collapse," *Living Rev. Rel.*, vol. 6, p. 2, 2003. arXiv: gr-qc/0206041 [gr-qc].

[135] B. P. Abbott *et al.*, "Search for Post-merger Gravitational Waves from the Remnant of the Binary Neutron Star Merger GW170817," *Astrophys. J.*, vol. 851, no. 1, p. L16, 2017. arXiv: 1710.09320 [astro-ph.HE].

[136] A. Torres-Rivas, K. Chatziioannou, A. Bauswein, and J. A. Clark, "Observing the post-merger signal of GW170817-like events with improved gravitational-wave detectors," *Phys. Rev.*, vol. D99, no. 4, p. 044 014, 2019. arXiv: 1811.08931 [gr-qc].

[137] K. S. Thorne, "Multipole Expansions of Gravitational Radiation," *Rev. Mod. Phys.*, vol. 52, pp. 299–339, 1980.

[138] J. Calderon Bustillo, "Sub-dominant modes of the gravitational radiation from compact binary coalescences: Construction of hybrid waveforms and impact on gravitational wave searches," 2019.

[139] U. Sperhake, B. J. Kelly, P. Laguna, K. L. Smith, and E. Schnetter, "Black hole head-on collisions and gravitational waves with fixed mesh-refinement and dynamic singularity excision," *Phys. Rev.*, vol. D71, p. 124 042, 2005. arXiv: gr-qc/0503071 [gr-qc].

[140] R. Abbott *et al.*, "GW190412: Observation of a Binary-Black-Hole Coalescence with Asymmetric Masses," *Phys. Rev. D*, vol. 102, no. 4, p. 043 015, 2020. arXiv: 2004.08342 [astro-ph.HE].

[141] J. Calderón Bustillo, C. Evans, J. A. Clark, G. Kim, P. Laguna, and D. Shoemaker, "Gravitational-wave imaging of black hole horizons: Post-merger chirps from binary black holes," 2019. arXiv: 1906.01153 [gr-qc].

[142] J. Calderón Bustillo, J. A. Clark, P. Laguna, and D. Shoemaker, "Tracking black hole kicks from gravitational wave observations," *Phys. Rev. Lett.*, vol. 121, no. 19, p. 191 102, 2018. arXiv: 1806.11160 [gr-qc].

[143] L. London, S. Khan, E. Fauchon-Jones, C. García, M. Hannam, S. Husa, X. Jiménez-Forteza, C. Kalaghatgi, F. Ohme, and F. Pannarale, "First higher-multipole model of gravitational waves from spinning and coalescing black-hole binaries," *Phys. Rev. Lett.*, vol. 120, no. 16, p. 161 102, 2018. arXiv: 1708.00404 [gr-qc].

[144] R. Cotesta, A. Buonanno, A. Bohé, A. Taracchini, I. Hinder, and S. Ossokine, "Enriching the Symphony of Gravitational Waves from Binary Black Holes by Tuning Higher Harmonics," *Phys. Rev.*, vol. D98, no. 8, p. 084 028, 2018. arXiv: 1803.10701 [gr-qc].

[145] J. Blackman, S. E. Field, C. R. Galley, B. Szilágyi, M. A. Scheel, M. Tiglio, and D. A. Hemberger, "Fast and Accurate Prediction of Numerical Relativity Wave-

forms from Binary Black Hole Coalescences Using Surrogate Models," *Phys. Rev. Lett.*, vol. 115, no. 12, p. 121 102, 2015. arXiv: 1502.07758 [gr-qc].

[146] J. Blackman, S. E. Field, M. A. Scheel, C. R. Galley, D. A. Hemberger, P. Schmidt, and R. Smith, "A Surrogate Model of Gravitational Waveforms from Numerical Relativity Simulations of Precessing Binary Black Hole Mergers," *Phys. Rev.*, vol. D95, no. 10, p. 104 023, 2017. arXiv: 1701.00550 [gr-qc].

[147] J. Blackman, S. E. Field, M. A. Scheel, C. R. Galley, C. D. Ott, M. Boyle, L. E. Kidder, H. P. Pfeiffer, and B. Szilágyi, "Numerical relativity waveform surrogate model for generically precessing binary black hole mergers," *Phys. Rev.*, vol. D96, no. 2, p. 024 058, 2017. arXiv: 1705.07089 [gr-qc].

[148] *Ligo grace db https://gracedb.ligo.org/latest/*.

[149] S. P. Wright, "Adjusted P-Values for Simultaneous Inference," *Biometrics*, vol. 48, no. 4, pp. 1005–1013, 1992.

[150] B. Allen, W. G. Anderson, P. R. Brady, D. A. Brown, and J. D. E. Creighton, "FINDCHIRP: An Algorithm for detection of gravitational waves from inspiraling compact binaries," *Phys. Rev.*, vol. D85, p. 122 006, 2012. arXiv: gr-qc/0509116 [gr-qc].

[151] B. J. Owen, "Search templates for gravitational waves from inspiraling binaries: Choice of template spacing," *Phys. Rev.*, vol. D53, pp. 6749–6761, 1996. arXiv: gr-qc/9511032 [gr-qc].

[152] B. J. Owen and B. S. Sathyaprakash, "Matched filtering of gravitational waves from inspiraling compact binaries: Computational cost and template placement," *Phys. Rev.*, vol. D60, p. 022 002, 1999. arXiv: gr-qc/9808076 [gr-qc].

[153] J. Veitch *et al.*, "Parameter estimation for compact binaries with ground-based gravitational-wave observations using the LALInference software library," *Phys. Rev.*, vol. D91, no. 4, p. 042 003, 2015. arXiv: 1409.7215 [gr-qc].

[154] G. Ashton *et al.*, "BILBY: A user-friendly Bayesian inference library for gravitational-wave astronomy," *Astrophys. J. Suppl.*, vol. 241, no. 2, p. 27, 2019. arXiv: 1811.02042 [astro-ph.IM].

[155] J. Lange, R. O'Shaughnessy, and M. Rizzo, "Rapid and accurate parameter inference for coalescing, precessing compact binaries," May 2018. arXiv: 1805.10457 [gr-qc].

[156] K. Wette, "SWIGLAL: Python and Octave interfaces to the LALSuite gravitational-wave data analysis libraries," *SoftwareX*, vol. 12, p. 100 634, 2020. arXiv: 2012.09552 [astro-ph.IM].

[157] T. B. Littenberg and N. J. Cornish, "Bayesian inference for spectral estimation of gravitational wave detector noise," *Phys. Rev. D*, vol. 91, no. 8, p. 084 034, 2015. arXiv: 1410.3852 [gr-qc].

[158] M. Millhouse, N. J. Cornish, and T. Littenberg, "Bayesian reconstruction of gravitational wave bursts using chirplets," *Phys. Rev.*, vol. D97, no. 10, p. 104 057, 2018. arXiv: 1804.03239 [gr-qc].

[159] K. Chatziioannou, M. Isi, C.-J. Haster, and T. B. Littenberg, "Morphology-independent test of the mixed polarization content of transient gravitational wave signals," *Phys. Rev. D*, vol. 104, no. 4, p. 044 005, 2021. arXiv: 2105.01521 [gr-qc].

[160] K. Chatziioannou, C.-J. Haster, T. B. Littenberg, W. M. Farr, S. Ghonge, M. Millhouse, J. A. Clark, and N. Cornish, "Noise spectral estimation methods and their impact on gravitational wave measurement of compact binary mergers," *Phys. Rev.*, vol. D100, no. 10, p. 104 004, 2019. arXiv: 1907.06540 [gr-qc].

[161] P. J. Green, "Reversible jump markov chain monte carlo computation and bayesian model determination," *Biometrika*, vol. 82, no. 4, pp. 711–732, 1995.

[162] R. P. Woodard, "Avoiding dark energy with 1/r modifications of gravity," *Lect. Notes Phys.*, vol. 720, pp. 403–433, 2007. arXiv: astro-ph/0601672 [astro-ph].

[163] A. De Felice and S. Tsujikawa, "f(R) theories," *Living Rev. Rel.*, vol. 13, p. 3, 2010. arXiv: 1002.4928 [gr-qc].

[164] P. Kanti, "Black holes in theories with large extra dimensions: A Review," *Int. J. Mod. Phys.*, vol. A19, pp. 4899–4951, 2004. arXiv: hep-ph/0402168 [hep-ph].

[165] L. S. Collaboration and V. Collaboration, "BayesWave Glitch Subtraction," LIGO, Tech. Rep. DCC-T1700406, Nov. 2019.

[166] M. Hannam, P. Schmidt, A. Bohe, L. Haegel, S. Husa, F. Ohme, G. Pratten, and M. Purrer, "Simple Model of Complete Precessing Black-Hole-Binary Gravitational Waveforms," *Phys. Rev. Lett.*, vol. 113, no. 15, p. 151 101, 2014. arXiv: 1308.3271 [gr-qc].

[167] B. P. Abbott *et al.*, "Observation of Gravitational Waves from a Binary Black Hole Merger," *Phys. Rev. Lett.*, vol. 116, no. 6, p. 061 102, 2016. arXiv: 1602.03837 [gr-qc].

[168] V. LIGO Scientific. (2018). "Gwtc-1: Fig. 10."

[169] E. Barausse, A. Buonanno, S. A. Hughes, G. Khanna, S. O'Sullivan, and Y. Pan, "Modeling multipolar gravitational-wave emission from small mass-ratio mergers," *Phys. Rev.*, vol. D85, p. 024 046, 2012. arXiv: 1110.3081 [gr-qc].

[170] A. Taracchini, A. Buonanno, G. Khanna, and S. A. Hughes, "Small mass plunging into a Kerr black hole: Anatomy of the inspiral-merger-ringdown waveforms," *Phys. Rev.*, vol. D90, no. 8, p. 084 025, 2014. arXiv: 1404.1819 [gr-qc].

[171] S. Khan, K. Chatziioannou, M. Hannam, and F. Ohme, "Phenomenological model for the gravitational-wave signal from precessing binary black holes with two-spin effects," *Phys. Rev. D*, vol. 100, no. 2, p. 024 059, 2019. arXiv: 1809.10113 [gr-qc].

[172] S. Khan, F. Ohme, K. Chatziioannou, and M. Hannam, "Including higher order multipoles in gravitational-wave models for precessing binary black holes," *Phys. Rev.*, vol. D101, no. 2, p. 024 056, 2020. arXiv: 1911.06050 [gr-qc].

[173] C. Garcıa-Quirós, M. Colleoni, S. Husa, H. Estellés, G. Pratten, A. Ramos-Buades, M. Mateu-Lucena, and R. Jaume, "Multimode frequency-domain model for the gravitational wave signal from nonprecessing black-hole binaries," *Phys. Rev. D*, vol. 102, no. 6, p. 064 002, 2020. arXiv: 2001.10914 [gr-qc].

[174] G. Pratten *et al.*, "Computationally efficient models for the dominant and subdominant harmonic modes of precessing binary black holes," *Phys. Rev. D*, vol. 103, no. 10, p. 104 056, 2021. arXiv: 2004.06503 [gr-qc].

[175] R. Cotesta, S. Marsat, and M. Pürrer, "Frequency domain reduced order model of aligned-spin effective-one-body waveforms with higher-order modes," *Phys. Rev. D*, vol. 101, no. 12, p. 124 040, 2020. arXiv: 2003.12079 [gr-qc].

[176] S. Ossokine *et al.*, "Multipolar Effective-One-Body Waveforms for Precessing Binary Black Holes: Construction and Validation," *Phys. Rev. D*, vol. 102, no. 4, p. 044 055, 2020. arXiv: 2004.09442 [gr-qc].

[177] V. Varma, S. E. Field, M. A. Scheel, J. Blackman, D. Gerosa, L. C. Stein, L. E. Kidder, and H. P. Pfeiffer, "Surrogate models for precessing binary black hole simulations with unequal masses," *Phys. Rev. Research.*, vol. 1, p. 033 015, 2019. arXiv: 1905.09300 [gr-qc].

[178] V. Varma, S. E. Field, M. A. Scheel, J. Blackman, L. E. Kidder, and H. P. Pfeiffer, "Surrogate model of hybridized numerical relativity binary black hole waveforms," *Phys. Rev. D*, vol. 99, no. 6, p. 064 045, 2019. arXiv: 1812.07865 [gr-qc].

[179] T. A. Apostolatos, "Search templates for gravitational waves from precessing, inspiraling binaries," *Phys. Rev.*, vol. D52, pp. 605–620, 1995.

[180] R. Smith, S. E. Field, K. Blackburn, C.-J. Haster, M. Purrer, V. Raymond, and P. Schmidt, "Fast and accurate inference on gravitational waves from precessing compact binaries," *Phys. Rev.*, vol. D94, no. 4, p. 044 031, 2016. arXiv: 1604.08253 [gr-qc].

[181] B. P. Abbott *et al.*, "Observing gravitational-wave transient GW150914 with minimal assumptions," *Phys. Rev.*, vol. D93, no. 12, p. 122 004, 2016, [Addendum: Phys. Rev.D94,no.6,069903(2016)]. arXiv: 1602.03843 [gr-qc].

[182] M. Vallisneri, J. Kanner, R. Williams, A. Weinstein, and B. Stephens, "The ligo open science center," *Journal of Physics: Conference Series*, vol. 610, p. 012 021, May 2015.

[183] J. B. Kanner, T. B. Littenberg, N. Cornish, M. Millhouse, E. Xhakaj, F. Salemi, M. Drago, G. Vedovato, and S. Klimenko, "Leveraging waveform complexity for confident detection of gravitational waves," *Physical Review D*, vol. 93, no. 2, Jan. 2016.

[184] B. Becsy, P. Raffai, N. J. Cornish, R. Essick, J. Kanner, E. Katsavounidis, T. B. Littenberg, M. Millhouse, and S. Vitale, "Parameter estimation for gravitational-wave bursts with the BayesWave pipeline," *Astrophys. J.*, vol. 839, no. 1, p. 15, 2017. arXiv: 1612.02003 [astro-ph.HE].

[185] F. Mosteller and R. A. Fisher, "Questions and answers," *The American Statistician*, vol. 2, no. 5, pp. 30–31, 1948.

[186] J. Calderon Bustillo, P. Laguna, and D. Shoemaker, "Detectability of gravitational waves from binary black holes: Impact of precession and higher modes," *Phys. Rev.*, vol. D95, no. 10, p. 104 038, 2017. arXiv: 1612.02340 [gr-qc].

[187] K. Jani, J. Healy, J. A. Clark, L. London, P. Laguna, and D. Shoemaker, "Georgia Tech Catalog of Gravitational Waveforms," *Class. Quant. Grav.*, vol. 33, no. 20, p. 204 001, 2016. arXiv: 1605.03204 [gr-qc].

[188] S. Nissanke, D. E. Holz, S. A. Hughes, N. Dalal, and J. L. Sievers, "Exploring short gamma-ray bursts as gravitational-wave standard sirens," *Astrophys. J.*, vol. 725, pp. 496–514, 2010. arXiv: 0904.1017 [astro-ph.CO].

[189] J. Healy, P. Laguna, and D. Shoemaker, "Decoding the final state in binary black hole mergers," *Class. Quant. Grav.*, vol. 31, no. 21, p. 212 001, 2014. arXiv: 1407.5989 [gr-qc].

[190] N. E. Huang, Z. Shen, S. R. Long, M. C. Wu, H. H. Shih, Q. Zheng, N.-C. Yen, C. C. Tung, and H. H. Liu, "The empirical mode decomposition and the hilbert spectrum for nonlinear and non-stationary time series analysis," *Proceedings of the Royal Society of London. Series A: mathematical, physical and engineering sciences*, vol. 454, no. 1971, pp. 903–995, 1998.

[191] B. P. Abbott *et al.*, "Tests of general relativity with GW150914," *Phys. Rev. Lett.*, vol. 116, no. 22, p. 221 101, 2016, [Erratum: Phys. Rev. Lett.121,no.12,129902(2018)]. arXiv: 1602.03841 [gr-qc].

[192] L. S. Collaboration, V. Collaboration, *et al.*, "Tests of general relativity with the binary black hole signals from the ligo-virgo catalog gwtc-1," *arXiv preprint arXiv:1903.04467*, 2019.

[193] B. P. Abbott *et al.*, "Tests of General Relativity with GW170817," *Phys. Rev. Lett.*, vol. 123, no. 1, p. 011 102, 2019. arXiv: 1811.00364 [gr-qc].

[194] T. G. F. Li, W. Del Pozzo, S. Vitale, C. Van Den Broeck, M. Agathos, J. Veitch, K. Grover, T. Sidery, R. Sturani, and A. Vecchio, "Towards a generic test of the strong field dynamics of general relativity using compact binary coalescence," *Phys. Rev. D*, vol. 85, p. 082 003, 2012. arXiv: 1110.0530 [gr-qc].

[195] M. Agathos, W. Del Pozzo, T. G. F. Li, C. Van Den Broeck, J. Veitch, and S. Vitale, "TIGER: A data analysis pipeline for testing the strong-field dynamics of general relativity with gravitational wave signals from coalescing compact binaries," *Phys. Rev. D*, vol. 89, no. 8, p. 082 001, 2014. arXiv: 1311.0420 [gr-qc].

[196] S. Mirshekari, N. Yunes, and C. M. Will, "Constraining Generic Lorentz Violation and the Speed of the Graviton with Gravitational Waves," *Phys. Rev. D*, vol. 85, p. 024 041, 2012. arXiv: 1110.2720 [gr-qc].

[197] B. . P. . Abbott *et al.*, "GW170608: Observation of a 19-solar-mass Binary Black Hole Coalescence," *Astrophys. J. Lett.*, vol. 851, p. L35, 2017. arXiv: 1711.05578 [astro-ph.HE].

[198] ——, "Prospects for Observing and Localizing Gravitational-Wave Transients with Advanced LIGO, Advanced Virgo and KAGRA," *Living Rev. Rel.*, vol. 21, no. 1, p. 3, 2018. arXiv: 1304.0670 [gr-qc].

[199] P. Ajith, M. Hewitson, J. R. Smith, H. Grote, S. Hild, and K. A. Strain, "Physical instrumental vetoes for gravitational-wave burst triggers," *Phys. Rev. D*, vol. 76, p. 042 004, 2007. arXiv: 0705.1111 [gr-qc].

[200] B. P. Abbott, R. Abbott, T. Abbott, F. Acernese, K. Ackley, C. Adams, T. Adams, P. Addesso, R. Adhikari, V. Adya, *et al.*, "Gw170817: Observation of gravita-

tional waves from a binary neutron star inspiral," *Physical Review Letters*, vol. 119, no. 16, p. 161 101, 2017.

[201] B. P. Abbott *et al.*, "GW170817: Observation of Gravitational Waves from a Binary Neutron Star Inspiral," *Phys. Rev. Lett.*, vol. 119, no. 16, p. 161 101, 2017. arXiv: 1710.05832 [gr-qc].

[202] M. Zevin *et al.*, "Gravity Spy: Integrating Advanced LIGO Detector Characterization, Machine Learning, and Citizen Science," *Class. Quant. Grav.*, vol. 34, no. 6, p. 064 003, 2017. arXiv: 1611.04596 [gr-qc].

[203] M. Cabero *et al.*, "Blip glitches in Advanced LIGO data," *Class. Quant. Grav.*, vol. 36, no. 15, p. 15, 2019. arXiv: 1901.05093 [physics.ins-det].

[204] M. Zevi, *Diagnosing the tomte glitch*, https://blog.gravityspy.org/2019/01/23/diagnosing-the-tomte-glitch/, May 2019.

[205] B. P. Abbott *et al.*, "All-Sky Search for Short Gravitational-Wave Bursts in the Second Advanced LIGO and Advanced Virgo Run," *Phys. Rev. D*, vol. 100, no. 2, p. 024 017, 2019. arXiv: 1905.03457 [gr-qc].

[206] R. Abbott *et al.*, "All-sky search for long-duration gravitational-wave bursts in the third Advanced LIGO and Advanced Virgo run," *Phys. Rev. D*, vol. 104, no. 10, p. 102 001, 2021. arXiv: 2107.13796 [gr-qc].

[207] M. H. P. M. van Putten and M. Della Valle, "Observational evidence for Extended Emission to GW170817," *Mon. Not. Roy. Astron. Soc.*, vol. 482, no. 1, pp. L46–L49, 2019. arXiv: 1806.02165 [astro-ph.HE].

[208] B. Margalit and B. D. Metzger, "Constraining the Maximum Mass of Neutron Stars From Multi-Messenger Observations of GW170817," *Astrophys. J.*, vol. 850, no. 2, p. L19, 2017. arXiv: 1710.05938 [astro-ph.HE].

[209] L. Rezzolla, E. R. Most, and L. R. Weih, "Using gravitational-wave observations and quasi-universal relations to constrain the maximum mass of neutron stars," *Astrophys. J.*, vol. 852, no. 2, p. L25, 2018, [Astrophys. J. Lett.852,L25(2018)]. arXiv: 1711.00314 [astro-ph.HE].

[210] M. Hempel and J. Schaffner-Bielich, "Statistical Model for a Complete Supernova Equation of State," *Nucl. Phys.*, vol. A837, pp. 210–254, 2010. arXiv: 0911.4073 [nucl-th].

[211] S. Typel, G. Ropke, T. Klahn, D. Blaschke, and H. H. Wolter, "Composition and thermodynamics of nuclear matter with light clusters," *Phys. Rev.*, vol. C81, p. 015 803, 2010. arXiv: 0908.2344 [nucl-th].

[212] A. Bauswein, H. T. Janka, K. Hebeler, and A. Schwenk, "Equation-of-state dependence of the gravitational-wave signal from the ring-down phase of neutron-star mergers," *Phys. Rev.*, vol. D86, p. 063 001, 2012. arXiv: 1204.1888 [astro-ph.SR].

[213] A. Bauswein and N. Stergioulas, "Unified picture of the post-merger dynamics and gravitational wave emission in neutron star mergers," *Phys. Rev.*, vol. D91, no. 12, p. 124 056, 2015. arXiv: 1502.03176 [astro-ph.SR].

[214] A. Bauswein, N. Stergioulas, and H. .-T. Janka, "Revealing the high-density equation of state through binary neutron star mergers," *Phys. Rev.*, vol. D90, no. 2, p. 023 002, 2014. arXiv: 1403.5301 [astro-ph.SR].

[215] A. Bauswein, N. Stergioulas, and H.-T. Janka, "Exploring properties of high-density matter through remnants of neutron-star mergers," *Eur. Phys. J. A*, vol. 52, no. 3, p. 56, 2016. arXiv: 1508.05493 [astro-ph.HE].

[216] G. A. Lalazissis, J. Konig, and P. Ring, "A New parametrization for the Lagrangian density of relativistic mean field theory," *Phys. Rev.*, vol. C55, pp. 540–543, 1997. arXiv: nucl-th/9607039 [nucl-th].

[217] A. W. Steiner, M. Hempel, and T. Fischer, "Core-collapse supernova equations of state based on neutron star observations," *Astrophys. J.*, vol. 774, p. 17, 2013. arXiv: 1207.2184 [astro-ph.SR].

[218] B. P. Abbott *et al.*, "GW190425: Observation of a Compact Binary Coalescence with Total Mass $\sim 3.4 M_{\odot}$," *Astrophys. J. Lett.*, vol. 892, no. 1, p. L3, 2020. arXiv: 2001.01761 [astro-ph.HE].

[219] D. Radice, S. Bernuzzi, and C. D. Ott, "One-armed spiral instability in neutron star mergers and its detectability in gravitational waves," *Phys. Rev. D*, vol. 94, no. 6, p. 064 011, 2016. arXiv: 1603.05726 [gr-qc].

[220] H. Yang, V. Paschalidis, K. Yagi, L. Lehner, F. Pretorius, and N. Yunes, "Gravitational wave spectroscopy of binary neutron star merger remnants with mode stacking," *Phys. Rev.*, vol. D97, no. 2, p. 024 049, 2018. arXiv: 1707.00207 [gr-qc].

[221] P. Kalmus, K. C. Cannon, S. Marka, and B. J. Owen, "Stacking Gravitational Wave Signals from Soft Gamma Repeater Bursts," *Phys. Rev.*, vol. D80, p. 042 001, 2009. arXiv: 0904.4906 [astro-ph.HE].

[222] F. Robinet, N. Arnaud, N. Leroy, A. Lundgren, D. Macleod, and J. McIver, "Omicron: a tool to characterize transient noise in gravitational-wave detectors," *SoftwareX*, vol. 12, p. 100 620, 2020. arXiv: 2007.11374 [astro-ph.IM].

[223] *International gravitation-wave network (igwn) computing*, https://computing.docs.ligo.org/guide/, Accessed: 2019-01-10.

[224] *Htcondor*, https://research.cs.wisc.edu/htcondor/, Accessed: 2019-01-10.